

POLITECNICO DI TORINO

Collegio di Ingegneria Chimica e dei Materiali

Master of Science Course in Materials Engineering for Industry 4.0

Master of Science Thesis

Application of Hot Isostatic Pressing to Tailor the Microstructure of Additively Manufactured Nickel-Based Superalloy (In939)

Supervisor Candidate

Prof. Bassini Emilio Rufini Martina

INDEX

ABS	STRACT	1
CH	IAPTER 1	2
Stat	te of art	2
1.1	Superalloys	2
1.2	Nickel superalloys	4
	1.2.1 Primary and secondary phases	8
	1.2.3 Precipitated particles: carbides.	13
	1.2.4 Strengthening mechanisms and effect of alloying elements	15
	1.2.5 Inconel 939	18
1.3	Manufacturing processes	20
	1.3.1 Cast and Wrought processes	20
	1.3.2 Additive manufacturing	22
	1.3.2.1 LPBF (Laser Powder Bed Fusion)	24
1.4	Heat treatments in Ni-based superalloys	27
	1.4.1 Typical heat treatments	27
	1.4.2 Hot isostatic Pressing (HIP)	29
1.5	Incipient melting	30
СН	IAPTER 2	33
Mai	terials and methods	33
2.1	Description of IN939 analyzed	34
2.2	Metallographic preparation of sample	34
2.3	Specimens Analysis	36
	2.3.1 Optical Microscope	36
	2.3.2 Scanning Electron Microscopy (SEM)	37
	2.3.3 Field-Emission Scanning Electron Microscopy (FESEM)	38
	2.3.4 Electron Backscatter Diffraction (EBSD) Analysis	38
2.4	Grain size assesment	39
2.5	Porosity analysis	40
26	Differential scanning calorimetry (DSC)	40

2.7 Air-furnac	e Heat Treatment	41								
2.8 HIP (Hot)	sostatic pressing)	42								
2.9 Nano inde	2.9 Nano indentation test									
2.10 Minitab so	oftware	43								
CHAPTER 3		45								
Results		45								
3.1. Characteri	zation of IN939 as built sample	46								
3.2 Character	ization of air furnace heat treated IN939 samples	50								
3.2.1	Characterization of standard solution heat treated IN939 samples	51								
3.2.2	Characterization of non-standard heat-treated specimens	54								
3.3 Characteri	zation of hipped IN939 samples	79								
3.3.1	Sample 1: 1260 °C – 125 MPa – 240 min	81								
3.3.2	Sample 2: 1280 °C – 125 MPa – 240 min	85								
3.3.3	Sample 3: 1300 °C – 125 MPa – 240 min	87								
CHAPTER 4		91								
Discussion of r	esults	91								
CHAPTER 5		103								
Conclusion		103								
ACKNOWLED	GEMENTS	105								
BIBLIOGRAP	HY	106								

ABSTRACT

The object of this study is the characterization of a nickel superalloy, Inconel 939, processed by Laser Powder Bed Fusion (LPFB), an Additive Manufacturing (AM) technique. This kind of metallic material finds its application in crucial fields such as the aerospace sector and energy production, particularly in the production of turbine blades. Here the specific properties required for the service, such as mechanical stability at high temperatures, meet those of nickel superalloys. Whitin this group of materials, IN939 has excellent mechanical characteristics and resistance to corrosion and oxidation at high temperatures. However, Ni superalloys exhibit high melting temperature, low castability and forgeability. These conditions make additive manufacturing one of the most attractive choices for the production of these alloys. Indeed, AM allows to build components with a layer-by-layer process, using a 3D model. This allows for components with a more complex geometry and also to a completely different defectiveness compared to those shown by traditional methods. The critical aspect is that with this technology the final microstructure is composed of extremely fine grains, condition that is excellent for fatigue resistance but results in an issue for creep resistance. This is where the thesis focuses. The main scope is to assess the impact on the microstructure of non-standard heat treatments and HIP treatment above the solidus temperature of IN939. Following an initial solution heat treatment conducted at 1160°C for a duration of four hours, microstructural analysis confirmed the successful dissolution of secondary carbides into the γ (gamma) matrix. Notably, this treatment did not induce recrystallization, thereby preserving the existing grain structure. Subsequent investigative heat treatments, performed at elevated temperatures, revealed that exceeding a specific thermal threshold leads to the onset of incipient melting. This phenomenon is characterized by the localized formation of a liquid phase at grain boundaries and other regions with a depressed solidus temperature, often due to solute segregation or the presence of low-melting-point eutectic phases. This melting event is highly detrimental, resulting in the formation of micro-porosity and irreversible damage to the material's integrity. The primary objective of this study is maximizing the grain size to enhance the high-temperature performance, specifically the creep resistance, of the superalloy through microstructural control. While the high-temperature heat treatments can promote grain growth, their practical application is fundamentally limited by the incipient melting temperature, which constrains the maximum usable processing temperature. The observation of liquid phase formation, however, suggests an alternative processing route. This study proposes investigating the potential of Hot Isostatic Pressing (HIP) as a means to circumvent this limitation. The central hypothesis is that the application of high isostatic pressure during HIP may suppress the thermodynamic driving force for melting, inducing a shift in the phase equilibrium and allowing the material to be processed within or near the conventional incipient melting region without the catastrophic formation of liquid phase. Alternatively, the pressure may significantly delay its formation, permitting access to higher temperatures than are achievable at atmospheric pressure. Consequently, this research aims to systematically explore this hypothesis. The goal is to determine whether the synergistic combination of high temperature and high isostatic pressure can facilitate extreme grain coarsening without causing microstructural damage.

CHAPTER 1

State of art

1.1 Superalloys

Superalloys are a particular group of alloys based on nickel, cobalt or iron-nickel discovered during the 20th century due to the need for stronger, more corrosion-resistant materials for high-temperature applications. Nowadays, indeed they are used particularly in fields such as aeronautics, automotive and power generation where high performances are required. These materials in fact exhibit high mechanical properties, e.g. high yield strength, fatigue resistance, high corrosion and thermal oxidation resistance. They are generally used at temperatures above about 540 °C. Cobalt-base and nickel-base superalloys may be wrought and cast, depending on the application/composition involved while iron-nickel-base superalloys are generally wrought (where wrought includes powder metallurgy processing) [1]. Superalloys are known to have complex chemical composition, so they are classified according to their base element and strengthening mechanisms, showing different crystal lattice structures. Fe-Ni- base superalloys are typically strengthened by intermetallic compound precipitation in a faced-centered cubic (FCC) matrix, called gamma (y) phase. The most common precipitate is γ , a secondary phase with FCC structure. At the current time iron-nickel-base superalloys invariably are used in wrought conditions. Another group is Nickel-base superalloy. Intermetallic compound precipitation and/or carbides strengthen the material in an austenitic FCC matrix. The third class is cobalt-base superalloys. They are invariably strengthened by a combination of carbides and solid-solution hardeners. No intermetallic compound possessing the same degree of utility as the γ ' precipitates in nickel-or iron-nickel base superalloys has been found to be operative over a wide range in cobalt-base systems [1]. All the classes described above are represented in the figure below.

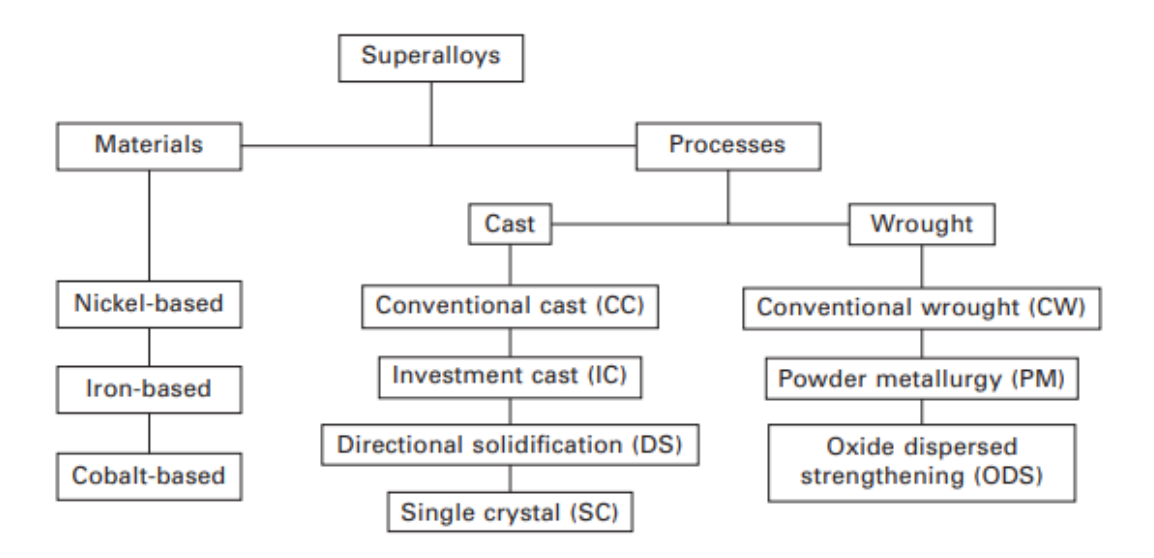


Figure 1.1. Classification of superalloys [5].

Superalloys exhibit high fatigue strength, good toughness, good corrosion resistance, both at low and high temperatures. *Figure 1.2* shows the trend of stress-rupture strengths as a function of the temperature. Superalloys owe their strength from solid solution hardeners, that is substituted atoms interfere with deformation, and precipitated phases, that are gamma prime (γ ') and gamma double prime (γ '') present in Fe-Ni- and Ni- based superalloys. These two phases can significantly strengthen these classes of superalloys. Ather type of strengthening are shown in the figure, i.e. for carbides, which reinforces directly, related to dispersion, or indirectly, in relation of stabilizing grain boundaries against excessive shear, however, a reinforcement limited to superalloys. In addition to elements that promote the formation of carbides and gamma prime phase or produce hardening by solid solution, superalloys, based on nickel and nickel-iron, other elements such as Boron, Zirconium, Hafnium, improve their mechanical and chemical properties.

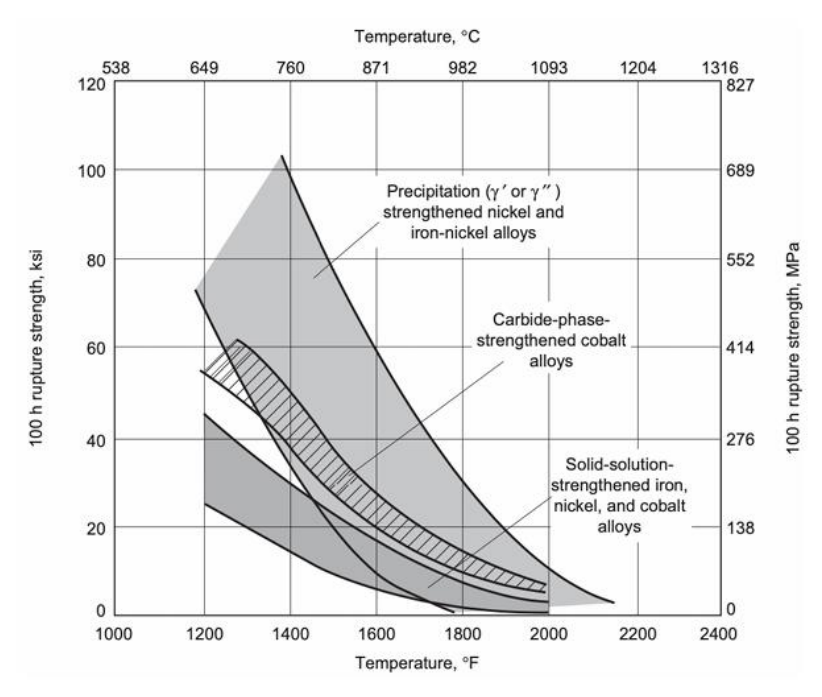


Figure 1.2. Stress-rupture strengths of alloys [1].

Figure 1.3 charts the specific strength (strength-to-density ratio, measured in MPa/(Mg/m³)) against temperature (K) for various advanced materials. The data illustrates that superalloys occupy a critical performance niche in the temperature range between approximately 800 K and 1200 K. Their specific strength is superior to that of titanium and aluminum alloys at elevated temperatures and remains robust within this operational window. The graph signifies a major compromise in the balance of key material properties, creep strength, oxidation resistance, and damage tolerance, that emerges around the 1200 K threshold. This represents a fundamental performance ceiling for conventional polycrystalline superalloys. The figure further differentiates a subclass within this family: single crystal superalloys. By eliminating grain boundaries, which are primary pathways for creep deformation and failure, this advanced variant extends the superalloy performance envelope, offering enhanced specific strength and pushing the operational temperature limit further before the property compromises become critically limiting. This allows them to bridge the gap towards the even higher-temperature capabilities of refractory metals and intermetallics.

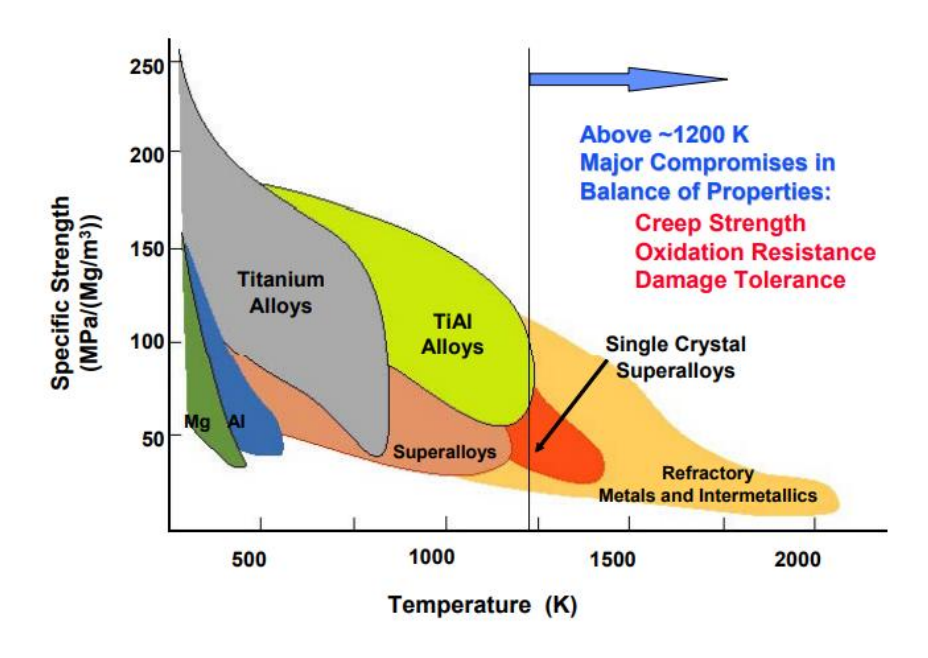


Figure 1.3. Strengths of advanced metallic materials. SOURCE: Hardwick (2005).

1.2 Nickel superalloys

Nickel-base superalloys are among the most high-performing and complex materials in existence, making them the subject of extensive study. They can achieve the highest temperature/strength combination of all cast and wrought superalloys, making them ideal for the most demanding applications, such as turbine blades. Wrought nickel-base superalloys are often used where high toughness is required, such as turbine discs and forged blades. Examples of the wrought alloys include Udimet 700, Rene 41, Waspaloy, N-901, and Udimet 630. Castings are favored for high strength and creep resistance in high-temperature applications, such as investment-cast turbine blades and wheels, and are represented by alloys such as Inconel alloys 100, 713, 738, and 792, single-crystal cast alloys PWA1483, PWA1484, CMSX-4, and Rene N6. The superior hightemperature capability of nickel-base superalloys is due to the precipitation of high-volume fractions of the γ' , Ni₃(Al, Ti) phase, which requires combined aluminum and titanium contents of at least four to six weight percent. This precipitate is the main strengthening phase in such wrought alloys as Waspaloy, Astroloy, Udimet alloys 700 and 720 and in such cast alloys as Rene 80, MAR-M 247, and Inconel 713 and in all of the directionally solidified and single-crystal superalloys. Some nickel-base alloys do not rely on precipitates for strengthening but rather depend mainly on solid-solution hardening (SSH). Two notable alloys strengthened by SSH are Hastelloy X and alloy 625, but they also derive some hardening through carbide and/or intermetallic compound precipitation. Within the wrought alloys, there is another group of superalloys that is produced by pounding in a dry milling process. They are known as mechanically alloyed (MA) materials. The MA process involves a metallic and/or nonmetallic powder charge being worked by a highly energetic ball to produce a composite metal powder. As a result of the repeated welding-fracturing process, the MA powder has a fine lamellar structure (spacing under 0.7 µm) and is chemically homogeneous [3]. Nickel-based alloys consist of up to 40% of the weight of nickel and combinations of other five or ten elements. Figure 1.4 illustrates the major alloying elements that may be present in nickel-base superalloys. The amount of each element is represented by the height of its corresponding block.

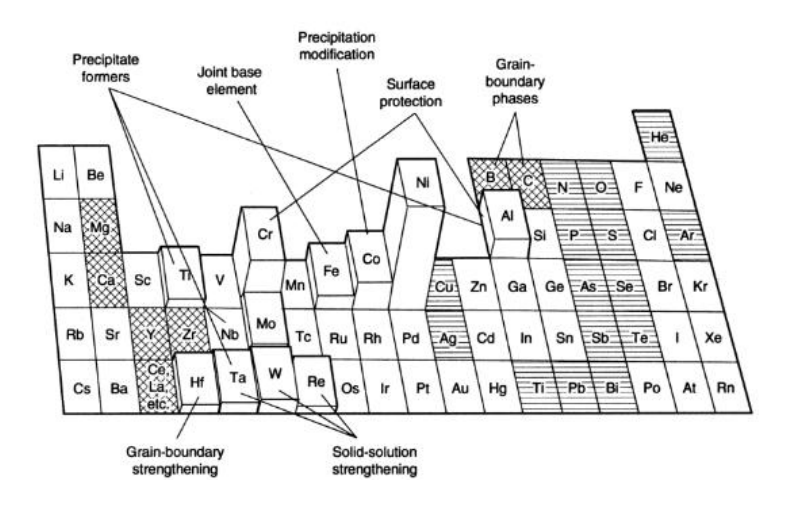


Figure 1.4. Principal alloying elements of nickel superalloys [1].

The chemical composition determines different nickel superalloys. The principal ones are reported in *Table 1.1*.

Alloy	Cr	Co	Mo	W	Ta	Re	Nb	Al	Ti	Hf	C	В	Y	Zs	Other
S 50.00	-0.11		7.52.50		200-0	Conven	tionally	Cast All	ovs	0.000				50000	
Mar-M246	8.3	10.0	0.7	10.0	3.0	-	_	5.5	1.0	1.50	0.14	0.02	-	0.05	-
Rene' 80	14.0	9.5	4.0	4.0	-	-	_	3.0	5.0	-	0.17	0.02	_	0.03	-
IN-713LC	12.0	-	4.5	_	-	-	2.0	5.9	0.6	_	0.05	0.01	_	0.10	_
C1023	15.5	10.0	8.5	_	-	-	_	4.2	3.6	-	0.16	0.01	-	-	-
						Direction	nally Sol	idified A	llovs						
IN792	12.6	9.0	1.9	4.3	4.3	-	_	3.4	4.0	1.00	0.09	0.02	-	0.06	-
GTD111	14.0	9.5	1.5	3.8	2.8		_	3.0	4.9	-	0.10	0.01	-	-	-
					Firs	-Genera	tion Sing	le-Cryst	al Alloy:	8					
PWA 1480	10.0	5.0		4.0	12.0	-	-	5.0	1.5	D. Seeding		0.000			
Rene' N4	9.8	7.5	1.5	6.0	4.8	-	0.5	4.2	3.5	0.15	0.05	0.00	_	-	-
CMSX-3	8.0	5.0	0.6	8.0	6.0	-	-	5.6	1.0	0.10	-	-	_	-	-
					Secon	d-Gener	ation Sin	gle-Cry	stal Allo	VX.					
PWA 1484	5.0	10.0	2.0	6.0	9.0	3.0	-	5.6	-	0.10	-	-	-	2000	-
Rene' N5	7.0	7.5	1.5	5.0	6.5	3.0	_	6.2	-	0.15	0.05	0.00	0.01	-	-
CMSX-4	6.5	9.0	0.6	6.0	6.5	3.0	_	5.6	1.0	0.10	_	_	-	-	-
					Thin	d-Genera	tion Sing	ele-Crys	tal Alloy	8					
Rene' N6	4.2	12.5	1.4	6.0	7.2	5.4	-	5.8	-	0.15	0.05	0.00	0.01	-	-
CMSX-10	2.0	3.0	0.4	5.0	8.0	6.0	0.1	5.7	0.2	0.03	-	-	-	-	-
						Wro	ught Sup	eralloys							
IN 718	19.0	-	3.0	_	-	-	5.1	0.5	0.9	-	100	0.02	-	-	18.5Fe
Rene' 41	19.0	11.0	10.0	-	-	-	-	1.5	3.1	-	0.09	0.005	-		-
Nimonic 80A	19.5	-	-	_	-	-	-	1.4	2.4	-	0.06	0.003	_	0.06	-
Waspaloy	19.5	13.5	4.3	_	-	-	-	1.3	3.0	-	0.08	0.006	-	-	-
Udimet 720	17.9	14.7	3.0	1.3	-	-	-	2.5	5.0	-	0.03	0.03	-	0.03	-
					3	Powder-H		d Supera	dloys						
Rene' 95	13.0	8.0	3.5	3.5	-	-	3.5	3.5	2.5	-	0.065	0.013	_	0.05	-
Rene' 88 DT	16.0	13.0	4.0	4.0	-	-	0.7	2.1	3.7	-	0.03	0.015	-	-	-
N18	11.2	15.6	6.5	_	-	-	-	4.4	4.4	0.5	0.02	0.015	_	0.03	_
IN100	12.4	18.4	3.2	-	-	-	_	4.9	4.3	-	0.07	0.02		0.07	

Table 1.1. Chemical composition of principal nickel superalloys [1].

These materials are employed in many applications where high performances at high temperatures are required. They are primarily manufactured as critical components for areo-engine turbines, yet their application extends to aerospace propulsion systems, heat exchangers, and the chemical and petrochemical industries, as well as to power-generation turbines. A typical application of nickel superalloys is reported in *Figure 1.5* that shows the materials employed for the different components of a gas turbine. It is possible to notice that nickel superalloys are spready involved.

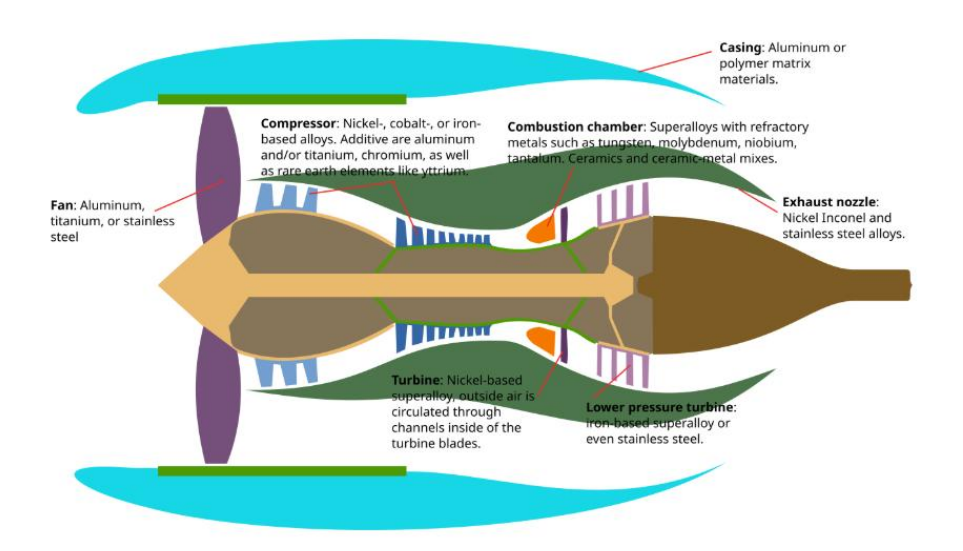


Figure 1.5. Different materials used for design of a gas turbine [21].

Over the years, numerous generations of nickel-based superalloys have been developed with the objective of operating under increasingly elevated temperature conditions. This developmental trend is directly correlated with the pursuit of enhanced thermodynamic efficiency. Specifically, for both power-generation and aero-engine turbines, efficiency demonstrates a linear relationship with the turbine entry temperature (TET). Consequently, the drive for greater efficiency provides a continuous impetus for the advancement of materials capable of withstanding more extreme thermal environments. This development is shown in *Figure 1.6*. This graph illustrates the historical progression of turbine entry temperature (TET) in aeroengines, demonstrating how the introduction of new material classes and cooling technologies has enabled a consistent increase in operational temperatures, thereby enhancing engine performance and efficiency [6].

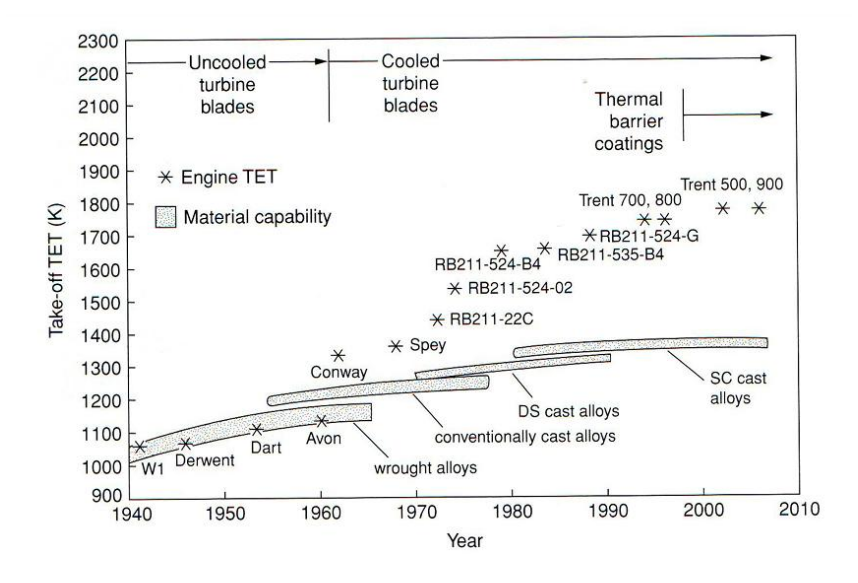


Figure 1.6. Evolution of the turbine entry temperature (TET) capability of Rolls-Royce's civil aeroengines, from 1940 to the present day [6].

Figure 1.7 demonstrates the superior performance of nickel-base superalloys, which retain their specific strength (a key property measuring strength-to-weight ratio) with minimal degradation at temperatures nearing their melting point, a characteristic in which they significantly outperform other

metallic materials. While aluminum and titanium alloys exhibit excellent specific strength at lower temperatures, their mechanical properties degrade rapidly as temperature increases. Nickel-based superalloys, however, demonstrate exceptional retention of specific strength at elevated temperatures. This property is paramount for components such as high-pressure turbine blades and vanes, which must withstand immense centrifugal stresses and aggressive thermal cycling at temperatures often exceeding 80% of their melting point. Consequently, the operational window of modern gas turbines is intrinsically linked to the high-temperature specific strength capability of these advanced superalloys, enabling higher turbine entry temperatures and, thus, greater thermodynamic efficiency.

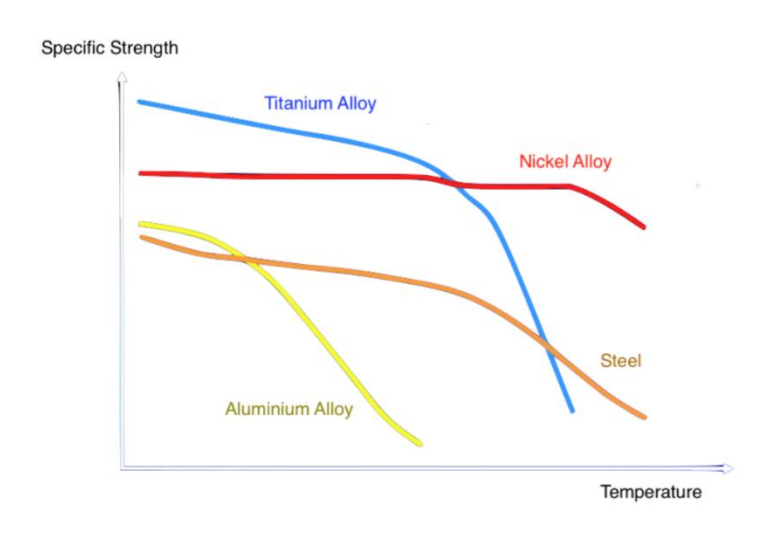


Figure 1.7. Specific strength as a function of temperature of different materials [21].

Concerning high-temperature capabilities, *Figure 1.8* shows the response of various engineering alloys materials by plotting their creep against their oxidation resistance. It is possible to notice that nickel superalloy is the best in performance at high temperatures for both the properties. This comparison clearly positions nickel-based superalloys as the premier material class, significantly outperforming all others like cobalt superalloys, stainless steels, and iron-based alloys by occupying the top-right quadrant of the chart. Their exceptional performance, which begins to surpass other materials at temperatures above approximately 1100°C, is due to a unique microstructure that provides unparalleled resistance to deformation and environmental degradation under extreme thermal and mechanical stress. This combination of superior creep strength and oxidation resistance makes them the indispensable material for the most critical components in aerospace and power generation turbines, such as high-pressure turbine blades and vanes. Nickel-based superalloys can be used to a higher fraction of melting temperature and are therefore more favorable than cobalt-based and iron-nickel-based superalloys at service temperatures close to the melting temperature of the materials [9].

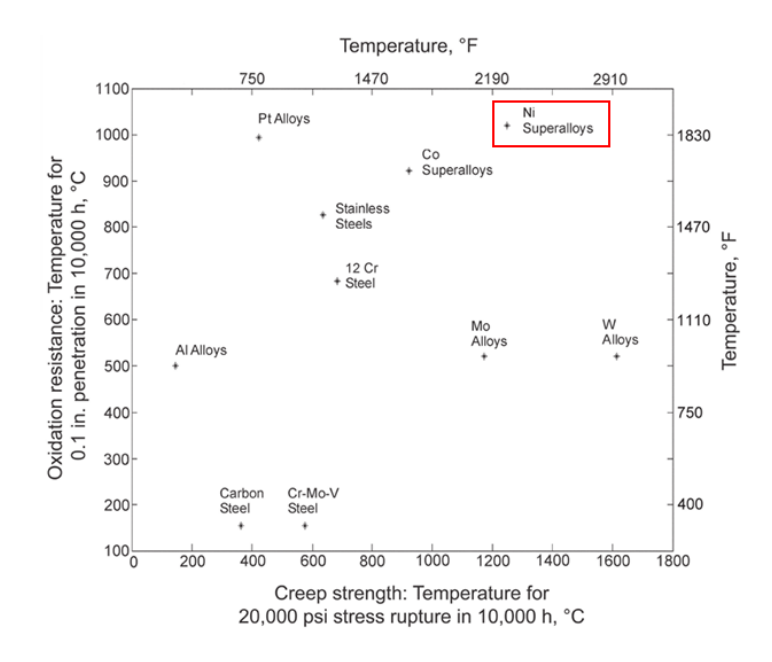


Figure 1.8. Graph shows different materials position based on their creep strength and oxidation resistance [8].

1.2.1 Primary and secondary phases

Nickel-based superalloys possess a face-centered cubic (FCC) crystal structure, which confers high toughness and ductility. They do not undergo allotropic transformations: the FCC structure is retained even at elevated temperatures. Different phases are formed during the fabrication of nickel-based superalloys. The dominating phases are the gamma matrix and the gamma prime. The austenitic (γ) matrix has an FCC structure and within this matrix, a high number of alloying elements are dissolved, each serving a specific function in enhancing mechanical properties and environmental resistance [9]. The amount of γ ' depends on the chemical composition and temperature, as illustrated in the ternary phase diagrams in *Figure 1.9*. The Ni-Al-Ti ternary phase diagrams show the γ and γ ' phase field. For a given chemical composition, the fraction of γ ' decreases as the temperature is increased. This phenomenon is used to dissolve the γ ' at a sufficiently high temperature (a solution treatment) followed by ageing at a lower temperature in order to generate a uniform and fine dispersion of strengthening precipitates [10].

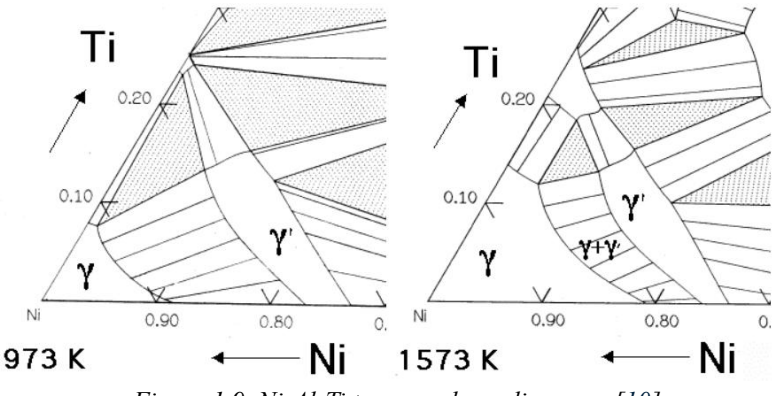


Figure 1.9. Ni-Al-Ti ternary phase diagrams [10].

This section provides a systematic overview of the major phases that constitute the microstructure of nickel-base superalloys, detailing their composition, morphology, and influence on material properties.

The matrix is gamma (γ) phase.

It is an FCC nickel-base nonmagnetic phase that usually contains a high percentage of solid-solution elements such as cobalt, iron, chromium, molybdenum, and tungsten. All nickel-base alloys contain this phase as the matrix [1]. The structure of γ phase is illustrated in *Figure 1.10*.

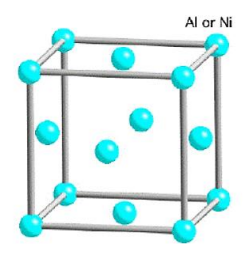


Figure 1.10. Crystal structure of gamma (γ) [9].

Nickel by itself has neither exceptional high elastic modulus nor low diffusivity. On the other hand nickel, has a nearly filled third electronic shell which allows alloying with solid solution strengthening elements without losses in phase stability. The alloy elements composing the gamma matrix mainly belong to Group V, VI and VII and are cobalt, iron, chromium, molybdenum and tungsten. [11].

Gamma prime (γ') phase.

It was not identified until the 1940's. It is formed from elements from Group III, IV and V. The addition of, for example aluminium and titanium, which are the essential solutes, results in a reaction with nickel, precipitating the γ' phase of the form Ni3X, where X is an alloy element. Other elements included in the γ' phase can be chromium, hafnium, niobium and tantalum [11,12]. Gamma prime phase is the principal high-temperature strengthening phase. It appears as spheres or cuboids when properly formed. γ' films along grain boundaries in some wrought and cast alloys; produced by heat treatments and service exposure. These films may be beneficial for creep-rupture properties. γ' in rafts (elongated γ' in the grain) may be produced by initial heat treatment or by extended service operation. These rafts may be useful for increasing creep-rupture properties [1]. The structure of the gamma prime is FCC and the atom ordering is illustrated in *Figure 1.11*.

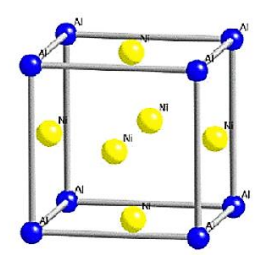


Figure 1.11. Crystal structure of gamma prime (γ') [9].

There are several benefits of the presence of γ' in the matrix. The coherence between γ' and γ results in a low surface energy and in an exceptional long-time stability. This phase is also the reason for the

high temperature strength and creep resistance in most superalloys [13]. The strength of the alloy is strongly dependent on the volume fraction of γ' . Wrought alloys contain 20-45 % of γ' . Higher fractions will make the deformation too difficult. Cast superalloys can have a volume fraction of up to 60%, which will increase the alloy strength compared with the wrought alloys [11,13].

Gamma double prime(γ ") phase.

Nickel and niobium combine in the presence of iron to form bct Ni₃Nb, which is coherent with the gamma matrix, while inducing large mismatch strains (of the order of 2.9%). This phase provides very high strength at low-to-intermediate temperatures, but it is unstable at temperatures above about 1200 °F (649 °C). This precipitate is found in only a few nickel-(nickel-iron-) base alloys [1]. The gamma double prime precipitate is a useful strengthening phase, mainly in such nickel-iron-base superalloys as 718 and 706 alloys. When greater strength is required at lower temperatures (e.g. turbine discs), alloys can be strengthened using this phase known as γ ". It occurs in nickel superalloys with significant additions of niobium (Inconel 718) or vanadium; the composition of the γ " is then Ni₃Nb or Ni₃V. The crystal structure of γ " is based on a body-centered tetragonal lattice with an ordered arrangement of nickel and niobium atoms as shown in *Figure 1.12*. Strengthening occurs therefore by both a coherency hardening and order hardening mechanism. The lattice parameters of γ " are approximately a=0.362 nm and c=0.741 nm [10].

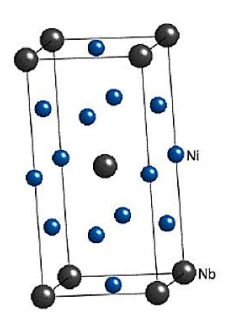


Figure 1.12. Crystal structure of gamma double prime (γ'') [10].

TCP phases.

They usually are platelike or needlelike phases such as σ and Laves that may form for some compositions and under certain conditions. These phases can cause lowered rupture strength and ductility. The likelihood of their presence increases as the solute segregation of the ingot increases [1].

Another phase is eta phase (η) .

This phase is generally regarded as a detrimental phase, exerting negative effect on tensile and creeprupture properties. This phase has a hexagonal close-packed (HCP) structure as shown in *Figure 1.13*. Eta phase has been reported to have different chemistry in different superalloys. Generally, Waspaloy is susceptible to precipitate η -Ni3Ti phase at intermediate or high temperature during long-term exposure, especially under external stress. This is mainly due to the relatively higher Ti/Al ratio composition in Waspaloy, as it is widely established that high Ti content or Ti/Al ratio would promote the formation of this phase. Pickering et al. reported that Nb atoms replaced certain Al sites, leaving Ti and Al to occupy randomly the other sites. However, in another superalloy, it was Ta along with Nb that occupied η phase crystal structure [14].

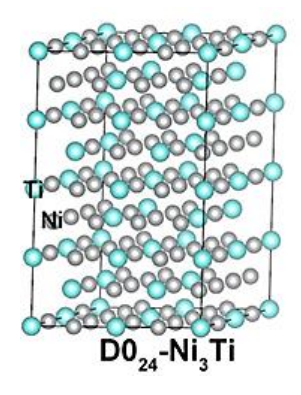


Figure 1.13. Crystal structure of η phase [15].

According to whether the grain boundary directly evolves in reaction, the precipitation of η phase is divided into two mechanisms. In the first, the phase nucleates at the grain boundary defects or carbides, subsequently grows toward the grain interior through the lattice diffusion by which Ni and Ti solutes transport to the incoherent precipitate/matrix interface, η / γ interface, and eventually develops a Widmanstatten morphology. The second mechanism provides η phase that nucleates at the grain boundary on one grain side, extends to the adjacent grain by the discontinuous precipitation reaction, and eventually exhibits a unique isolated cellular morphology [15]. η phase normally exhibits a needle-like, thin-plate-like or sheet-like morphology as shown in *Figure 1.14*.

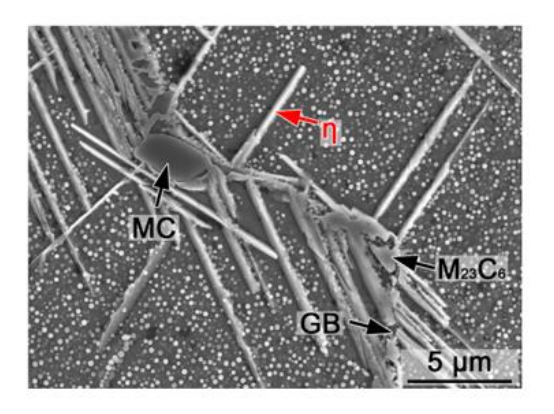


Figure 1.14. n phase [15].

Figure 1.15 shows the DTA thermograph obtained on cooling and heating for alloy IN939. A particular focus of this analysis is on the thermal event represented by Peak 3 (Figure 1.15. (a)): a slight inflection was observed around 1482 K. This value corresponds to the final precipitation event which was found to be precipitation of eutectic η -phase. The amount encountered was small and probably the sensibility of equipment used was not enough to obtain a clear peak. For heating part (b) Peak1 at 1508K is likely the beginning of the melting of the matrix and thus the solidus temperature. Platelet η -phase is found appearing in as-cast pieces after standard heat treatment (4h/1433 K, homogenization) and an incipient melting of the alloy corresponding at a temperature of 1483 K [20].

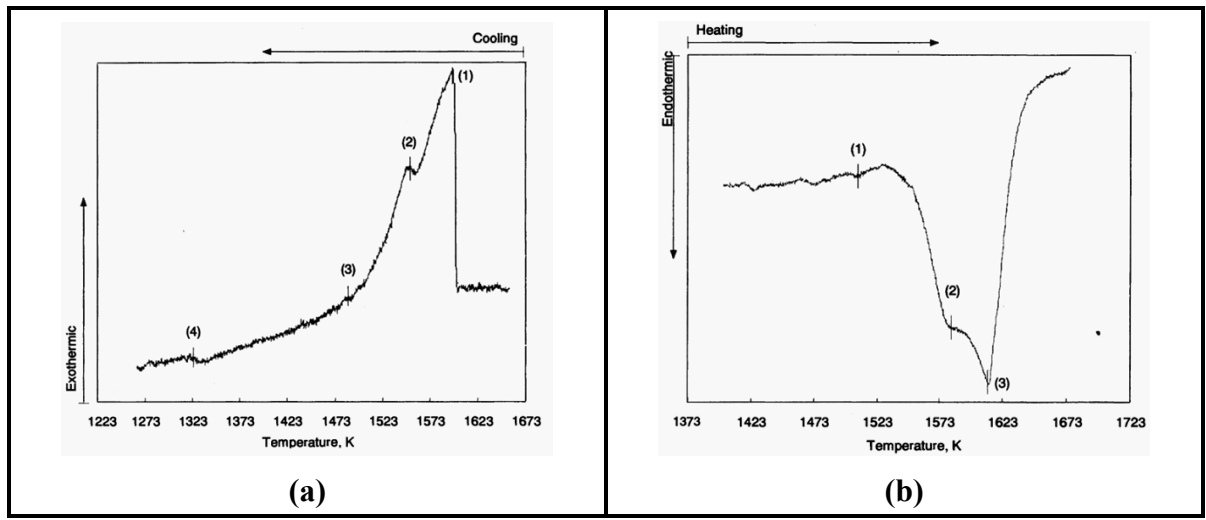


Figure 1.15. DTA thermograph on (a) cooling and (b) heating of IN939 [19].

The precipitation of the platelet phase (η) occurred at the very last stage of the solidification process. The composition of the phase is shown in *Figure 1.16*. Considering the nominal formula A₃B of the η -phase (Ni₃Ti), elements such as Ni, Co, and Cr represent the A component, and Ti, Ta, Nb, and Al the B component. It was important to note that this phase generally was associated with voids and cracks, while the matrix was not. This is an indication that this particle is very brittle, since even standard metallographic preparation was enough to cause such cracks [19].

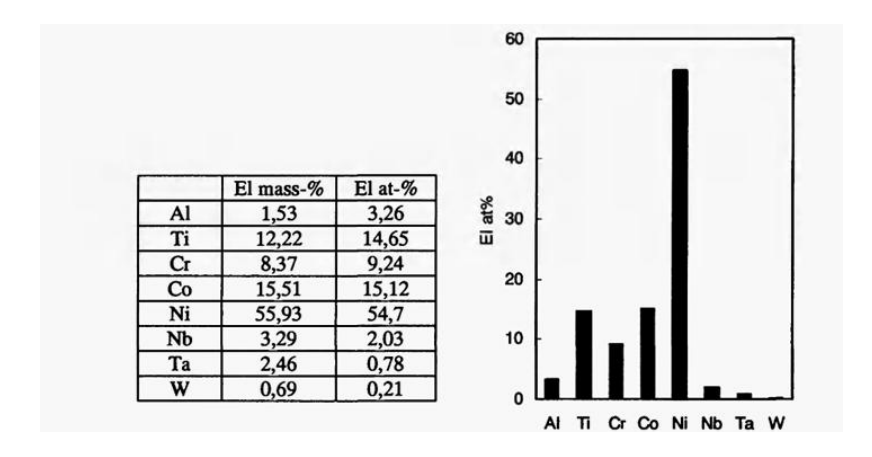


Figure 1.16. Chemical composition by EDS of the platelet (η)phase in the as-solidified microstructure of IN939[19].

Along with the σ and Laves phases, η phase is an undesirable phase that exerts a detrimental influence on the mechanical characteristics of nickel superalloys.

Another major phase is delta (δ) phase.

This phase has a composition of Ni₃Nb and an orthorhombic crystal structure as it is shown in *Figure 1.17*, where Nickel atoms are in red and Niobium atoms in blue. The precipitation of the δ -phase is highly heterogeneous because of the dissimilar structure with respect to the FCC γ -matrix. Delta phase can also form as a transformation product of γ ", which becomes unstable above about 650°C [17]. Although Delta phase precipitates are incoherent and their precipitation is known to reduce the strength of γ " strengthened alloys. It is a stable precipitate that plays a critically dualistic role, being both beneficial and detrimental to mechanical properties depending on its fraction, size, and morphology. Its formation is primarily driven by the niobium content and a specific thermal exposure

range, typically between 700°C and 1000°C. The delta phase serves a vital beneficial role in certain alloy systems, most notably in alloy 718 (Inconel 718). Here, its controlled precipitation is harnessed to pin grain boundaries during thermo-mechanical processing, effectively preventing grain growth and resulting in a fine-grained microstructure that enhances yield strength and improves fatigue life. Furthermore, the formation of δ -phase depletes the matrix of niobium, thereby suppressing the formation of the metastable γ" (Ni₃Nb) phase during aging. This is a crucial mechanism for controlling the final strength and stabilizing the alloy against over-aging during long-term exposure at high temperatures, as the δ -phase is coarser and more stable than γ ". Conversely, the uncontrolled or excessive precipitation of the delta phase is overwhelmingly detrimental. When it forms as coarse plates or needles within the grains or as continuous films along grain boundaries, it acts as a brittle phase that severely compromises mechanical properties. It provides easy paths for crack initiation and propagation, leading to a significant loss in tensile ductility, impact toughness, and stress rupture life. Its presence depletes strengthening elements like Nb from the matrix, reducing the potential for precipitation of the primary strengthening γ' and γ'' phases. Therefore, meticulous control of the heat treatment schedule is essential to optimize the volume fraction and morphology of the δ -phase for the intended service application [6,16].

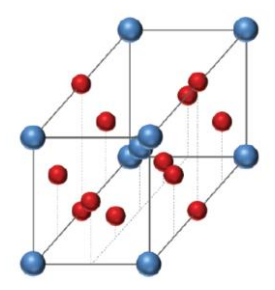


Figure 1.17. Crystal structure of δ phase [17].

Borides.

They have a relatively low density, and these particles may be formed when Boron segregates to grain boundaries. There are several boride phases. Generally, boride phases in minute amounts are favorable for creep-rupture properties [1].

1.2.3 Precipitated particles: carbides.

In nickel superalloys, the addition of carbon, generally in amounts of about 0.02 to 0.2 %, will result in a union with refractory elements such as hafnium, niobium, tantalum and titanium (especially in IN939) leading to the formation of carbides. It is possible to identify primary carbides, MC type, where M represents one of the previously mentioned metals generally Nb and Ti. They are formed during freezing of the alloy due to the wide segregation of these alloying elements in the interdendritic zones [2]. When the material is produced by additive manufacturing technologies, such as LPBF, carbides tend to precipitate in lower amount and dimension due to the rapid cooling. In *Figure 1.14* (a) the exothermic peak 2 during cooling is associated with the precipitation of primary TiC. This reaction occurred within the range 1523-1563 K with a peak at 1553 K [19]. The precipitation

sequence of alloy IN939 starts with a primary precipitation of austenitic γ phase followed by the eutectic reaction (Liquid $\rightarrow \gamma$ + MC) which proceeded until the end of solidification. At high temperatures, simple nitrides or complex carbonitrides are present but also surrounded by MC carbides. They were found in the liquid region or enveloped by the growing γ phase. Later a more active reaction occurred where many carbides with a more 'script-like' morphology were formed. The mechanism of carbide precipitation in alloy IN939 is complex and the final morphology seems to depend on the local solidification conditions [19].

The structure of primary carbides is FCC. During heat treatment carbides tend to decompose into other, secondary, carbide variants, such as $M_{23}C_6$ and M_6C that tend to form at grain boundary [2]. The degeneration of these two carbides is reported in the reactions below:

$$MC+ \gamma \rightarrow M_{23}C_{6+}\gamma'$$
 (1.1)

and

$$MC+ \gamma \rightarrow M_6C + \gamma'$$
 (1.2)

Reaction (1.1) shows that during exposure to high temperatures (typically in the range of 760-980°C or 1400-1800°F), the large, blocky MC carbides are metastable. They react with the surrounding γ matrix. The reaction consumes the MC carbide and elements from the matrix (like Cr) to form a layer or halo of finer, more stable M₂₃C₆ carbides. The formation of γ' is a consequence of this reaction because the decomposition of the MC carbide (e.g., TiC) releases strong γ' -forming elements (like Ti) back into the matrix, allowing additional γ' to precipitate [2]. The most common M element in M₂₃C₆ is chromium but also iron (Fe), tungsten (W) and molybdenum (Mo) can be found in that position. They are the least thermodynamically stable and exhibit a cubic lattice, but they are less tough compared to MC carbides. The M elements generally found in M₆C are molybdenum (Mo) and tungsten (W), but the carbide can contain chromium (Cr), cobalt (Co) and tantalum (Ta) as well. In In939, among the main carbide forming elements, Ti, Nb, and Ta, the former, is the most important one. The proportion of these elements is 4:1:1 [19]. A chemical composition of primary carbide is reported in *Figure 1.18*.

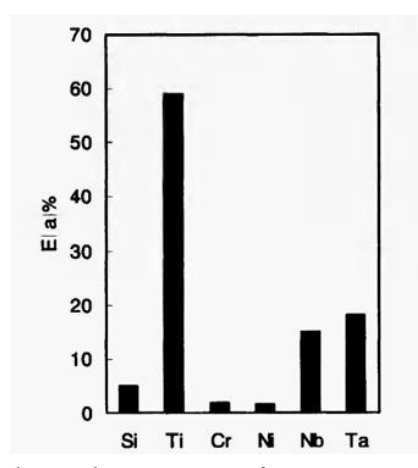


Figure 1.18. EDS chemical composition of a primary carbide of IN939 [19].

The presence of coarse primary carbides of these alloying elements is beneficial for the mechanical properties of the material, as they stabilize grain boundaries and inhibit grain growth following hot mechanical deformation or prolonged thermal exposure. However, excessive precipitation of these carbides is undesirable. They sequester significant quantities of niobium (Nb) and titanium (Ti) from the matrix. These elements are essential for the formation of the strengthening intermetallic γ'' and γ' phases, which are the primary reinforcing precipitates in this superalloy. Furthermore, the volume fraction, morphology, and size of these carbides must be precisely controlled. Coarse or irregularly distributed carbides can act as stress concentration sites, promote grain boundary embrittlement, and serve as initiation points for intergranular corrosion. This corrosive attack is often exacerbated by localized chromium depletion in the matrix regions adjacent to the carbides [18].

A general overview of morphology of the different carbides described above is given in Figure 1.19.

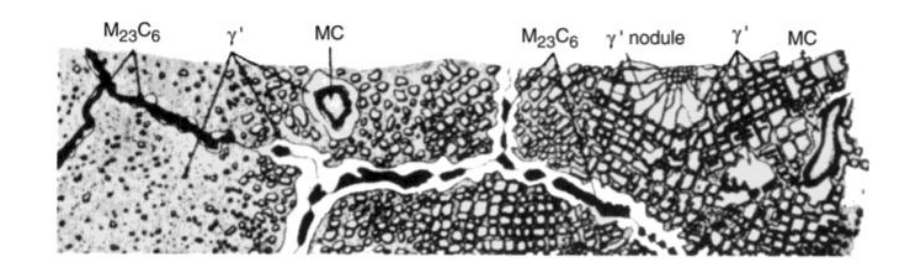


Figure 1.19. Qualitative description of microstructure for nickel-base superalloy [2].

1.2.4 Strengthening mechanisms and effect of alloying elements

Strengthening in superalloys is by solid-solution hardening (substituted atoms interfere with deformation), work hardening (energy is stored by deformation), and precipitation hardening (precipitates interfere with deformation). Carbide production (a favorable distribution of secondary phases interferes with deformation) also produces strength. Nickel-base solid-solution-strengthened alloys are considerably lower than those of the nickel-base precipitation-strengthened [1]. *Figure 1.20* reports all the strength mechanisms related to nickel superalloys.

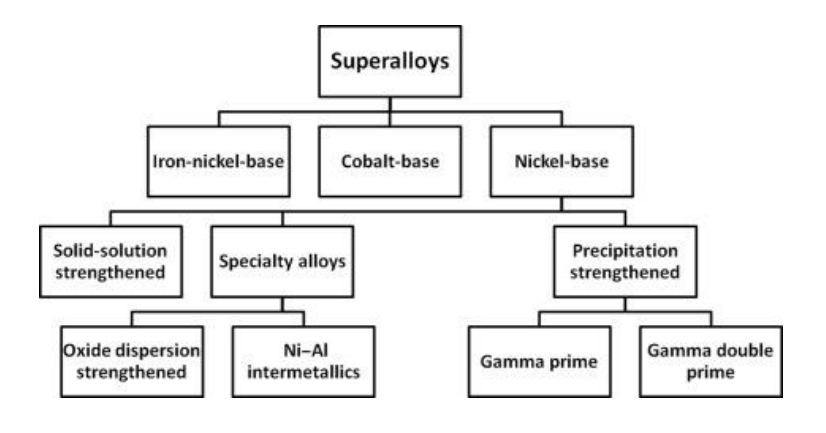


Figure 1.20. Classification of superalloys [4].

For the most demanding applications, for example hot gas path components in land-based and aeronautical gas turbines, nickel-base superalloys are omnipresent as they outperform other superalloys classes. Their high mechanical performance is based on two strengthening mechanisms: solid solution strengthening of the FCC gamma matrix and precipitation hardening by intermetallic γ ' Ni₃(Al, Ti) and/or γ '' Ni₃(Nb) phases. While alloys that are solely solid solution strengthened do not require heat treatment to achieve their optimal strength, precipitation hardening alloys require specific heat treatments to reach their full performance. Additionally, further strengthening can be provided by grain boundary strengthening mechanisms, through the use of Boron, Zirconium, and Carbon. These elements have extremely limited solubility in the γ and γ' phases, and tend to segregate towards grain boundaries, becoming locally enriched in the intergranular areas; borides, carbides, and, to some extent oxides that are formed at the grain boundaries pin the interfaces and prevent grain boundary sliding. This strengthening mechanism is of highest importance when creep resistance and mechanical strength at high temperature are required [4]. In Figure 1.19 also it is shown dispersed oxides strengthening as a mechanism to increase the strength of nickel superalloy. This is a mechanism similar to precipitation hardening, except that the strengthening agent is added to the alloy and not precipitated from the matrix. The production of this family of superalloys is complicated by the fact that the density of ceramics is lower than the metal matrix and tends to float to the surface of the molten metal during casting. The oxides presence in the matrix enhances mechanical resistance and creep properties of the alloy, providing stable properties for long periods of time. Moreover, oxides are found to be beneficial for the oxidation resistance of the alloy, since they act like nucleation agents for protective oxides and make the formed oxide layer smooth [22].

Nickel-based superalloys are composed of various elements; their specific ratios are carefully adjusted to obtain the required properties for a given application. Besides nickel, the alloys contain in general 10-20 % chromium, up to 8% Aluminum together with titanium, and 5-10% Cobalt. Small amounts of Boron, Zirconium and Carbon are included as well. Common additions in some alloys is for example Molybdenum, Tungsten, Niobium, Tantalum and Hafnium. There are also some tramp elements, i.e. elements which unintentionally were included in the alloy, and these elements have to be carefully controlled. Examples of elements belonging to this group are Silicon, Phosphorus, Sulfur, Oxygen and Nitrogen. Chromium and Aluminum are desired since they improve the oxidation resistance of the alloy. A small amount of Yttrium binds the oxide layer to the substrate. Boron and Zirconium are added to the polycrystalline superalloys where they segregate to the grain boundaries. This results in better creep strength and ductility. The carbides tend to precipitate at the grain boundaries and prevent the sliding phenomenon of the boundaries. A few examples of carbide formers are Carbon, Chromium, Molybdenum and Tungsten. Some elements function as solid-solution strengtheners, e.g. Cobalt, Iron, Niobium, Rhenium and Molybdenum. The addition of Titanium will increase the hot corrosion resistance, and the role of nickel is to give phase stability [6].

The effect of individual elements on the material's metallurgy in nickel superalloys is summarized in *Table 1.2* and visualized in *Figure 1.21*.

Table 1.2. Effect of various alloying elements on the metallurgy of y'strengthened nickel superalloys [4].

Effect	Alloying elements				
Solid-solution strengtheners	Co, Cr, Fe, Mo, W, Ta, Re				
Carbide form:					
MC	W, Ta, Ti, Mo, Nb, Hf				
M_7C_3	Cr				
M ₂₃ C ₆	Cr, Mo, W				
M ₆ C	Mo, W, Nb				
Carbonitrides: M(CN)	C, N				
Forms γ' Ni3(AI, Ti)	Al, Ti				
Raises solvus temperature of γ'	Co				
Hardening precipitates and/or intermetallics	Al, Ti, Nb, Ta				
Oxidation resistance	Al, Cr, Y, La, Ce				
Improve hot corrosion resistance	La, Th				
Sulfidation resistance	Cr, Co, Si				
Improves creep properties	B, Ta				
Increases rupture strength	В				
Grain-boundary refiners	B, C, Zr, Hf				
Retard γ' coarsening	Re				

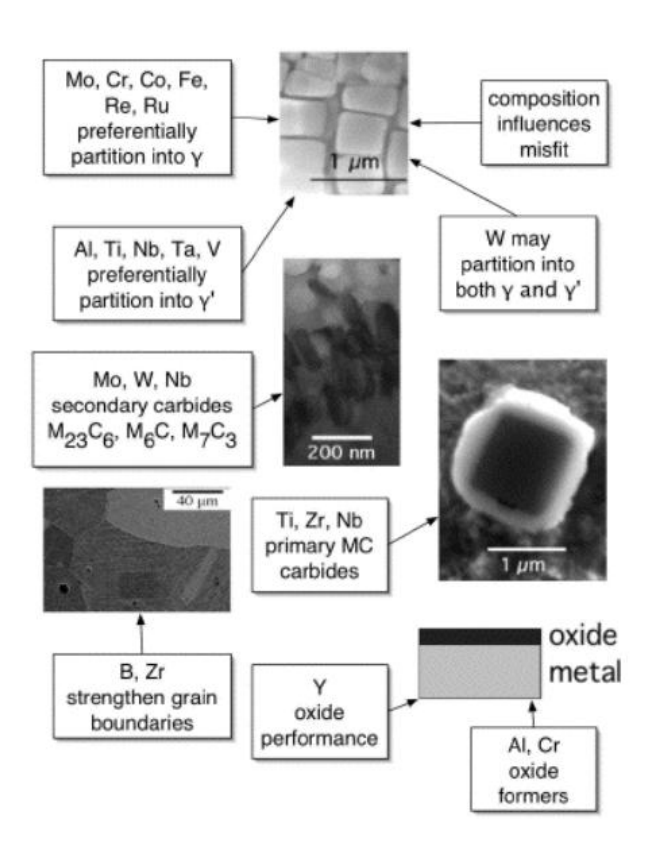


Figure 1.21. Alloying element effects in nickel based superalloys [10].

1.2.5 Inconel 939

IN939 is a corrosion resistant nickel-base superalloy designed for long lifetimes at service temperatures up to about 850 °C. The alloy has been developed for manufacturing gas turbine blades/vanes, fuel nozzles, casings, and some other high temperature applications [23]. The chemical composition is reported in *Table 1.3*.

Table 1.3. Chemical composition of INC939 (wt%).

	Ni	Cr	Co	Ti	W	Al	Ta	Nb
min	balance	22%	18%	3%	1%	1%	1%	0.5%
max	balance	23%	20%	4.5%	3%	3%	1.8%	1.5%

Inconel 939 (also known as Nimocast 739), which is a high- chromium-content superalloy developed by Inco Europe Ltd. This alloy has an adequate strength (γ ' former) at operating temperatures of up to 950°C. IN939 and similar superalloys, such as IN718, IN625 and Ren' e 220, form Cr2O3 scales through the preferential oxidation of Cr, which protects the metal against high temperature corrosion. The formed chromia layer is usually dense and slow-growing, obeying the parabolic rate law and exhibiting a long service lifetime at operating temperatures of up to 1000°C. When in service, the Cr2O3 layer is subjected to stresses, especially under cyclic conditions, which may result in the spallation of this layer. The spalled regions can be healed by re-formation of the Cr2O3 layer, if the alloy can supply sufficient Cr to the surface of the alloy [25].

The mechanical properties (at low and high temperatures) of the superalloys are attributed directly to the precipitation of some phases in the solid state during the fabrication, the ordered intermetallic γ' [Ni₃(Al,Ti)] consider as a first reaction phase and in minor quantity but not less important MC which precipitate within the grains and in the grain limits and M₂₃C₆ carbides which precipitate in the grain limits. It is well known strengthening of these alloys is achieved as a result of coherency strains, distribution and size of the particles and high-volume fraction of γ' [24]. The percentage of γ' also positively influences the creep-rupture life, as shown in *Figure 1.23*, where it is possible to appreciate the increasing trend of the creep-rupture life as the percentage of the phase in the alloy increases. Solid solution strengthened alloys (e.g., Hastelloy X), as well as low volume fraction precipitation hardened alloys (e.g., IN718) are generally considered weldable. Conversely, alloys containing high amounts of titanium and aluminum (y' forming elements), have been traditionally referred to as "hard-to-weld" or "nonweldable" alloys. The weldability limit of these materials has been empirically defined based on the combined content of titanium and aluminum, as shown in *Figure 1.22*.

IN939, inside the red box in the figure, is a type of nickel superalloy that falls into "hard-to-weld" group [4].

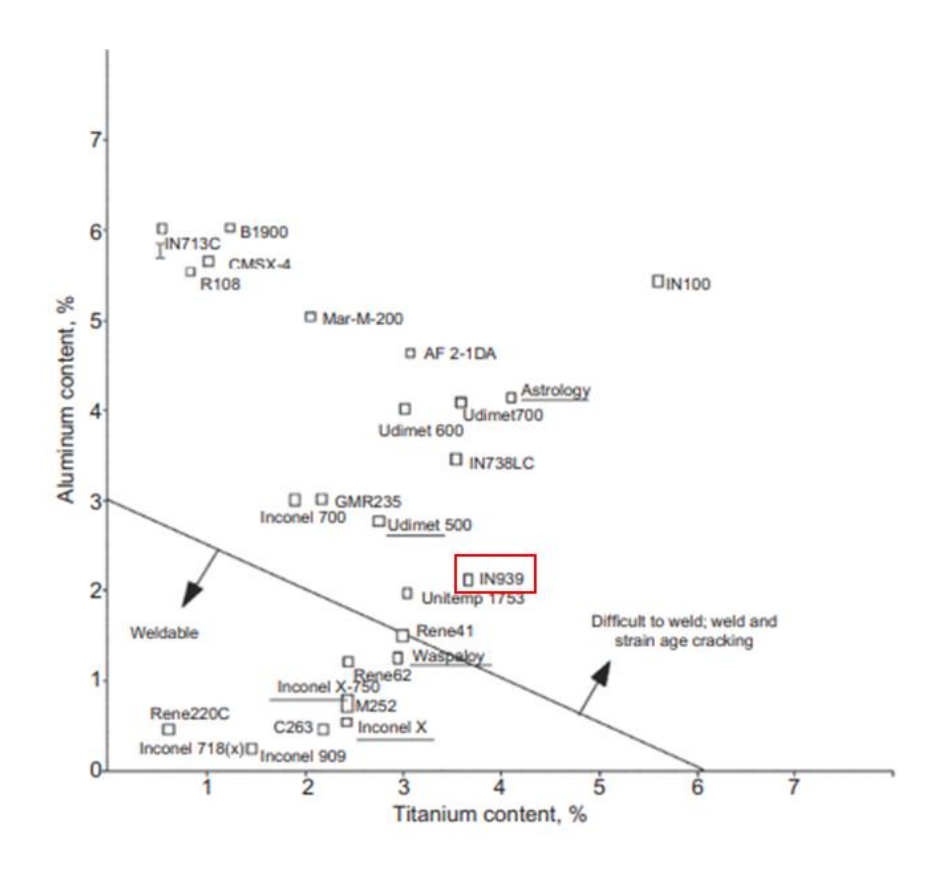


Figure 1.22. Weldability diagram based on Ti and Al content. IN939 highlighted in the red box [4].

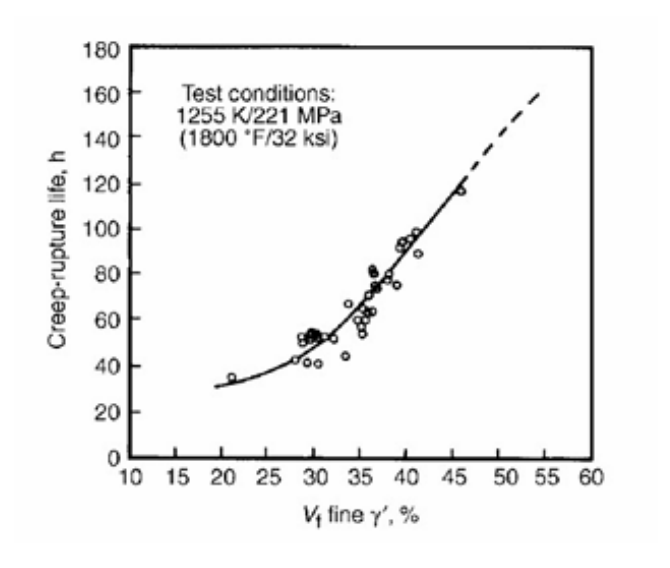


Figure 1.23. Effect of gamma prime on creep-rupture life [1].

A scientific study conducted creep resistance tests on the IN939 alloy, observing that specific stress levels at fixed temperatures did not induce phase instability in the alloy. These tests were carried out over a duration of 500 hours under the following sets of temperature-stress conditions: $600 \, ^{\circ}\text{C} / 750 \, \text{MPa}$, $700 \, ^{\circ}\text{C} / 400 \, \text{MPa}$, and $800 \, ^{\circ}\text{C} / 150 \, \text{MPa}$ [23].

1.3 Manufacturing processes

There is a strong motivation to develop new alloys that are capable of operating at higher temperatures to realize improvements in thermal efficiency, which are necessary to achieve environmental targets for reduced emissions of harmful green-house gases [26]. A major use of nickel based superalloys is in the manufacture of aeroengine turbine blades. A single-crystal blade is free from γ/γ grain boundaries. Boundaries are easy diffusion paths and therefore reduce the resistance of the material to creep deformation. The directionally solidified columnar grain structure has many y grains, but the boundaries are mostly parallel to the major stress axis; the performance of such blades is not as good as the single-crystal blades. However, they are much better than the blade with the equiaxed grain structure which has the worst creep life. Superalloy blades are used in aeroengines and gas turbines in regions where the temperature is in excess of about 400°C, with titanium blades in the colder regions. This is because there is a danger of titanium igniting in special circumstances if its temperature exceeds 400°C. Turbine blades are attached to a disc which in turn is connected to the turbine shaft. The properties required for aeroengine discs are different from that of a turbine, because the metal experiences a lower temperature. The discs must resist fracture by fatigue. Discs are usually cast and then forged into shape. They are polycrystalline. [10]. Traditional cast-wrought superalloys have been challenging in cogging due to element segregation. However, additive manufacturing technology is anticipated as a novel method for producing low-segregation superalloys. Additive manufacturing (AM) represents a class of manufacturing using a digital approach to product designing and production, making it a bottom-up process of manufacturing. In contrast to traditional manufacturing, which, in most cases, adopts subtractive or formative manufacturing approaches, AM processes, as suggested by the name, allow manufacturing parts by cumulative addition of the material layer by layer to realize the shape of interest.

All these manufacturing techniques cited above are presented in the next chapters.

1.3.1 Cast and Wrought processes

Vacuum induction melting (VIM), vacuum arc remelting (VAR) and electroslag remelting (ESR) are used in the production of nickel and iron-nickel based superalloy ingots. In the VIM process, liquid metal is processed under vacuum in an induction heated crucible. VIM is used as the initial melting method to reduce interstitial gases to low levels, enable higher and more controllable levels of the reactive strengthening elements aluminum and titanium, and eliminate the slag or dross problem inherent in air melting. After initial VIM processing, the alloys are then remelted using either VAR or ESR. Vacuum induction melting is used to produce the desired alloy composition. Feedstock for VIM includes pure elements, master alloys and recycled scrap. VIM is used to remove dissolved gases (oxygen, nitrogen and hydrogen) and other impurities before the addition of reactive alloying elements to the melt. Ceramic filters are also used to remove large oxide and nitride inclusions during the final pour. The VIM process may be the only melting process if the ingot is going to be remelted for casting; however, if the ingot is going to be hot worked, it must be secondarily melted, because VIM ingots generally have coarse and non-uniform grain sizes, shrinkage and alloying element

segregation that restricts hot workability during forging. Vacuum arc remelting and electroslag remelting are used to further refine the ingot after initial VIM processing. In the VAR process, an arc is struck between the end of the ingot electrode and the bottom of a water cooled copper crucible. The arc generates the heat to melt the end of the electrode which drips down into the crucible. In the ESR process, remelting does not occur by striking an arc; instead, the ingot is built-up in a water-cooled crucible by melting a consumable electrode that is immersed in a slag that is heated by resistance heating. The ESR process does not require a vacuum since the molten metal is protected from the atmosphere by the slag covering. Therefore, a triple melting process (VIM-ESR-VAR) is used for producing large ingots for forging stock for gas turbine components, as shown in *Figure 1.24* [27].

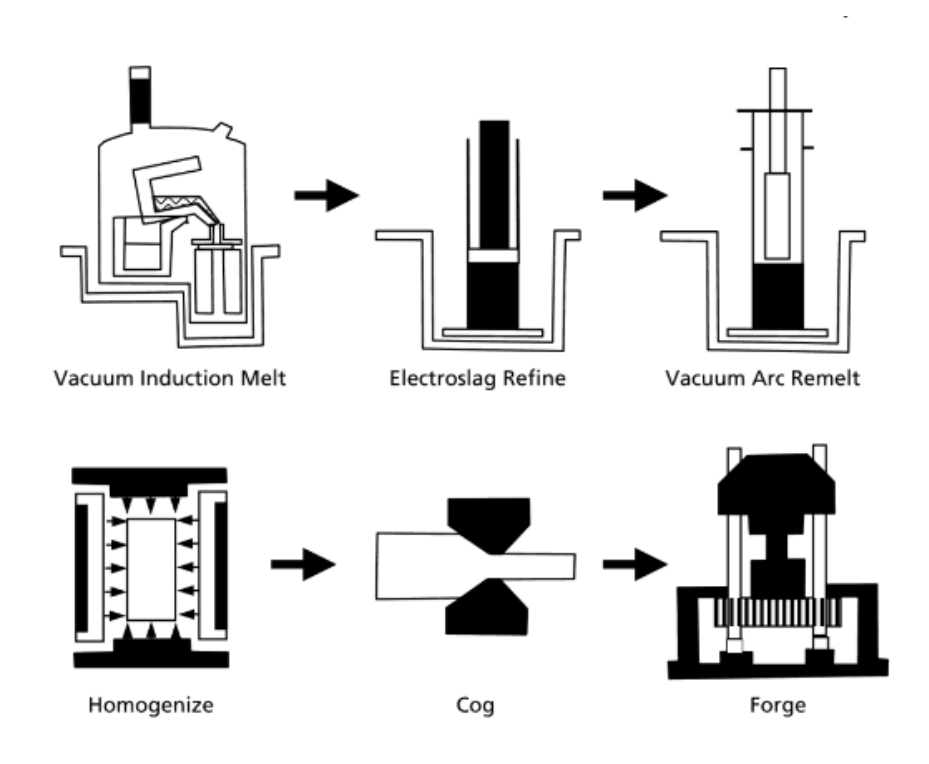


Figure 1.24. Forged superalloys by Ingot Metallurgy [27].

Because of their strength retention at elevated temperatures, superalloys are more difficult to forge than most metals. In reality, forgeability varies widely depending on the type of superalloy and its exact composition. For example, some of the iron-nickel based alloys, such as A-286, are similar to the austenitic stainless steels. At the other extreme, some superalloy compositions are intrinsically so strong at elevated temperatures that they can only be processed by powder metallurgy or by casting. In general, as the alloying content has been increased to obtain even greater elevated temperature strength, the forgeability has been degraded, i.e. the γ' strengthened alloys are much more difficult to forge than the solid solution strengthened alloys. Forging of superalloys has evolved from the simple process of making a specific shape to a very sophisticated one that not only fabricates the correct shape but also imparts a great degree of microstructural control for enhanced properties. Superalloy billets are usually furnace heated for hot forging. Although nickel base alloys have a greater resistance to scaling at hot working temperatures than steels, they are more susceptible to attack by sulfur during heating. Cleanliness is extremely important. All potential contaminants, such as lubricants and paint markers, must be removed before heating. Low sulfur fuels must also be used. Gas fuels, such as natural gas, butane and propane, are the best fuels. Oil is also a satisfactory fuel provided it has low sulfur content. Since the mid-1960s, the hottest parts of the engine, the blades (rotating) and vanes

(non-rotating), have been manufactured by investment casting. As the alloy content of nickel based superalloys was continually increased to obtain better creep and stress rupture capability, the alloys became increasingly difficult to forge. To allow even higher contents of alloying elements, it became necessary to change the fabrication process to casting. Investment casting became the process of choice because it is amendable to the fabrication of hollow blades with intricate cooling passages, which allows higher operating temperatures. Since the mid-1980s, turbine inlet temperatures have increased by 500° F. About half of this increase is due to more efficient designs, while the other half is due to improved superalloys and casting processes. The introduction of directional solidification allowed about a 50° F increase in operating temperature, while the single crystal process produced another 50° F increase. [27].

As shown in *Figure 1.25*, increases in operating temperature for superalloys have increased over the past seven decades and this improvement relies heavily on the microstructure of the alloy. Wrought alloys were improved through conventional casting. The creep resistance was then improved through directional solidification followed by single crystals of the alloys. Decreasing the number of grains in the alloy significantly reduces the creep tendencies at high temperature.

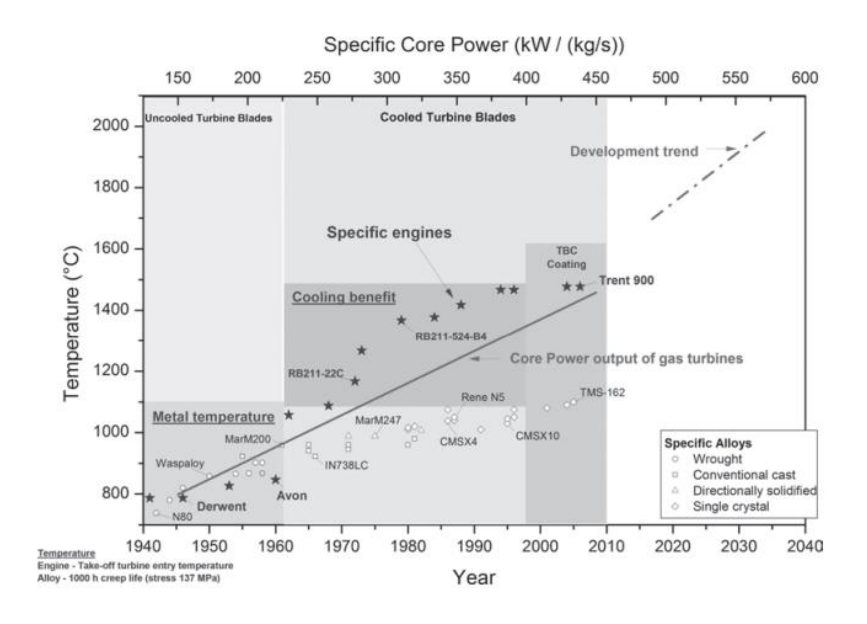


Figure 1.25. Evolution of the high temperature capability of Ni-based superalloys in the last 70 years [28].

1.3.2 Additive manufacturing

Additive manufacturing (AM), also commonly called 3D printing, paves the way for new possibilities in the production of end-use, multi-component, and multi-material parts that are difficult to manufacture with conventional technologies. In the last few years, the AM sector has experienced a tremendous increase in interest, both in the scientific and commercial field. The main reasons for the growing interest are that complex and expensive models or molds no longer have to be produced and only the guidance of a computer-aided design model is required as well as materials with unique physical, mechanical, or chemical properties can be prepared. Other reasons are of an economic

ecological nature. AM technologies allow substantial financial and time savings and reduce critical raw material waste. Owing to excellent mechanical properties at elevated temperatures, nickel-based superalloys are key material in gas turbines, turbocharger rotors, parts of nuclear reactors, liquidfueled rockets, and many others. AM makes the microstructure different from those of traditional processes, such as casting and forging, proposing unique and app-tailored mechanical proper ties. The microstructure is often metastable. The formation of the principle strengthening phase (γ' precipitates), that is, allowing superalloys to be used at temperatures up to even 90 % of their melting point, is in the as-built microstructure but limited owing to solid-state cracking. To trigger precipitation of γ' precipitates, appropriate heat treatment needs to be applied. The present study investigates the effect of heat treatment and building direction (BD) on the microstructure and basic mechanical properties of IN939 superalloy produced by direct metal laser sintering [29]. Main applications of additive manufacturing include rapid prototyping, rapid tooling, direct part production and part repairing of plastic, metal, ceramic and composite materials. The two main parameters of any metal AM process are type of input raw material and energy source used to form the part (Bhavar 2014). Input raw material can be used in the form of metal powder or wire whereas laser/electron beam or arc can be used as energy source [30]. Figure 1.26 shows an additive manufacturing process.

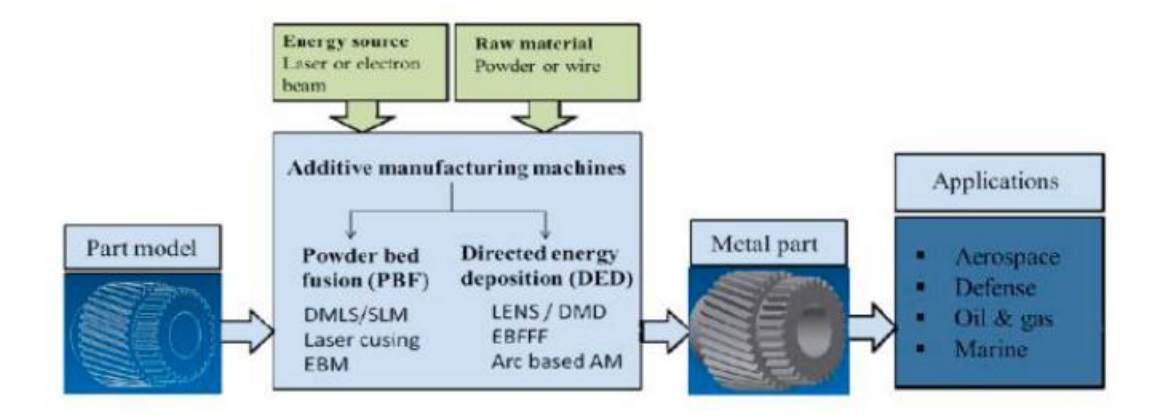


Figure 1.26. Common metal additive manufacturing process [30].

One widely used additive manufacturing technology for metals is Powder Bed Fusion (PBF), as shown in Figure 1.26. Thermal energy selectively fuses regions of powder bed. Selective laser sintering/melting (SLS/SLM), Direct Metal Laser Sintering (DMLS) laser cusing and electron beam melting (EBM) are main representative processes of PBF based technologies reported in Figure 1.27. Under PBF process, DMLS is an additive manufacturing (AM) or rapid prototyping (RP) process that uses metal powder and a high power laser to sinter together a usable part. This method is capable of producing very dense parts but in order to achieve gas or pressure tightness, post-treatment is often required. Most tradenames such as laser sintering, cusing etc. are describing the same process but not different technologies. The process is very similar to an existing AM process called Selective Laser Sintering (SLS), both SLS and DMLS are conceptually the same process, but instead of using polymers or coated metal powders in the case of SLS, DMLS uses uncoated pre-alloyed metal powders as the sintering material. Electron beam melting (EBM) technology uses a heated powder bed of metal in a vacuum that is then melted and formed layer by layer using an electron beam energy source similar to that of an electron beam welding/electron microscope [30].

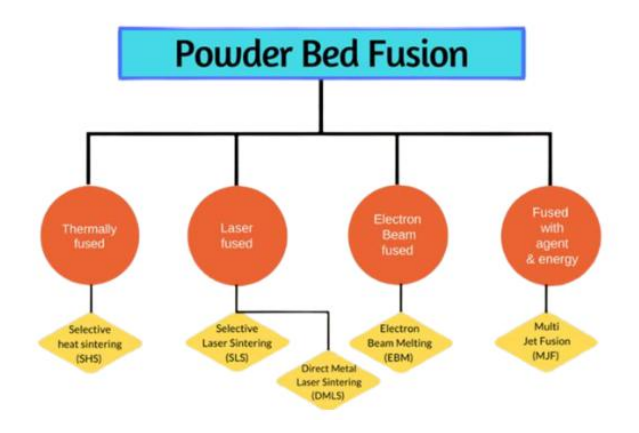


Figure 1.27. Powder Bed Fusion Types [31].

1.3.2.1 LPBF (Laser Powder Bed Fusion)

Powder bed AM processes that utilize laser beams as the heat source date back to as early as the 1990s with the emergence of laser sintering processes. With the development of the technology, higher-intensity lasers were then utilized to achieve full melting of metals in the early 2010s. It was then referred to as selective laser melting, a name that was later changed to laser powder bed fusion (L-PBF) by ASTM [32]. Laser Beam Melting, standardized as Laser Powder Bed Fusion (LPBF), is the most used AM process for metals, within Powder Bed Fusion technologies. Whit LPBF is possible to produce functional near net shape parts with enhanced mechanical properties. Realization of the 3D solid part occurs by melting successive thin metal powder layers (20-80 µm) through the application of a concentrated laser beam, resulting in the fast cooling of the molten alloy.

The operational concept of L-PBF along with the general architecture of its system can be seen in *Figure 1.28*.

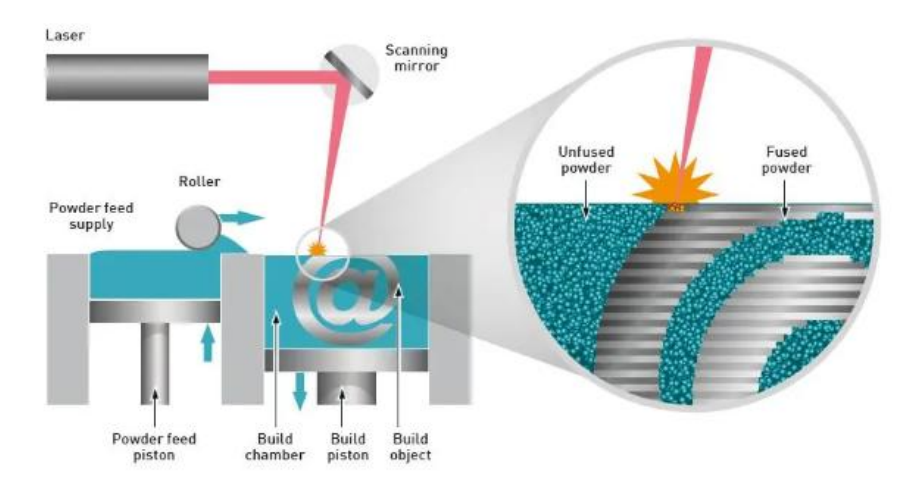


Figure 1.28. A schematic of the basic architecture of an L-PBF system [33].

After the 3D CAD model (STL file) is sliced into layers of equal thickness using a relevant software package, the feedstock material in powder form is laid down on a platform in the form of thin layers,

typically around 15-45µm, depending on the material. The layer thickness corresponds to the thickness of each slice of the STL file prepared for printing. The layer thickness must ensure that it is thin enough to enable full melting of each individual layer while also enabling bonding to the previous layer and being large enough for high productivity. The build plate onto which the powder is deposited and processed usually has the capacity to be heated up to aid in reducing the residual stresses and part curling or warping. Nevertheless, support structures are used to anchor the part being fabricated to the build plate to aid in heat dissipation. Most machines enable heating the build plate up to 200°C, with some machines now offering a capability of up to 500°C and fewer ones offering 1200°C. After depositing the layer of powder, a laser beam is controlled to scan across that layer and selectively melt the regions of interest, line by line according to the information from the CAD model. The build plate is then lowered, and the earlier described steps are repeated until the full part is built. In laser powder bed fusion, the process must operate under an inert atmosphere to protect the molten metal from oxidation. Therefore, the processing chambers are typically filled with an inert gas, such as argon, nitrogen, or, the less common option, helium, prior to starting the manufacturing process. The type of gas used has been reported to affect the defect and porosity content, microstructure, and residual stresses to various extents, depending on the material being processed. L-PBF powder beds operate at room temperatures, i.e., only the building plate is heated and not the whole powder bed [32].

Much research is focused on optimizing these parameters to enable the production of fully dense defect-free parts. The most critical and commonly studied process parameters are represented in *Figure 1.29* and include:

- Laser power: the energy irradiated on the material by the laser beam.
- Scan speed: speed by which the laser beam scans the powder bed, which is dictated by both
 exposure time and point distance deployed while irradiating the powder bed with the laser
 beam.
- Hatch spacing: the distance between the center point of two neighboring scan tracks, defining the overlap between every two adjacent melt pools.
- Layer thickness: the thickness of each layer of powder deposited onto the build plate for laser irradiation. This is equivalent to the thickness of the slices in the STL file prepared for printing.
- Scan strategy or pattern: this parameter defines the movement of the laser beam as it scans the powder bed.

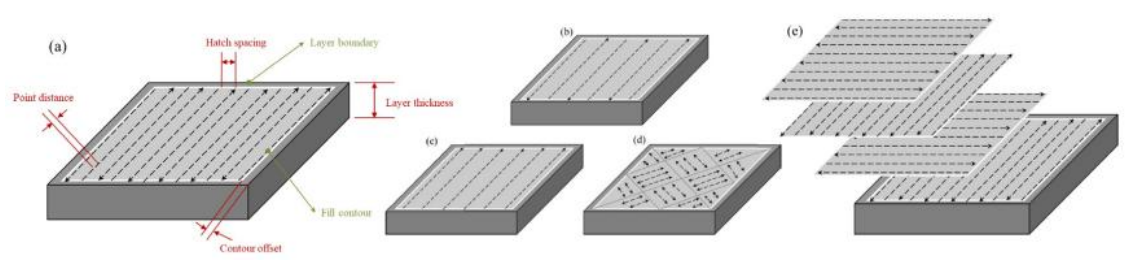


Figure 1.29. Geometrical process parameters in L-PBF processing: (A) an illustration of the hatch spacing, point distance, and layer thickness. Examples of various scan patterns in (B) meander, (C) unidirectional, and (D) checkerboard scan patterns. (E) Depictions of an alternating scan strategy in which the scan direction is rotated between layers by a 90 degree rotation [32].

Three types of defects typical of LPBF are: lack of fusion (LoF), gas entrapped pores and keyhole pores. LoF is generated by the lack of overlap between laser hatches or by insufficient energy input. Keyhole pores appear when the laser power is high enough to cause evaporation of metal at the bottom of melt pool. Gas pores originate from bubbles of inert gas entrapped in the melt during fusion of the powder bed and/or from gas entrapped inside the feedstock material. These types of defects are represented in *Figure 1.30* (a) as a function of process parameters and (b) their morphology.

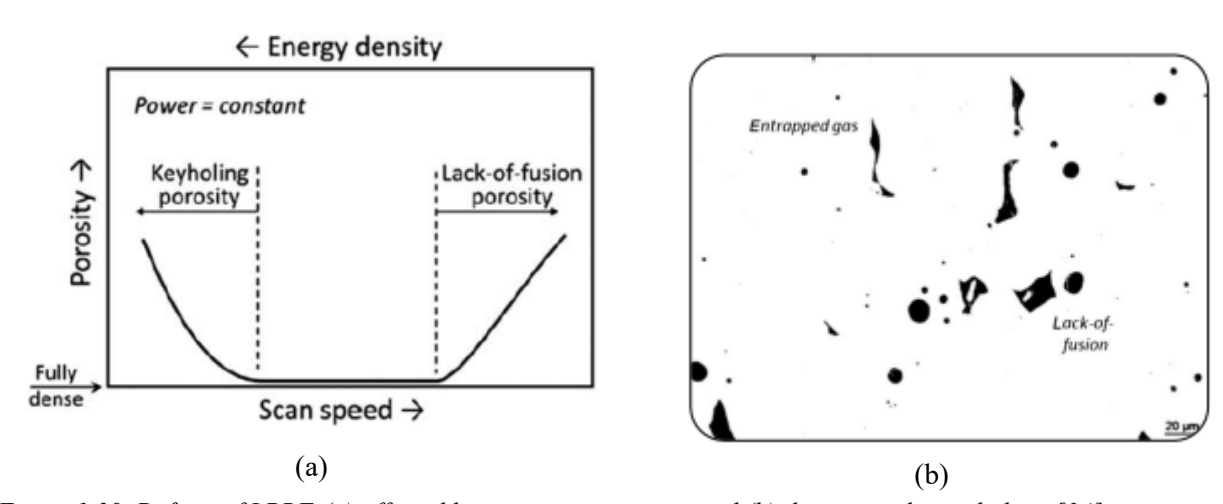


Figure 1.30. Defects of LPBF, (a) affected by process parameters and (b) their typical morphology [34].

The microstructure of In939 obtained by LPBF (as built condition) is reported in Figure 1.31. The process consists of multiple laser scanning and generates a microstructure in which the laser tracks can be identified in the XY plane, perpendicular to the building direction (BD), XZ. These tracks appear as melt pools.

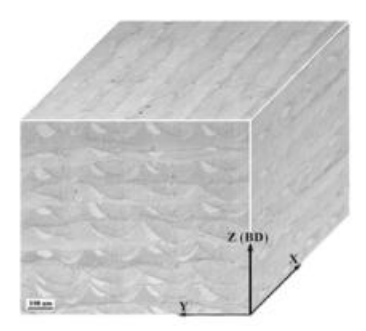


Figure 1.31. Three dimensional optical metallograph composite of the as-built sample, BD: building direction, [43].

For this work all samples that have been analyzed and studied were produced by Laser Powder Bed Fusion technology and were supplied by Siemens Energy AG.



Figure 1.32. Turbine blades produced by LPBF [36].

1.4 Heat treatments in Ni-based superalloys

In numerous applications involving superalloys, the component's microstructure must be altered to optimize key material properties or to condition it for further manufacturing steps. Among the most prevalent techniques employed for this purpose is the application of a controlled heat treatment. To optimize properties (often of a coating-metal system), nickel based superalloys are, after solution treatment, heat treated at two different temperatures within the γ/γ phase field. The higher temperature heat treatment precipitates coarser particles of γ . The second lower temperature heat treatment leads to further precipitation, as expected from the phase diagram. This latter precipitation leads to a finer, secondary dispersion of γ . The net result is a bimodal distribution of γ illustrated in *Figure 1.33* [10].

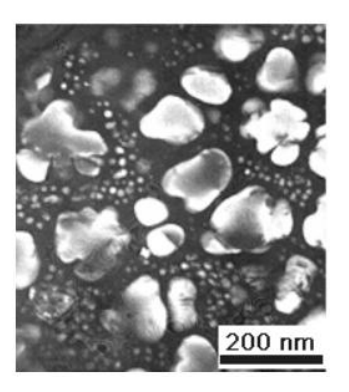


Figure 1.33. Bimodal distribution of y' in nickel superalloys [10].

1.4.1 Typical heat treatments

Heat treatment procedures for nickel-based superalloys are applied to achieve chemical homogenization and to control the grain structure. Heat treatment is an important method for modifying the morphology of the precipitates in superalloys. Each treatment has a precise objective and depends on the temperature and time setting.

The annealing treatment makes it possible to increase the ductility of the material, relieve post-welding stresses, improve the homogeneity of the microstructure thanks to static recrystallization. It also prepares the material for welding, relieves stresses after welding or soften age hardened structures by resolution of second phases [37].

Stress relieving treatment is performed on superalloys in order to reduce the stress carried by the material after the fabrication process. Temperatures used in this treatment are usually below the annealing or recrystallization temperatures, in order to avoid microstructural changes. Generally, temperatures for Ni-based superalloys vary between 675 °C and 900 °C and with dwell times between 1 and 4 hours. Annealing, as well as stress relieving, has specific parameters for each alloy. *Table 1.4* shows some parameters for stress relieving and annealing of some nickel-based superalloys [1].

Table 1.4. Typical stress relieving and annealing cycles of Nickel-based alloys [1].

	Stre reliev		Annealing		
	T[^C]	h	T['C]	h	
Astroloy	*	-	1135	4	
Hastelloy X	*	-	1175	1	
Incoloy800	870	1.5	980	1/4	
Incoloy800H	-	-	1175	-	
Incoloy825	-	-	980	-	
Incoloy 901	*	-	1095	2	
IN600	900	1	1010	1/4	
IN601	-	-	980	1	
IN625	870	1	1040	1/2	
IN718	-	-	955	1	
IN X-750	*	-	1035	1/2	
Nimonic 80A	880	-	1080	2	
Nimonic 90	*	-	1080	2	
Rene 41	*	-	1080	2	
Udimet 500	*	-	1080	4	
Udimet 700	*	-	1135	4	
Waspaloy	*	-	1010	4	

Solution heat treatment is performed at higher temperatures compared to stress relieving and annealing treatments, arriving near to the incipient melting temperature of the alloy. These temperatures may range from about 980 °C to 1230 °C. The main goal of this treatment is intended to dissolve second phases to produce maximum corrosion resistance or to prepare an alloy for subsequent aging.

Aging treatments strengthen age-hardenable alloys by the precipitation of additional quantities of different phases from the supersaturated matrix developed by solution treating. The desirable phases for optimal mechanical properties are precipitates such as γ ', γ " and secondary carbides. In Ni-based superalloys, γ ' and γ " precipitate from the γ matrix when subjected to double aging treatment in the range of 600-900 °C [43].

Table 1.5 shows a typical four stage heat treatment of IN939.

Table 1.5. Typical four stage heat treatment of IN939.

Heat treatments	Microstructure
as-cast	Cored dendritic (dendrite core Co-Cr-W-rich, Ti-Ta-Nb interdendritic) Primary MC 8 Plates of η clusters in interdendri tic regions γ'/γ eutectic islands, some primary γ' formed on cooling Shrinkage pores (up to 0.3%)
1 stage: solutioning 4h/1160 C/fast air cooled	Homogenisation of γ matrix Dissolution of γ' η rounded or dissolved Primary MC unchanged, secondary MC formed on cooling Fine γ' formed on cooling (20nm)
2 stage 6h/1000°C/fast air cooled	Precipitation of primary γ' (70-150nm) precipitation of MC at grain boundaries
3 stage 24h/900°C	Growth of primary γ' Precipitation of M23C6 on grain boundaries in form of strings of discrete particles
4 stage 16h/700°C	Precipitation of fine γ' to result in bimodal particle size distribution (150nm+20nm) Slight increase in amount of M23C6

1.4.2 Hot isostatic Pressing (HIP)

Hot isostatic pressing (HIP) is a manufacturing process that involves simultaneous application of high temperature and pressure. It was invented in 1955 for diffusion-bonding applications in the nuclear industry and has since found numerous applications in other fields [40].

Hot isostatic pressing (HIP) involves the simultaneous application of iso-static pressure and elevated temperature to a workpiece, which results in the workpiece (usually powder) becoming consolidated. The pressure medium used is an inert gas such as argon or nitrogen, which is pumped into a pressure vessel and pressurised to up to 200 MPa, whilst a furnace in the vessel produces tem- peratures of up to 2000 °C. The workpiece is usually encapsulated in an evac- uated capsule of sheet metal, ceramic or glass. With HIP, it is possible to give service parts a further heat-treatment under pressure so that the precipitate structures are restored and internal damage is repaired. Some success has been claimed also for the repair of fatigue-induced damage, creep damage. It has been established that HIP is capable of healing casting defects such as shrinkage cavities, hot tears or micropores, hence it is expected that HIP processing can also close creep voids in service-exposed parts: this has been documented extensively by many researchers. Nickel-based superalloys are strengthened by the presence of precipitated Ni₃A1 (γ') in the grain interiors and the intermetallic γ' phase and carbides are also precipitated along grain boundaries, thereby raising creep resistance. Elevated service temperatures over long duration, however, can alter the microstructure, the γ ' particles coarsening and becoming elongated in the direction of loading. Grain-boundary carbides also agglomerate, forming continuous brittle films. Creep-induced cavities may also form at grain boundaries of transverse orientation with respect to the direction of applied stress, the linking of creep voids then leading to microcrack formation. These changes may be reversed by a combination of HIP and further heat-treatment. The HIP pressure heals the structural discontinuities in a manner similar to that for the healing of castings. The selection of the HIP temperature and further heat-treatment cycle must take into consideration the formation of serrated grain boundaries, carbide precipitate morphology, and the size and shape of the γ ' particles. [40]. Figure 1.34 shows the increase in stress rupture properties of Inconel X-750 blades after HIP re-heat treatment,

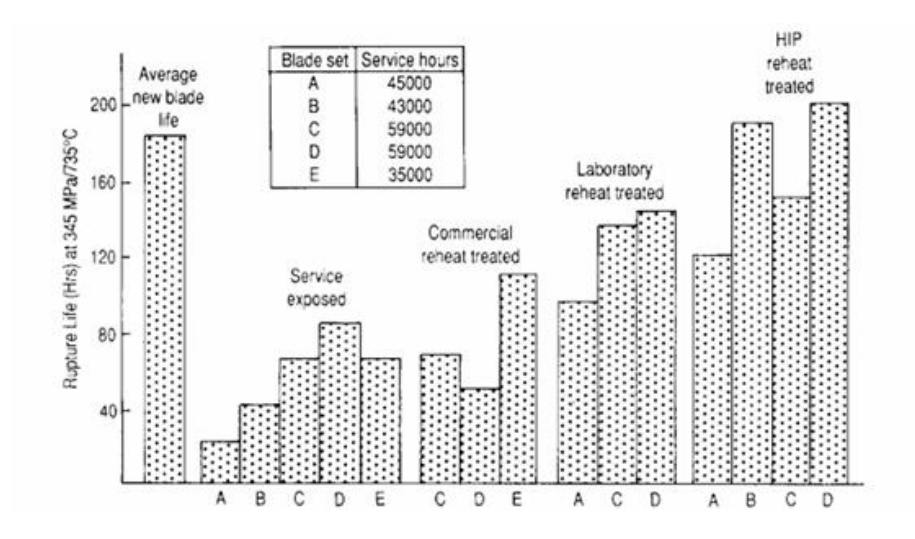


Figure 1.34. Stress-rupture properties from several sets of Inconel alloy X-750 blades after various treatments compared to the average new blade life [40].

An investigation of as-printed and heat treated IN718 superalloy shows as result of heat treatment, γ [Ni3(Al,Ti,Nb)] and γ " (bct-Ni3Nb) phases that dissolved in the matrix (Ni-Cr solid solution) and the needle-like-phase that formed at the grain boundaries. The tensile properties of the heat treated SLM-printed specimens were found comparable to those of the wrought IN718 alloys. The HIP-treated microstructures showed more pronounced columnar precipitates with partially "recrystallized" structure. Whereas the microstructure of annealed specimens (1160 C, 4 h) showed ~50% "recrystallized" structure with spheroidal precipitates distributed in a dense field of fine precipitates. It is worth emphasizing that Amato et al. used the term "recrystallization" to describe the change from dendritic to equiaxed structure. The microstructure of the HIP-treated IN718 alloy is shown in Figure 14, where more equiaxed grains and a higher volume fraction of carbide precipitates at the grain boundaries are present compared with the homogenized structure. It can be depicted that γ " precipitates are completely dissolved in the γ phase matrix due to the HIP treatment further exposed the material to high temperature, holding time and pressure thereby accelerating the γ " phase dissolution [41].

The range of HIP temperature, pressure, and time depends on the alloy type and the expected properties. HIP atmosphere is mostly argon gas. The presence of oxidizing elements in HIP atmosphere reduces creep and fatigue properties. *Table 1.6* gives a general overview of HIP impact for different superalloys.

Table 1.6. Range of HIP temperature, pressure, and time; type of atmosphere; heating and cooling rate and its impact on the properties of different superalloys [42].

Material	Tempe			sure Pa		Heating	Environment	Durations	Ref	Remarks
	max	min	max	min	rate	rate				
GTD 111-DS	1230	890		120	0.17C/S	0.25C/S		4	[11]	Tensile strength increased 40% and toughness increased a little.
GTD 111-DS	1190	900		120	0.17C/S	0.25C/S		4	[12]	Mechanical properties did not change.
GTD 111-DS	1340	1330		120	0.17C/S	0.25C/S		4	[13]	Mechanical properties increased a little.
NiAl-28Cr-5.7Mo-0.3Hf		1300		150	0.17C/S	0.25C/S	Vacuum	3	[14]	Hardness increased 30%, strength increased 17% and toughness increased 4 times.
CM247LC	1320	1100		150					[15]	Fatigue strength and tensile strength increased slightly at 1260 C.
Inconel 738		1200		100				5	[16]	Mechanical properties of used Inconel 738 increased to new one.
Inconel 718		1200		120				3	[17]	Strength did not change but elongation reduced 50%.
Inconel 718		1200		120				3	[18]	Creep resistance reduced because of oxygen in environment.

1.5 Incipient melting

Knowledge of the temperature marking the very onset of melting is crucial to the control of superalloy processing and utilization. It has long been known that small amounts of liquid play havoc with the workability of superalloys; hot shortness thus causes severe cracking. This severe sensitivity to the presence of a small amount of liquid is undoubtedly aggravated by the "stiffness" and poor thermal

conductivity associated with the high alloy content of superalloys. Lack of space does not permit a full exposition here of the limits posed on the workability of superalloys by incipient-melting. The most dramatic example of this effect, however, is presented by Inconel 718, for which forging temperatures must be strictly limited to a maximum of 1120 C (2050 F). This is because the 5% Nb content of this alloy causes some eutectic liquid to persist to very low temperatures, at which point Laves phase is formed. During heating at 10°C/min, DTA reveals a distinct melting reaction in this region at 1130°C (2066 F) in *Figure 1.35*. The more general melting process begins at a moderate rate at 1175 C (2147 F) and at a stronger rate at 1223 C (2233 F) [44].

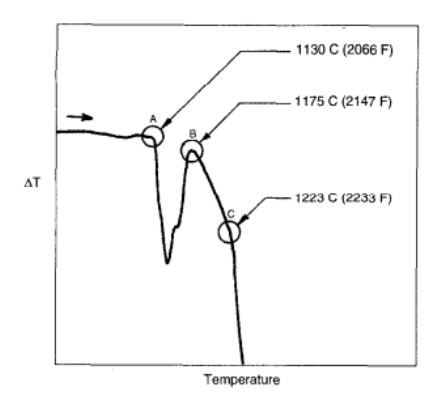


Figure 1.35. Distinct low-temperature melting reaction in Inconel-718, occurring at 1130 °C (2066 F) during heating at 10 °C/min. The more-general melting reaction begins at a moderate rate at 1175 °C (2147 F), and at a stronger rate at 1223 °C (2233 F) [44].

Knowledge of the incipient melting temperature is critical to the control of superalloy processing and its utilisation. One of the appropriate methods to study the effects of heat treatment on the microstructural features of IN939 superalloy, especially its incipient melting temperature, is thermal analysis (i.e. differential thermal analysis and DSC). Analysis by EDS showed that these local melted regions are rich in elements Zr and B and to some extent in Nb and Ti. Analysis of several incipient melted regions near the η phase showed that the overall composition of these regions is as follows, in which the subscripts represent the atomic percentage of related elements (Ni₃₀₋₄₅,Co₁₀₋₁₆, Cr₁₅₋₃₀)(Zr₇₋₁₁,Nb₃₋₇,Ti₄₋₈,B,Si,Al) [45]. *Figure 1.36* shows a morphology of incipient melting region.

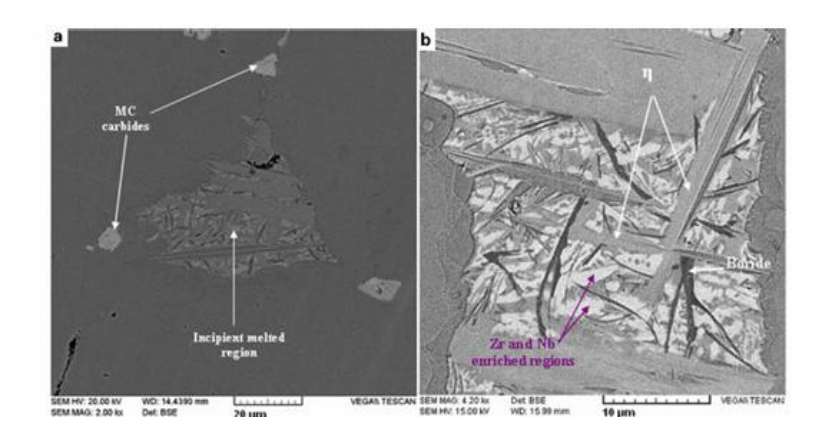


Figure 1.36. a, b SEM microstructures with different magnifications [45].

CHAPTER 2

Materials and methods

In this chapter, an extensive description of the laboratory testing methods is presented, including the metallographic sample preparation process and the instruments employed.

2.1 Description of IN939 analyzed

This thesis focuses on the analysis of Inconel ® 939, a nickel-based superalloy supplied by Siemens Energy AG. In particular, the material was produced in cylinder form by Laser Powder Bed Fusion technology, using the EOS M290 machine with process parameters optimized through Siemens Energy AG internal developments that remain confidential.

The sample shape is shown in the figure below.



Figure 2.1. Draw of LPBF cylinder sample.

2.2 Metallographic preparation of sample

In order to evaluate the microstructure of the IN939 specimens, in the as-built and post heat treatment state, a metallographic preparation was carried out structured as follows:

- 1. Cutting of the specimens into two sections, XY and XZ planes as shown in *Figure 2.2*, by means Remet MT60 cut-off machine;
- 2. Embedding of the sections by means of Hergon MI30 encapsulating press;
- 3. Polishing of the surfaces by means of Mecatech 234 polishing machine;
- 4. Chemical attack with oxalic acid (C₂H₂O₄), Kalling's N.2 solution and Marble, all suitable for nickel-based superalloys.

Precision cutting is a vital preparatory step to obtain the required cross-sections for microscopic examination. Careful sectioning with adequate coolant application is crucial to prevent both thermal-induced microstructural changes and specimen deformation. For this procedure, a precision sectioning system was used to ensure clean cuts while maintaining sample integrity.

As mentioned before, the sample is cylindrical, with a diameter of 14 mm and a height of 120 mm. To investigate the material properties along the two principal directions, particularly the building direction (Z-axis), the specimen was sectioned along the XY (transverse) and XZ (longitudinal) planes. This was achieved by initially dividing the original cylinder into smaller cylindrical segments, which were then bisected using a precision cutting machine. The cuts were performed both parallel and perpendicular to the building direction to allow directional analysis.

The schematic representation of cutting planes, XZ and XY, of the IN939 cylinder obtained by LPBF process is reported in *Figure 2.2*.

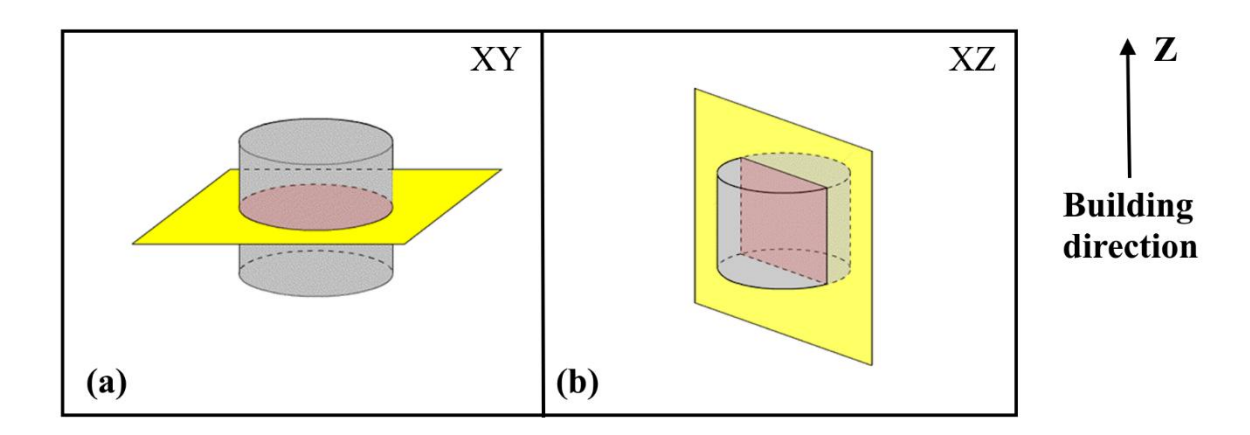


Figure 2.2. As-built IN939 sample representation of XY a) and XZ b) planes.

After sectioning the specimens, in order to facilitate the subsequent polishing step, the specimens are encapsulated within a thermosetting phenolic resin (20 ml) using a pneumatically driven Hergon MI30 encapsulating press.

The previously embedded specimens are then polished by means of an automatic Mecatech 234 polishing machine from Presi. Progressive finishing abrasive papers (grit 600,800, 1200) and cloths for polishing machine (6 μ m, 3 μ m, 1 μ m, colloidal silica) are sequentially used. During the initial coarse grinding and lapping steps, a force of 1.5 DaN was applied to the samples, whereas a reduced force of 0.8-1.0 DaN was used for the subsequent polishing stages with diamond suspensions.

Although proper polishing and subsequent cleaning of the specimen allows for microscopic images free of etching and sediment, often is not sufficient to highlight the microstructure of the specimen, especially the grains. It is necessary, therefore, to carry out a process of chemical attack on the surface of the sample, so as to create a contrast and make visible: shape and size grains, microstructural orientations, precipitates, inclusions and melt pools. Three different agents are used: Kalling's 2, Marble's reagent and oxalic acid 10%.

While all serve similar purposes, their distinct compositions and etching mechanisms make them suitable for different applications. Kalling's No. 2 reagent consists of a mixture of 5 g copper (II) chloride (CuCl₂), 100 mL hydrochloric acid (HCl), and 100 mL ethanol or methanol. This etchant is particularly effective for austenitic stainless steels and nickel-based superalloys, such as Inconel, where it highlights grain boundaries, annealing twins, and secondary phases like carbides and intermetallics. Its ability to delineate microstructural features in additively manufactured components makes it valuable for studying laser powder bed fusion (LPBF) microstructures.

Marble's reagent is composed of 10 g copper (II) sulfate (CuSO₄), 50 mL hydrochloric acid (HCl), and 50 mL distilled water. The etchant works through a redox reaction where copper deposits on the specimen surface, enhancing contrast between phases. Both etchants require careful handling due to their acidic nature, and proper rinsing with alcohol or water after etching is critical to stop the reaction. While these two reagents are used by depositing the reagent directly in the sample surface for a defined period of time and stopping the reaction by washing with water, followed by drying with

forced air, oxalic acid 10% is used for an electrolytic attack. The standard 10% solution is prepared by dissolving 10 grams of oxalic acid dihydrate (C₂H₂O₄·2H₂O) in 100 mL of distilled water.

This clear, colorless solution was used for electrolytic etching, performed using electropolishing machine ELLOPOL II by Persi. The 10% oxalic acid solution is typically used with a DC power supply at 6 volts (V) for 5-60 seconds, where the specimen serves as the anode and a stainless steel cathode completes the circuit. The etching process was performed at a fixed voltage of 3 V with a duration of a few seconds.

The result, achieved through sequential preparation steps, including coarse grinding, lapping, and diamond suspension polishing is presented in *Figure 2.3*. This optimized process followed by etching step ensures clear grain boundary delineation and artifact-free surface quality, enabling precise microstructural analysis.



Figure 2.3. Embedded and polished sample cross-sections

2.3 Specimens Analysis

Different instruments were used for the analysis of the specimen's microstructure. In this section the main three are presented. Following the polishing and etching procedures, this step is employed to accentuate grain boundaries, facilitating clearer microstructural analysis.

2.3.1 Optical Microscope

Microstructural characterization, including porosity assessment, grain size measurement, and general microstructure evaluation, was performed using a Leica optical microscope (Figure 2.4) equipped with a high-resolution digital camera. The system offers selectable magnifications of 50x, 100x, 200x, 500x, and 1000x, enabling detailed observation across multiple scales. Optical microscopy is a widely established technique for preliminary microstructural analysis due to its ability to provide rapid, high-contrast imaging of surface features without the need for vacuum conditions, unlike electron microscopy [12]. While the system offers both brightfield and darkfield imaging capabilities, the present analysis was conducted exclusively using brightfield microscopy to evaluate microstructural features.



Figure 2.4. Light optical microscope (LOM) Leica.

2.3.2 Scanning Electron Microscopy (SEM)

For high-magnification imaging and nanoscale microstructural analysis, a scanning electron microscope (SEM) was employed (*Figure 2.5*). Unlike optical microscopy which relies on visible light photons, SEM utilizes a focused beam of high-energy electrons (typically 1-30 keV) to achieve superior resolution down to nanometer scale. This electron-beam technique provides several analytical advantages, including higher resolution, great depth of field and elemental analysis capability through energy-dispersive X-ray spectroscopy (EDS). This last analysis leads to estimate the relative abundance of elements within the alloy matrix and precipitates. While EDS has inherent limitations (e.g., detection sensitivity and spatial resolution), it provides semi-quantitative compositional data, enabling the creation of elemental maps and localized point analyses. This combined approach revealed the chemical nature of precipitates and the approximate composition of the alloy matrix. Sem use also secondary and backscattered electrons for imaging. Backscattered electrons, generated by elastic scattering of the primary electron beam with sample atoms, exhibit higher energy than secondary electrons and penetrate several nanometers below the surface.



Figure 2.5. Zeiss Evo 15 Scanning Electron Microscope (SEM) [47].

Before SEM analysis a gold coating was performed to increase the conductivity of the sample preventing distortion of the image and damaging sample during the analysis leading to a better quality image. This sputter coating process involves placing the sample inside a small vacuum chamber. An inert gas, Argon, is introduced and then ionized into a plasma state by applying a high voltage between two electrodes, the target as cathode and the sample as anode.

2.3.3 Field-Emission Scanning Electron Microscopy (FESEM)

Field-Emission Scanning Electron Microscopy (FESEM) was also an investigation technology used in this analysis. It is an advanced imaging and analytical technique that utilizes a field-emission gun (FEG) to produce a highly focused, monochromatic electron beam with superior brightness compared to conventional SEMs. This technology enables exceptional resolution down to 0.4-1 nm, making it particularly suitable for characterizing nanoscale features. The FESEM's ability to operate at low accelerating voltages (typically 0.1-30 kV) minimizes sample damage while maintaining high image quality, especially for beam-sensitive specimens. The combination of high-resolution imaging and analytical capabilities makes FESEM an indispensable tool for comprehensive microstructural characterization, including grain boundary analysis, nanoparticle imaging, and defect identification in advanced materials [48]. The model used in this work is reported in *Figure 2.6*.



Figure 2.6. Zeiss Gemini Field Emissio Scanning Electron Microscope (FESEM) [47].

2.3.4 Electron Backscatter Diffraction (EBSD) Analysis

To thoroughly investigate the grain size distribution, core-shell dimensional differences, and crystallographic orientation, Electron Backscatter Diffraction (EBSD) analysis was performed using an Oxford instrument. This advanced technique is based on the diffraction of backscattered electrons from the sample surface, which obey Bragg's law, enabling precise determination of the crystallographic orientation at each analyzed point. In this work, EBSD analysis was specifically conducted on sample heat treated in air at 1300 °C and HIPped at same temperature. This analysis

was carried out to evaluate variations in grain size and morphology and assess the potential presence of prior particle boundaries (PPBs). All specimens were carefully reprepared according to the methodology detailed in Section 2.1.2 to ensure optimal surface quality for EBSD analysis, providing valuable insights into the relationship between processing conditions and the resulting microstructure.

2.4 Grain size assesment

For the evaluation of grain size, different steps were followed. After different chemical etching an optical microscopy investigation was carried out. Indeed, six images were taken for each sample, three along XY plane and the other three along XZ, at 200x magnification. FIJI-ImageJ software was used for the analysis. At the end, the average grain size was calculated following the rules of ASTM E112-13 (2021) [49].

The procedure can be divided into the steps shown below:

- Three main lines were sketched in the image, and their relative lengths were calculated.
- The grain count was determined through the linear intercept method by analyzing intersections between grain boundaries and reference lines. A full grain count (1.0) was recorded when the test line crossed two distinct boundaries of a single grain, while intersections with only one boundary were counted as half a grain (0.5). For triple junctions where multiple grains converge, each participating grain received a proportional count of one-third (0.33) to maintain geometric accuracy.
- The grain size value was calculated by dividing the length of the lines by the total number of grains counted along its path. Then, this value is compared to those in the table provided by the standard, in the mean intercept's column. Intermediate values were obtained via a linear interpolation among the values contained in table 4 of ASTM E112.
- The mean intercept was used to calculate the aspect ratio.

Figure 2.7 shows the three lines used for the identification of grains dimension by using FIJI-ImageJ software.

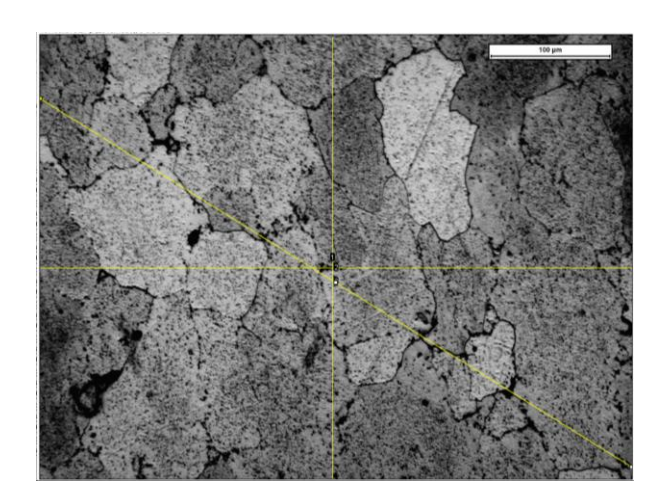


Figure 2.7. Three main lines (in yellow) for grain size analysis using FIJI-ImageJ.

2.5 Porosity analysis

For the evaluation of porosity FIJI(ImageJ) software was used. Non-etched cross-sectional samples are analyzed by light optical microscopy obtaining images with a magnification of 50x. A total of ten images were captured, five for each cross-sectional plane (XZ and XY). The sampling pattern is illustrated in *Figure 2.8*, which displays the two cross-sectional geometries along with the five designated imaging areas (labeled 1 through 5) on each plane. In light microscopy images, dense microstructures appear bright because their polished surfaces reflect light strongly. Defects, on the other hand, show up as dark regions due to surface irregularities that scatter light and reduce reflection. This contrast between the dense microstructure and defects allows for their separation. The process is automated using the open-source software FIJI for identifying defects such as spherical pores, lack of fusion, and cracks. The aspect ratio is calculated by dividing the major axis by the minor axis of the smallest ellipse that encloses the defect. This ratio helps assess defect morphology: a value of 1 means the flaw is perfectly round, while higher values indicate more irregular shapes. In addition, for analyzing defect morphology Feret diameter is used, which represents the smallest radius of a sphere that can fully contain the defect. This measurement provides additional insight into the size and shape of the flaws detected by the software.

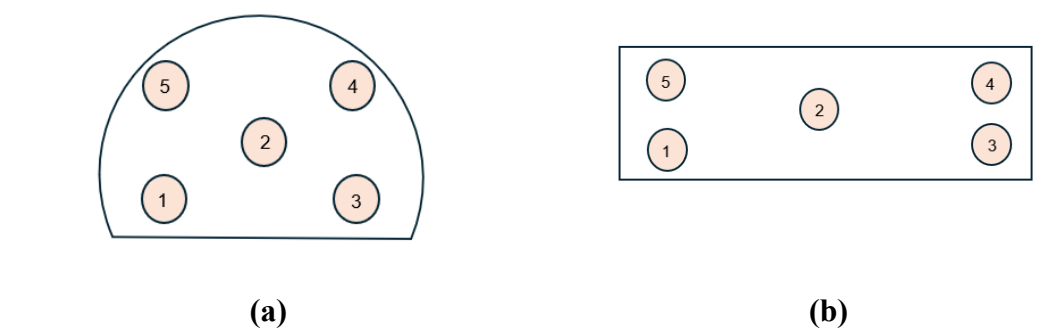


Figure 2.8. Cross-sectional geometries along with the five designated imaging areas on (a) XY and (b)XZ planes.

2.6 Differential scanning calorimetry (DSC)

The primary objective of a differential scanning calorimetry (DSC) investigation is to characterize the thermal behavior of the material system through precise measurement of heat flow variations across a defined temperature range. This thermoanalytical technique enables quantitative analysis of phase transformations by detecting endothermic and exothermic events, with the heat capacity serving as a critical parameter for identifying transition temperatures and associated enthalpic changes. With this analysis some important information of material can be obtained, such as the solidus temperature and the incipient melting temperature region. These data are fundamental to optimize the hot isostatic pressing parameters as effectively as possible. DSC was employed to characterize the thermal behavior of both as built and 1300°C air heat-treated specimens using a Setaram DSC/TGA instrument (Figure 2.9 a)). Precisely weighed samples (126 mg for the heat-treated sample and 73 mg for the HIPped sample) were loaded into alumina crucibles (100 µL capacity) alongside an Al₂O₃ reference crucible (Figure 2.9 b)). The thermal analysis protocol comprised multiple standardized stages: following an initial stabilization period at 50°C, the samples underwent controlled heating from 50°C to 1400°C at a constant rate of 15°C/min under an argon atmosphere (50 mL/min flow

rate). Subsequent cooling to ambient temperature was performed at an identical cooling rate to complete the thermal cycle. This systematic approach enabled comprehensive evaluation of phase transformations, thermal stability, and enthalpic changes across the investigated temperature range.

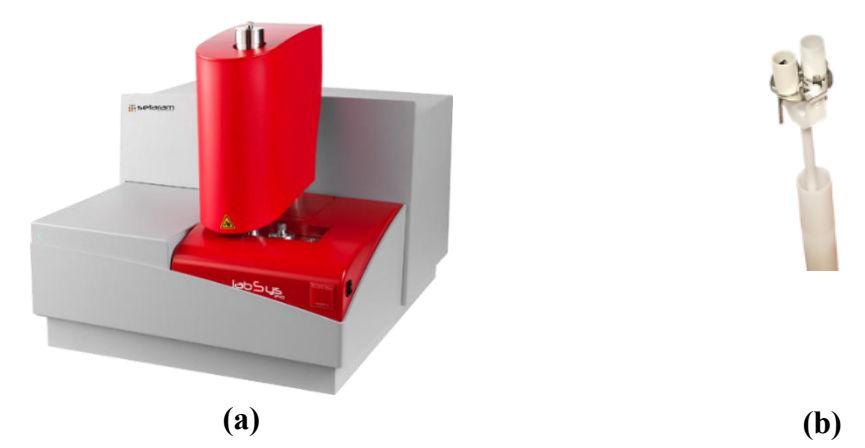


Figure 2.9. (a) Setaram LabSys Evo DSC [50] and (b)Al₂O₃ reference crucible and sample positioning.

2.7 Air-furnace Heat Treatment

In this work seven tests were conducted in a static air furnace at temperatures ranging from 1250°C to 1300°C, with an operational duration of 3 hours, followed by cooling in static air inside an alumina crucible with an estimated cooling rate of 120°C/min. These heat treatments allow to establish the temperatures at which liquid-phase zones begin to form. Six samples are obtained, respectively at 1250°C, 1260°C, 1270°C, 1280°C, 1290°C, 1300°C. The seventh one is the result of the solubilization temperature test of IN939. This standard test is conducted at 1160 °C for 4 hours with subsequent air cooling.

All the different tests conducted in this work are reported on the table below.

Sample	Temperature [°C]	Time [hours]
1	1160	4
2	1250	3
3	1260	3
4	1270	3
5	1280	3
6	1290	3
7	1300	3

Table 2.1. Standard and not standard heat treatments.

2.8 HIP (Hot Isostatic pressing)

The Hot Isostatic Pressing (HIP) system employed is the QIH 15L unit (Quintus Technologies) shown in *Figure 2.11*. It is composed of a molybdenum-lined cylindrical chamber designed for Uniform Rapid Cooling (URC) enabling the furnace to achieve maximum operational conditions of 1500°C and 228 MPa, while also supporting rapid cooling upon completion of the high-temperature dwell phase. The system is integrated with a standard argon (Ar) gas supply line, and final pressure levels are attained via a hydraulic piston-driven compressor.

The parameters setting is based on a DOE of a previous thesis "The influence of Hot Isostatic Pressing performed above solidus temperature of LPBFed Inconel 939 for microstructural improvement" [51]. This study evaluated the impact of three parameters (time, temperature and pressure) on the maximum crystal grain size after HIP treatment. By applying the "larger is better" optimization approach it maximized grain growth. So, the pressure is set at 125MPa, the least effect, time, that has the greatest impact on grain growth, is set at 180 minutes to compare the results with those of the air heat treatments, while the temperatures investigated are 1260°C,1280°C and 1300°C (*Table 2.2*).

HIP process has a crucial role inside this thesis work, since this technique allows the material to densify but also leads to some useful results that will be exposed in the next chapter.

Sample	Temperature [°C]	Pressure [MPa]	Time [min]
1	1260	125	180
2	1280	125	180
3	1300	125	180

Table 2.2. Summary of HIP parameter settings.



Figure 2.11. Quintus DSC, QIH 15L unit [52]

2.9 Nano indentation test

Nanoindentation is a technique used to measure the mechanical properties of a material at the nanoscale. A very small, precisely shaped tip (an indenter) is pressed into the surface of the sample while continuously monitoring the applied force and the depth of penetration. From this data, key properties like hardness can be calculated. In this study, the nickel-based superalloy IN939 was subjected to two distinct post-processing heat treatments at the same temperature,1300°C: conventional furnace treatment in air (Sample A) and hot isostatic pressing (Sample H). The objective was to evaluate the effect of these treatments on the local mechanical response of the alloy, with a particular focus on hardness distribution. The indenter used is Hysitron Tl 980 model. Nanoindentation experiments were performed on both samples using a constant load of 10 milliNewtons (mN), which was applied for a duration of 10 seconds. The tests were arranged in a grid pattern measuring 13 by 13 indentations, with a spacing of 5 micrometers (µm) between the center of each indentation site. This information is crucial for ensuring the tests are reproducible and for understanding the spatial distribution of the measured mechanical properties on the sample's surface. The spatial distribution of hardness was subsequently visualized through contour maps generated by triangulated interpolation, with a shared color scale spanning the full measured range of approximately 4.7–27 GPa. Power-law normalization was applied to enhance contrast in the low to mid hardness range, thereby preserving visibility of subtle variations while still representing extreme values. A schematic representation of nano indenter instrument is reported in *Figure 2.12*.

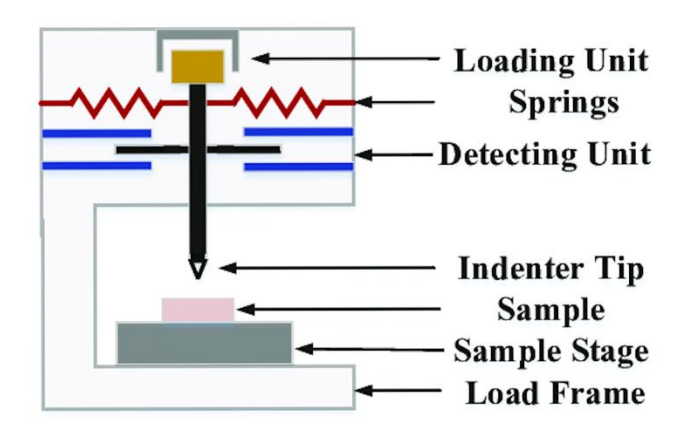


Figure 2.12. Schematic diagram of a nanoindenter instrument [55].

2.10 Minitab software

Minitab is a comprehensive statistical software application designed to facilitate data analysis, advanced statistical modeling, and continuous process improvement. It enables users to perform advanced statistical analyses, such as regression, hypothesis testing, and ANOVA, and to visualize their data through an integrated set of graphical tools.

CHAPTER 3

Results

This chapter presents a detailed analysis of the microstructural characteristics observed in IN939 samples under both as-built and post-heat-treated conditions. The findings derived from light optical microscopy (LOM), scanning electron microscopy (SEM), and electron backscatter diffraction (EBSD) are systematically discussed, highlighting key differences in grain morphology, phase distribution, and defect formation. The influence of heat treatment on precipitates evolution, grain boundary stability is thoroughly examined, providing critical insights into the microstructure-property relationships. Additionally, comparative assessments between as built and heat-treated specimens elucidate the effects of thermal processing on microstructural refinement and mechanical performance in term of hardness.

3.1. Characterization of IN939 as built sample

The material structure presented in this section is the result of the additive manufacturing process presented in *Chapter 1*. From the metallurgical point of view, the material will experience a certain number of remelting and thermal cycling due to subsequent additional laser beam passages, with a final rapid cooling that highly affects the structure of the material. While the final microstructure of IN939 is inherently influenced by process parameters, this thesis specifically focuses on microstructural optimization through post-processing of the as-built material. By systematically evaluating heat treatment strategies, the study aims to modify grain morphology, precipitate distribution, and defect structures to enhance mechanical properties, independent of initial fabrication conditions. The approach emphasizes tailoring the as-built microstructure rather than adjusting additive manufacturing parameters, providing a pathway to improve material performance through controlled thermal processing.

In *Figure 3.1* and *3.2* some of the defects detected in the as-built condition are shown, particularly gas porosity, in the XZ and XY plane.

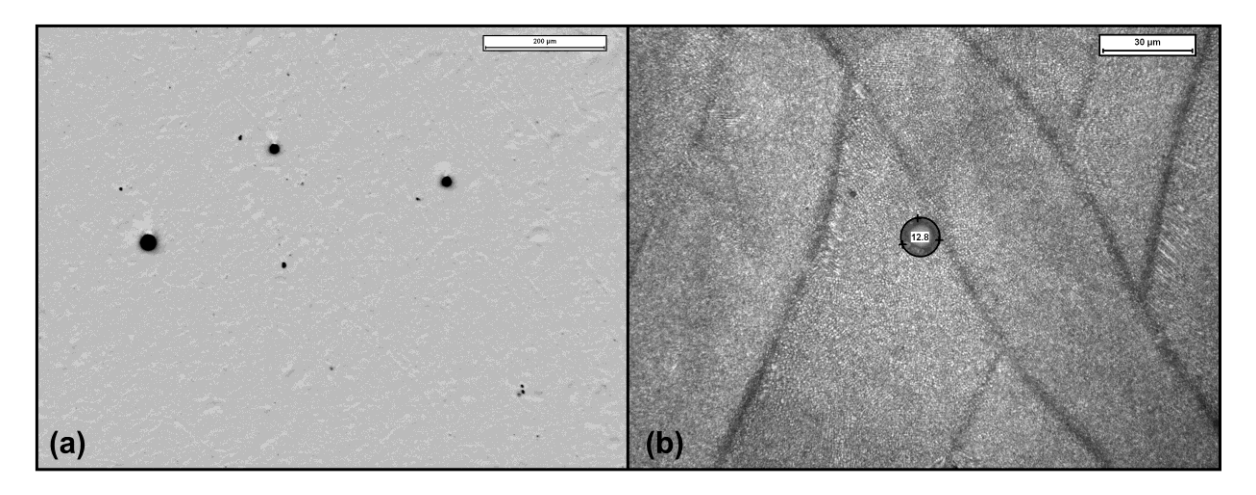


Figure 3.1. Optical Microscope image of IN939 sample showing gas porosity on XY plane at (a) 100x magnification and (b) 500x magnification.

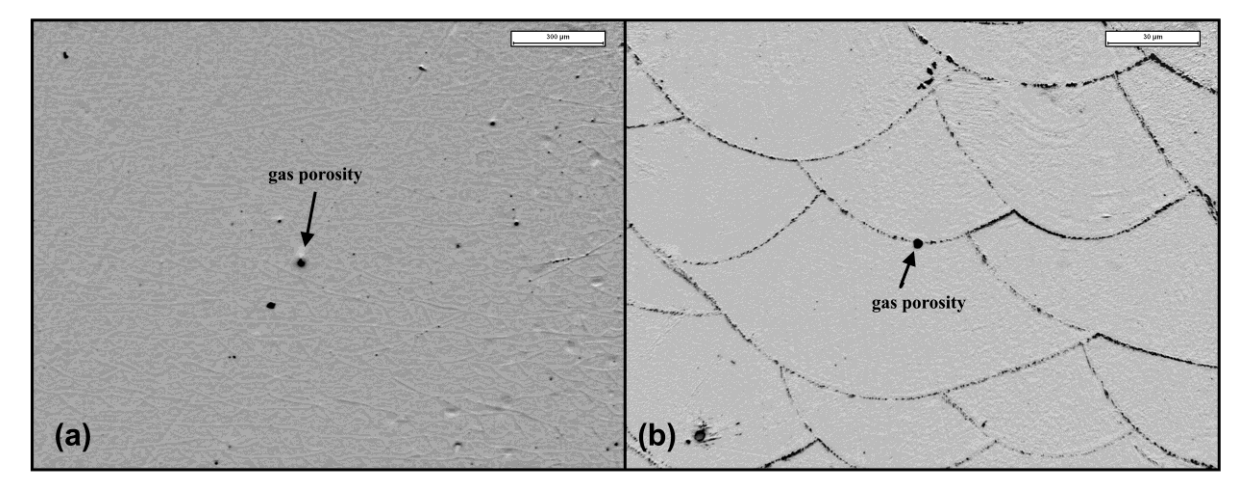


Figure 3.2. Optical Microscope image of IN939 sample showing gas porosity on XZ plane at (a) 50x magnification and (b) 500x magnification.

In the as built sample the defects that are mostly frequent are gas porosity and lack of fusion. By the analysis of this sample the concentration and morphology of these types of defects are determined. In particular, all the calculated statistics are reported in *Table 3.1*, and the aspect ratio is shown in the graphs below in *Figure 3.3*.

Table 3.1. Defect analysis summary of as-built sample.

Plane	Av. Aspect ratio	St.Dev.	Av.Defects diameter[μm]	St.Dev.	Av. %Area	St.Dev.
XY	1.16	0.20	16.54	4.51	0.036	0.017
XZ	1.24	0.16	14.14	3.20	0.020	0.009

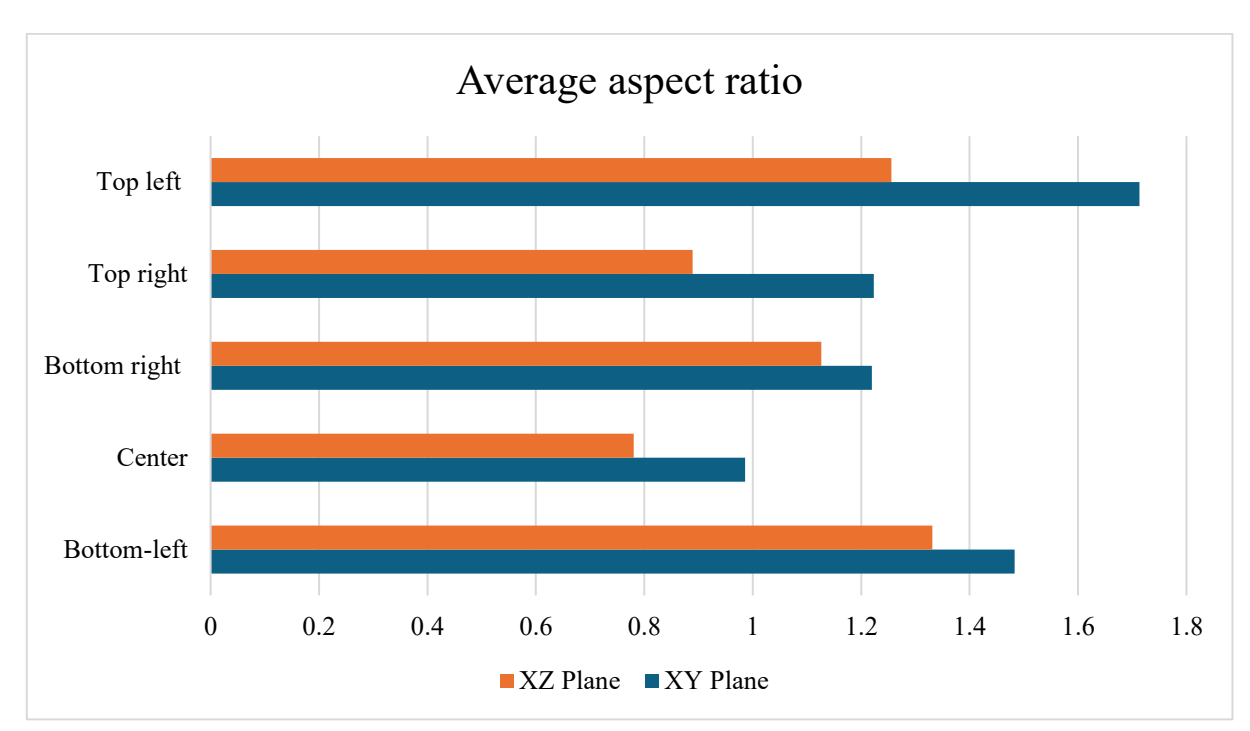


Figure 3.3. Aspect ratios in as-built sample.

The XZ-plane micrograph presented in *Figure 3.4* at different magnifications reveals well-bonded and partially overlapping melted powder layers, resulting from an optimized scanning strategy incorporating a 67° interlayer rotation of the laser track. Furthermore, the distinct "fish-scale" morphology of the melt pools, is clearly discernible [53].

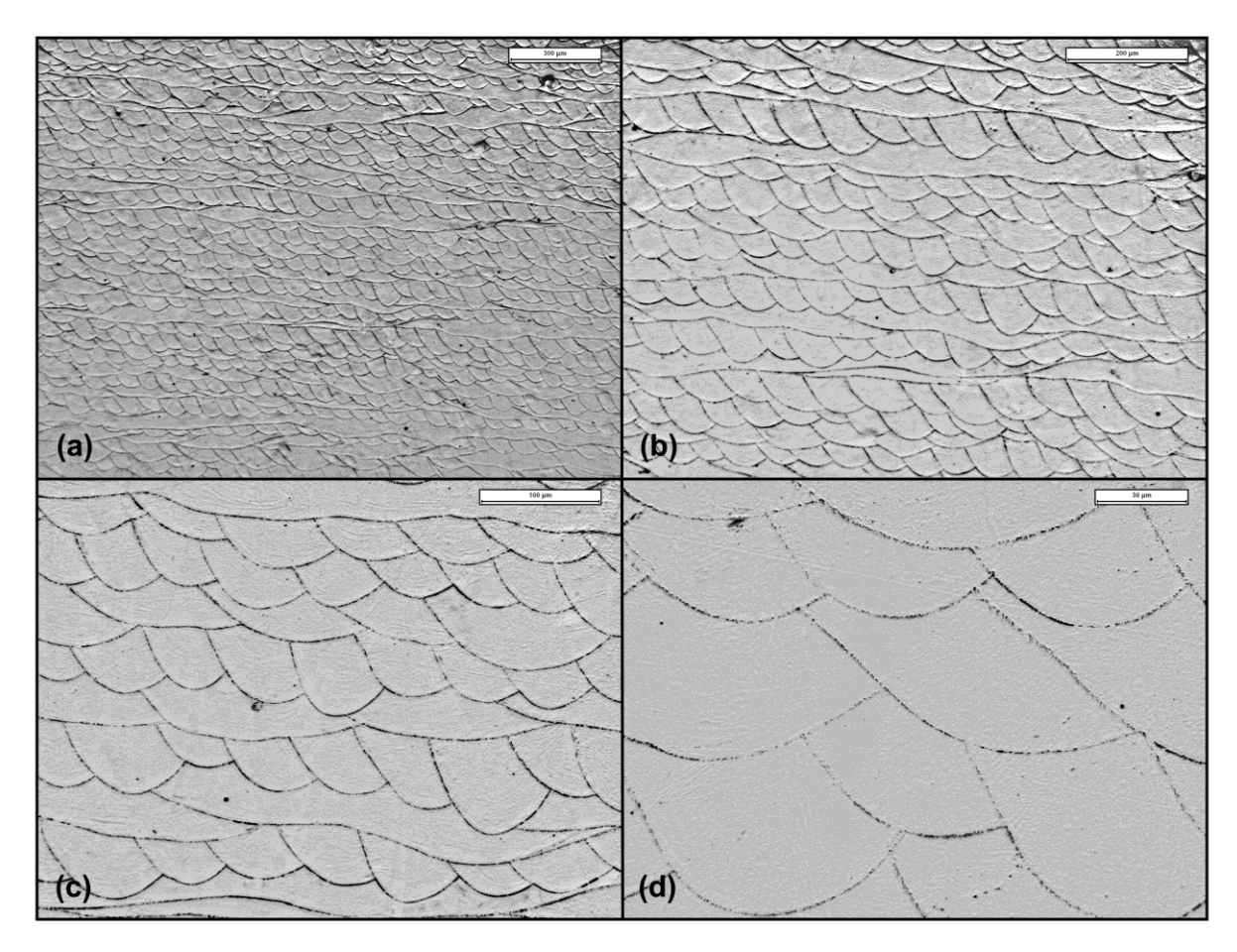


Figure 3.4. Optical Microscope image of IN939 sample showing melt pool at: (a)50x magnification, (b) 100x magnification, (c) 200x magnification, (d) 500x magnification.

.

The microstructural analysis demonstrates that grain development extends continuously across multiple layers rather than being confined to individual powder layers or melt pool boundaries. Well-defined columnar grains exhibit preferential alignment along the build direction, a direct consequence of partial remelting during successive laser passes. Higher magnification reveals distinct dendritic solidification patterns within the melt pools as shown in *Figure 3.5*. Indeed, at 500x and 1000x magnification, the micrograph clearly shows elongated dendritic structures aligned with the build axis, forming a striated pattern. This variation highlights the influence of thermal gradients on microstructural evolution during the additive manufacturing process. The continuous grain growth across layers, combined with the dendritic morphology and porosity distribution, provides critical insights into the solidification behavior and defect formation mechanisms in laser-based additive manufacturing.

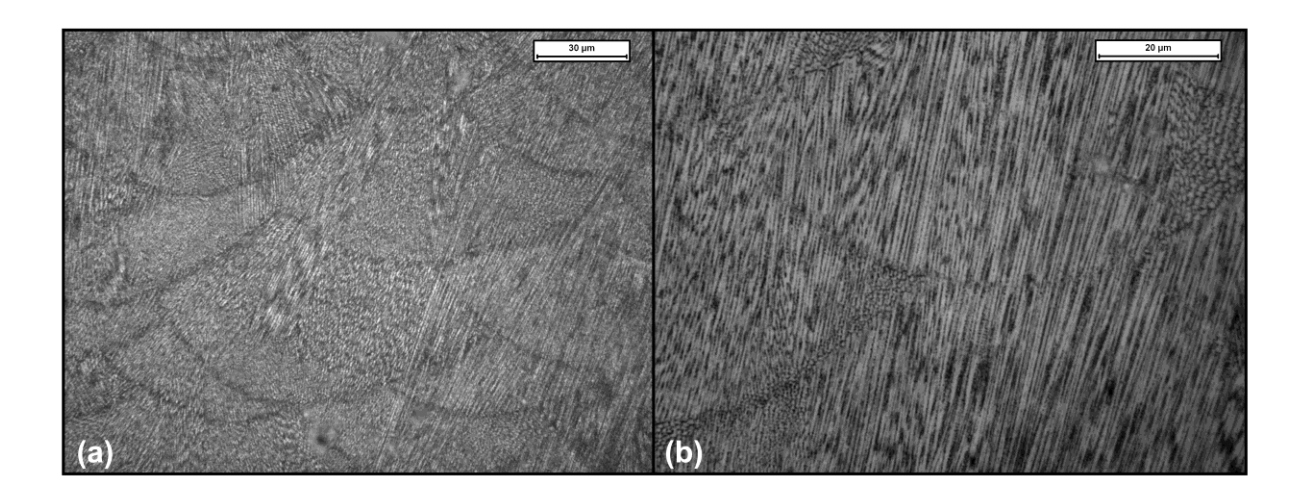


Figure 3.5. Optical Microscope image of IN939 sample showing melt pool at: (a)500x magnification, (b) 1000x magnification.

Further microstructural characterization of the sample was performed via Scanning Electron Microscopy (SEM), with particular focus on the melt pool regions. *Figure 3.6* (b), (c) and (d) display a backscattered electron (BSE) micrograph obtained at different magnification, revealing key morphological and compositional details.

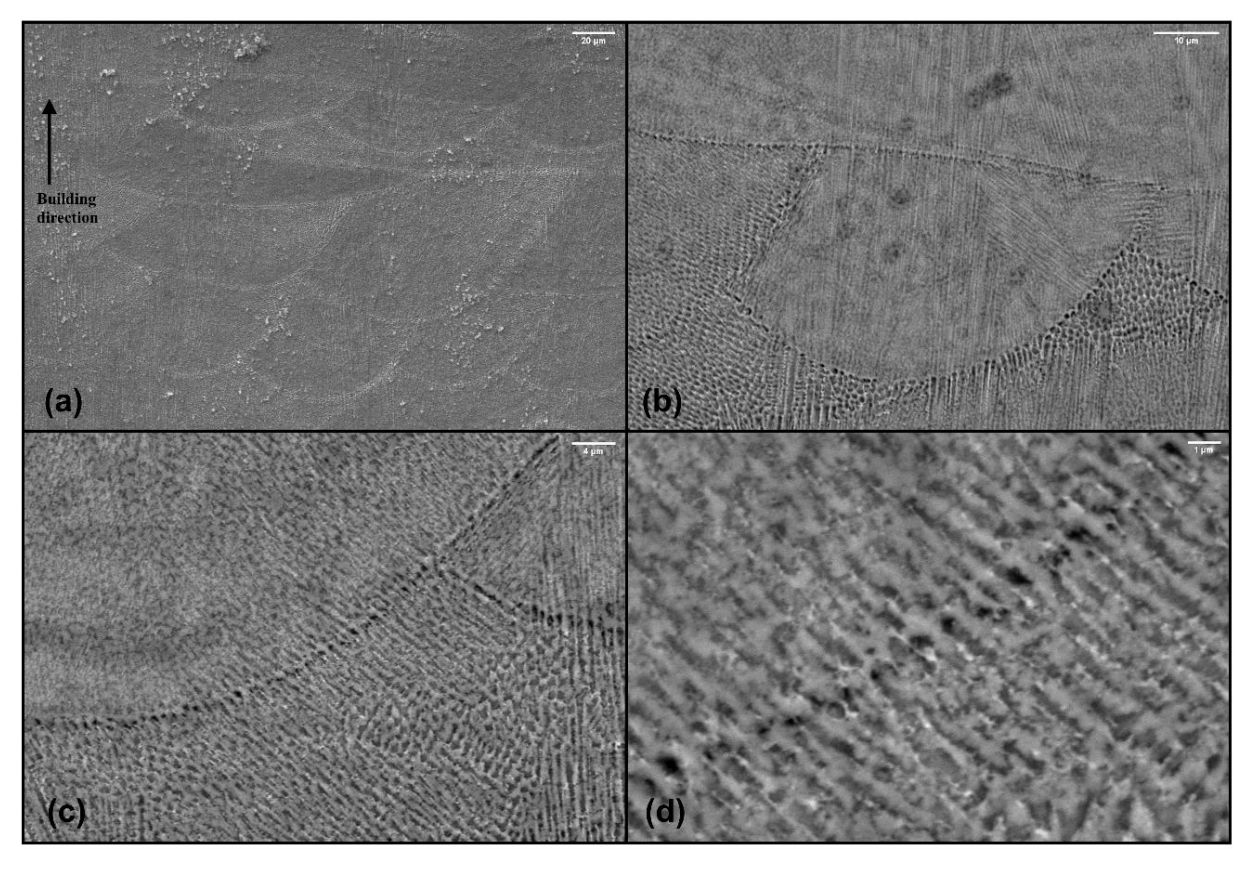


Figure 3.6. SEM image of IN939 sample at: (a)1.000x magnification with Secondary Electron, (b) 3.000x magnification with backscattered electron, (c) 5.000x magnification, (d) 16.000x magnification.

Indeed, it is possible to notice that the dendritic structure exhibits both columnar and cellular morphologies. Dendrite formation is a common phenomenon in metallic alloys and is closely linked to the solidification mechanism during the manufacturing process. As the molten metal cools, a

solidification front advances, initiating phase transformation. The process may release heat if the enthalpy of the solid phase is lower than that of the liquid, leading to interfacial instability. Under certain conditions, this instability promotes the development of a dendritic solidification structure. The term "dendritic" originates from the branching growth pattern characteristic of this solidification mode. A controlled dendritic growth is crucial during the solidification process for tailoring specific final properties of the material.

3.2 Characterization of air furnace heat treated IN939 samples

A DSC analysis was performed for the evaluation of the microstructure and the evolution of liquid formation, from room temperature to melting. To characterize the thermal behavior of IN939 the asbuilt sample was used to perform the DSC. The curves obtained from this analysis, both the heating (red) and cooling (blue), are displayed in *Figure 3.7*.

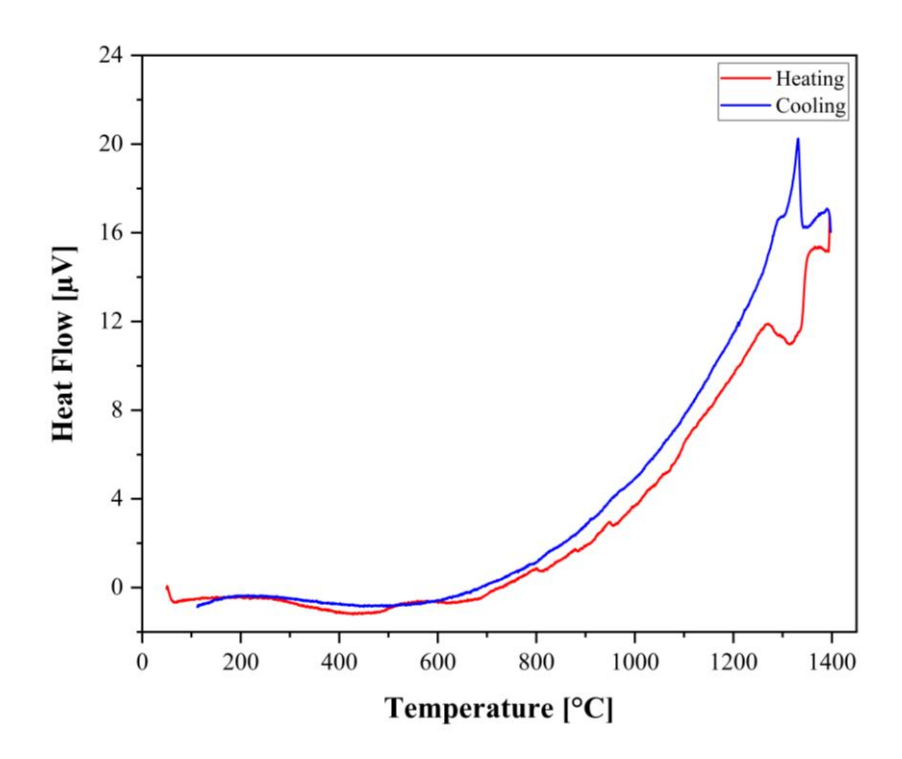


Figure 3.7. DSC cooling and heating curves for as-built sample.

During heating, the signal increases progressively up to ~1100 °C, which can be attributed to recovery phenomena and the onset of γ' coarsening and partial dissolution. A pronounced endothermic peak is detected between 1250 and 1300 °C, corresponding to the incipient melting of interdendritic regions enriched in carbides and segregated elements. This interpretation is consistent with literature, which reports a solidus for IN939 at ~1235 °C and the dissolution of carbides in the range 1275–1313 °C[19]. Upon cooling, the DSC reveals a single dominant exothermic peak in the same range, 1300–1250 °C, which is associated with the rapid re-solidification of the liquid formed during heating. Unlike some literature reports, no distinct exothermic peak is clearly resolved at lower temperatures for γ' re-precipitation in this curve, likely due to the very fine γ' already present in the as-built

microstructure. Nevertheless, γ' re-precipitation is expected to occur in this range, as confirmed in other studies on IN939. Overall, the DSC analysis identifies the critical temperature window of 1250–1300 °C as particularly significant for the as-built alloy, since the material approaches its solidus and becomes prone to localized melting. For this reason, a standard solution and non-standard heat treatments were carried out after assessing the as-built specimen as mentioned in Chapter 2. Specifically, the first standard solution treatment was conducted at a temperature of 1160°C and other six non-standard heat treatments through a working window between 1250°C and 1300°C. The main goal of these treatments is to verify at which temperature the liquid develops and understand the precipitation of the phases present in the material.

3.2.1 Characterization of standard solution heat treated IN939 samples

The solubilization heat treatment was performed at a temperature of 1160°C for a period of 4 hours, where 4h denotes the standard industrial heat treatment duration employed to achieve microstructural homogenization [45]. By analyzing the evolution of the phases and evolution of the grains in this heat treatment, the final goal is to compare it with the as-built state. In *Figure 3.8 (a)* it is possible to see that small defects are present which can be related to gas porosity and in (b) the morphology of the grains after this treatment. Comparing what is obtained after this treatment with the as built condition, it is possible to affirm that grain recrystallization did not occur, as it is shown in *Figure 3.8* (c) where in XZ plane the columnar elongated grains are still present, but the presence of melt pool is lacking.

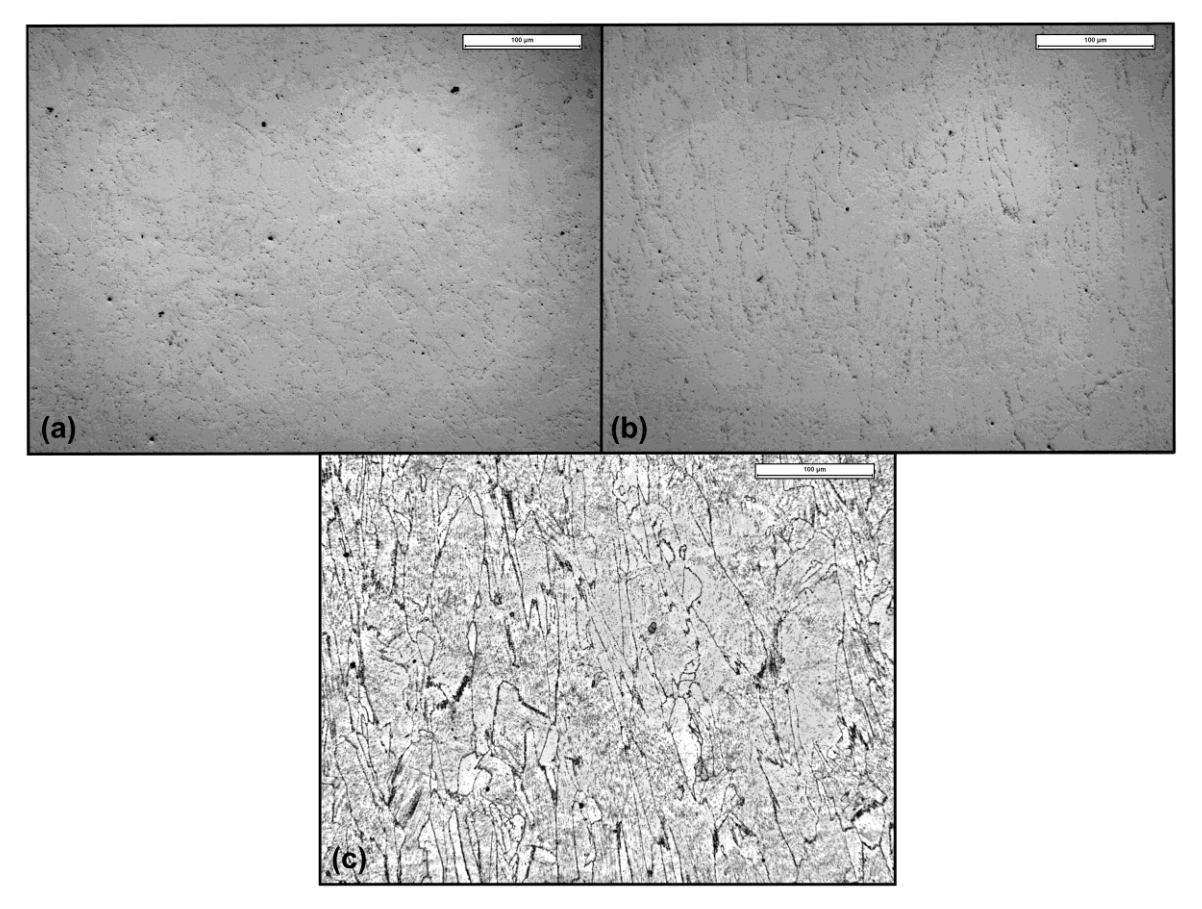


Figure 3.8. Optical Microscope image of solution heat-treated sample of IN939 at 200x magnification in (a)XY plane and (b) XZ plane (c) grain structure in XZ plane.

This is confirmed also by the values of the aspect ratio reported below.

Defects in the sample were identified through optical analysis. The aspect ratio of these defects was quantitatively evaluated using FIJI ImageJ for image processing following the methodology detailed in Chapter 2. All the results obtained are shown in *Table 3.2* and *Figure 3.9*.

Table 3.2. Defect	analysis summar	v of sample	heat treated at	1160°C.

Plane	Av. Aspect ratio	St.Dev.	Av.Defects diameter[μm]	St.Dev.	Av. %Area	St.Dev.
XY	1.41	0.27	9.77	1.85	0.014	0.007
XZ	1.74	0.32	10.41	2.29	0.018	0.013

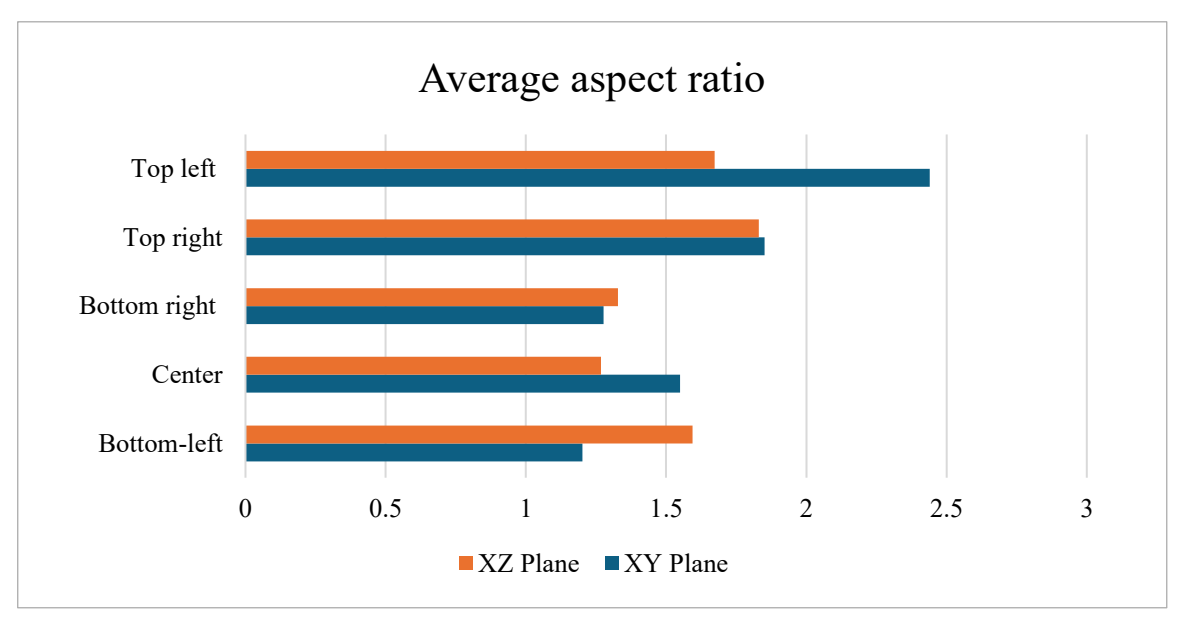


Figure 3.9. Aspect ratios in standard heat-treated sample.

Concerning the mean aspect ratios, it is possible to see that no trend is present between the areas analyzed. Only at the top can be seen a peculiar mean value.

A deeper investigation by SEM was performed to identify the carbides presence and distribution. In *Figure 3.10* two images taken both by backscattered electron at different magnification show carbide distribution in XY plane (a) and XZ plane (b). It is possible to notice that carbides, shown as bright particles(heavier), tend generally to precipitate at grain boundary.

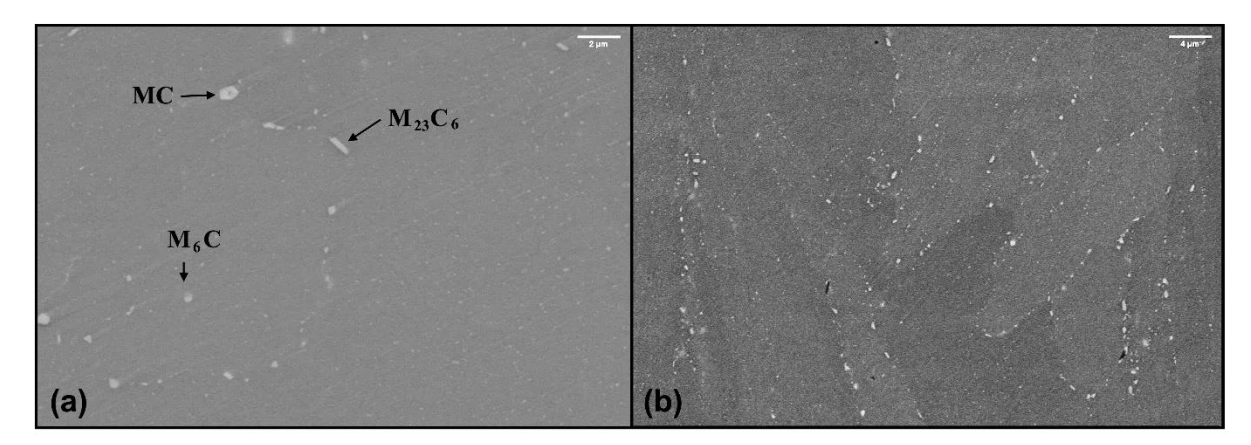


Figure 3.10. SEM image of solution heat-treated sample of IN939 taken with backscattered electron in (a)XY plane at 10.000x magnification and (b) XZ plane at 5.000x magnification.

The nature of the carbides can be classified based on literature and their morphology: MC type carbides are normally characterized by regular structures while the M₂₃C₆ carbides to the elongated ones. In *Figure 3.10 (a)* both are found along grain boundaries, this is true for M₂₃C₆ but not for MC that statistically are more frequent within the grains. In contrast, M₆C carbides are predominantly spherical and are mainly distributed within the grains. All the characteristics and effects of carbides were described in Chapter1.

With further and higher magnification, it is possible to see the areas of precipitation of carbides and their shape in particular analyzing XZ plane as reported in *Figure 3.11 (b)* and *(c)*.

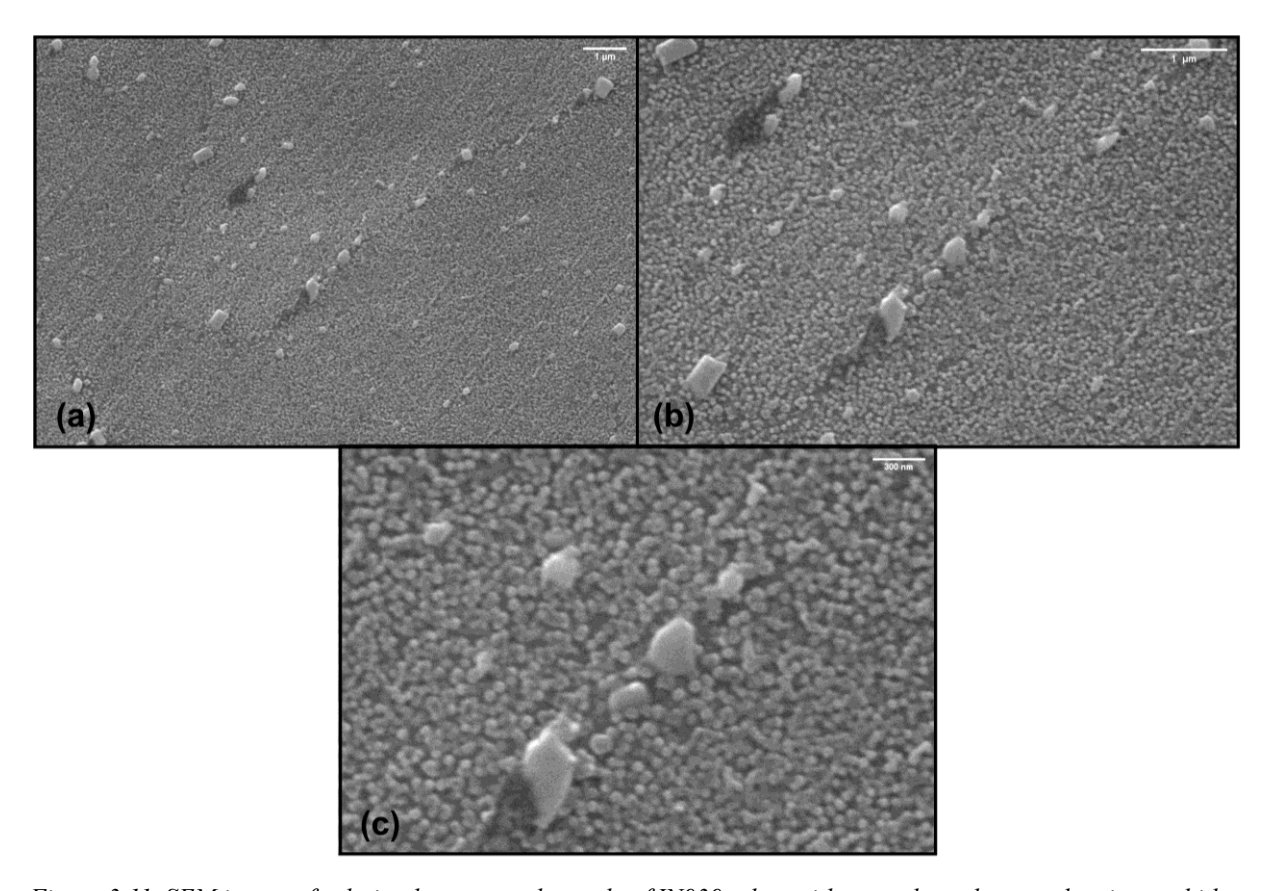


Figure 3.11. SEM image of solution heat-treated sample of IN939 taken with secondary electron showing carbides in XZ plane at (a) 20.000x magnification, (b) 40.000x magnification and c) 80.000x magnification.

EDS analysis performed on samples subjected to a 4-hour solubilization treatment confirmed the nature of the carbides. It reveals the presence of precipitates enriched in C, Ti, Nb, Ta, and W, along with a depletion of Ni, Cr, and Co. This compositional shift suggests the formation of carbides.4

3.2.2 Characterization of non-standard heat-treated specimens

In addition to the solubilization treatment, six non-standard heat treatments were carried out in a static furnace. Starting from the specimen treated at 1250°C up to 1300°C it is possible to observe how the porosity changes in size due to the incipient melting at high temperature as shown in *Figure 3.12*.

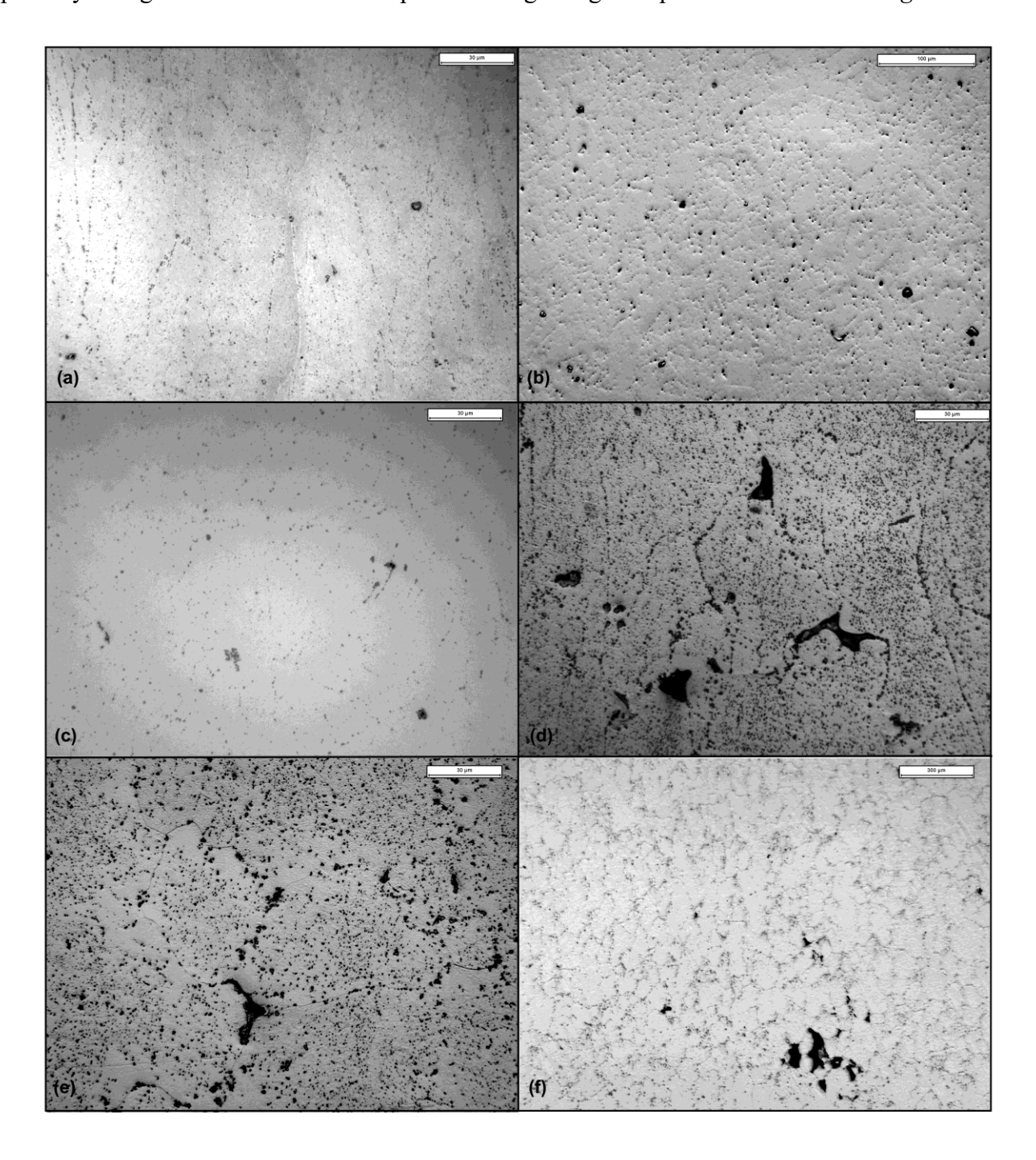


Figure 3.12. Optical microscope image of non-standard heat-treated samples (a) 1250° C, (b) 1260° C, (c) 1270° C, (d) 1280° C, (e) 1290° C and (f) 1300° C.

The defect analysis related to these specimens. All the calculated statistics relative to the six heat treatments at different temperatures are reported respectively in *Table 3.3*, *Table 3.4*, *Table 3.5*, *Table 3.6*, *Table 3.7* and *Table 3.8*, and the average aspect ratios are shown in the graph in *Figure 3.13*.

Table 3.3. Defect analysis summary of sample heat treated at 1250°C.

Plane	Av. Aspect ratio	St.Dev.	Av.Defects diameter[μm]	St.Dev.	Av. %Area	St.Dev.
XY	1.70	0.27	8.82	0.35	0.048	0.028
XZ	1.66	0.53	10.19	1.58	0.033	0.028

Table 3.4. Defect analysis summary of sample heat treated at 1260°C.

Plane	Av. Aspect ratio	St.Dev.	Av.Defects diameter[µm]	St.Dev.	Av. %Area	St.Dev.
XY	2.29	0.47	8.91	0.48	0.036	0.033
XZ	1.86	0.56	10.21	2.40	0.028	0.024

Table 3.5. Defect analysis summary of sample heat treated at 1270°C.

Plane	Av. Aspect ratio	St.Dev.	Av.Defects diameter[µm]	St.Dev.	Av. %Area	St.Dev.
XY	1.74	0.26	9.51	0.47	0.068	0.032
XZ	1.97	0.47	11.69	3.07	0.039	0.016

Table 3.6. Defect analysis summary of sample heat treated at 1280°C.

Plane	Av. Aspect ratio	St.Dev.	Av.Defects diameter[µm]	St.Dev.	Av. %Area	St.Dev.
XY	1.90	0.51	11.36	1.71	0.015	0.010
XZ	1.41	0.28	15.90	4.60	0.039	0.019

Table 3.7. Defect analysis summary of sample heat treated at 1290°C.

Plane	Av. Aspect ratio	St.Dev.	Av.Defects diameter[μm]	St.Dev.	Av. %Area	St.Dev.
XY	1.58	0.31	10.07	1.73	0.057	0.046
XZ	1.33	0.41	19.97	5.42	0.021	0.014

Table 3.8. Defect analysis summary of sample heat treated at 1300°C.

Plane	Av. Aspect ratio	St.Dev.	Av.Defects diameter[μm]	St.Dev.	Av. %Area	St.Dev.
XY	1.05	0.19	30.98	11.34	0.107	0.074
XZ	2.01	0.55	36.98	13.95	0.692	0.717

An easier evaluation can be done by seeing *Figure3.13* that reports a graphic comparison of all the samples' mean aspect ratios. It can be seen that with the increasing temperatures from 1270°C to 1280 °C there is a lowering of the mean aspect ratio of the flaws in XZ plane, such trend is inverted from 1290 to 1300 °C showing instead, a large increment. Thus, can be state that in ranges between 1290 °C and 1300 °C the presence of a plenty liquid phase produces larger porosities.

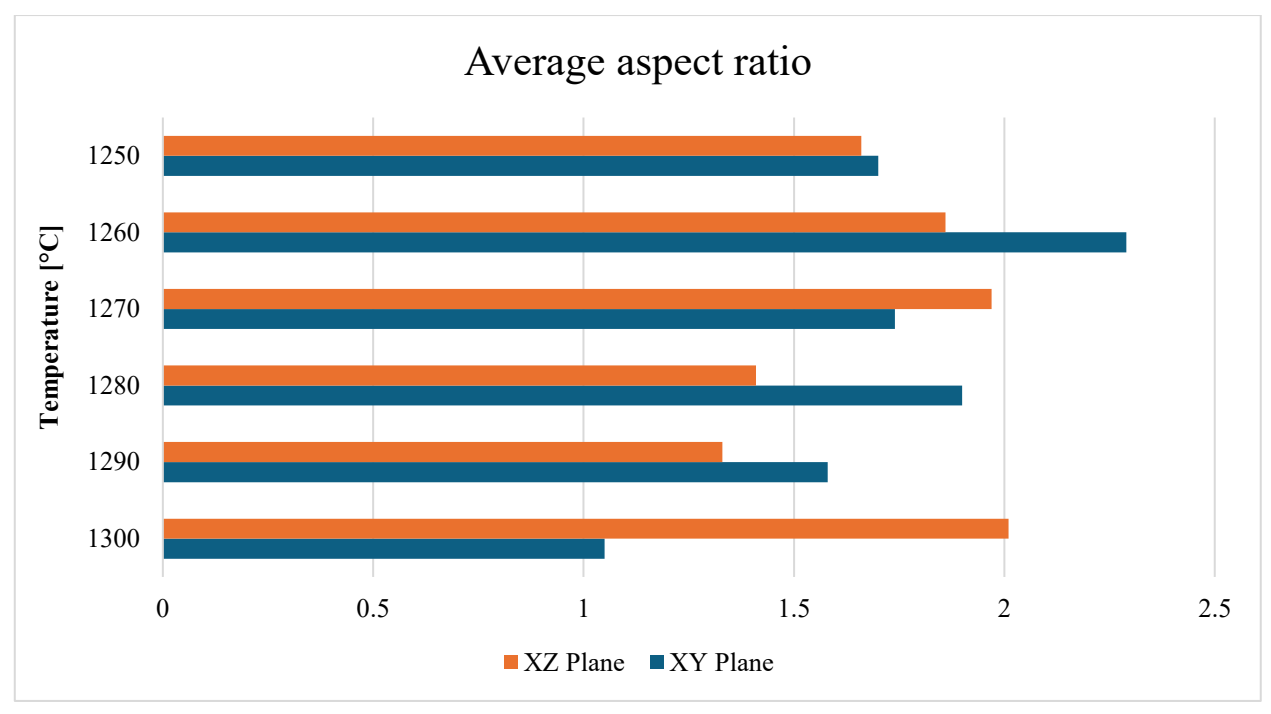
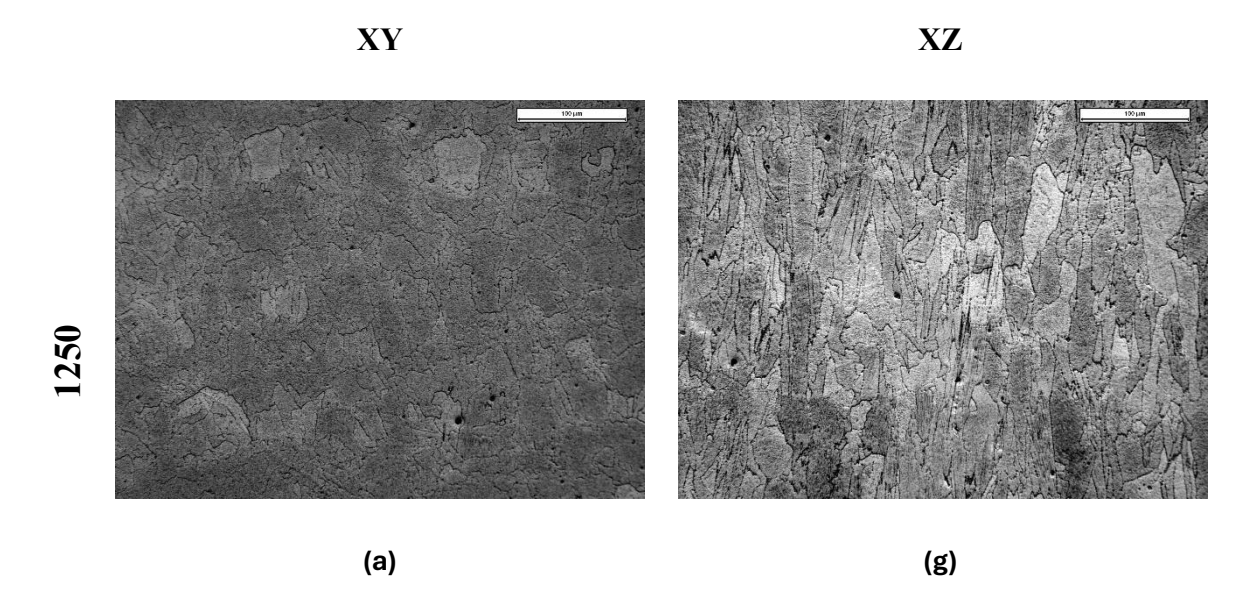
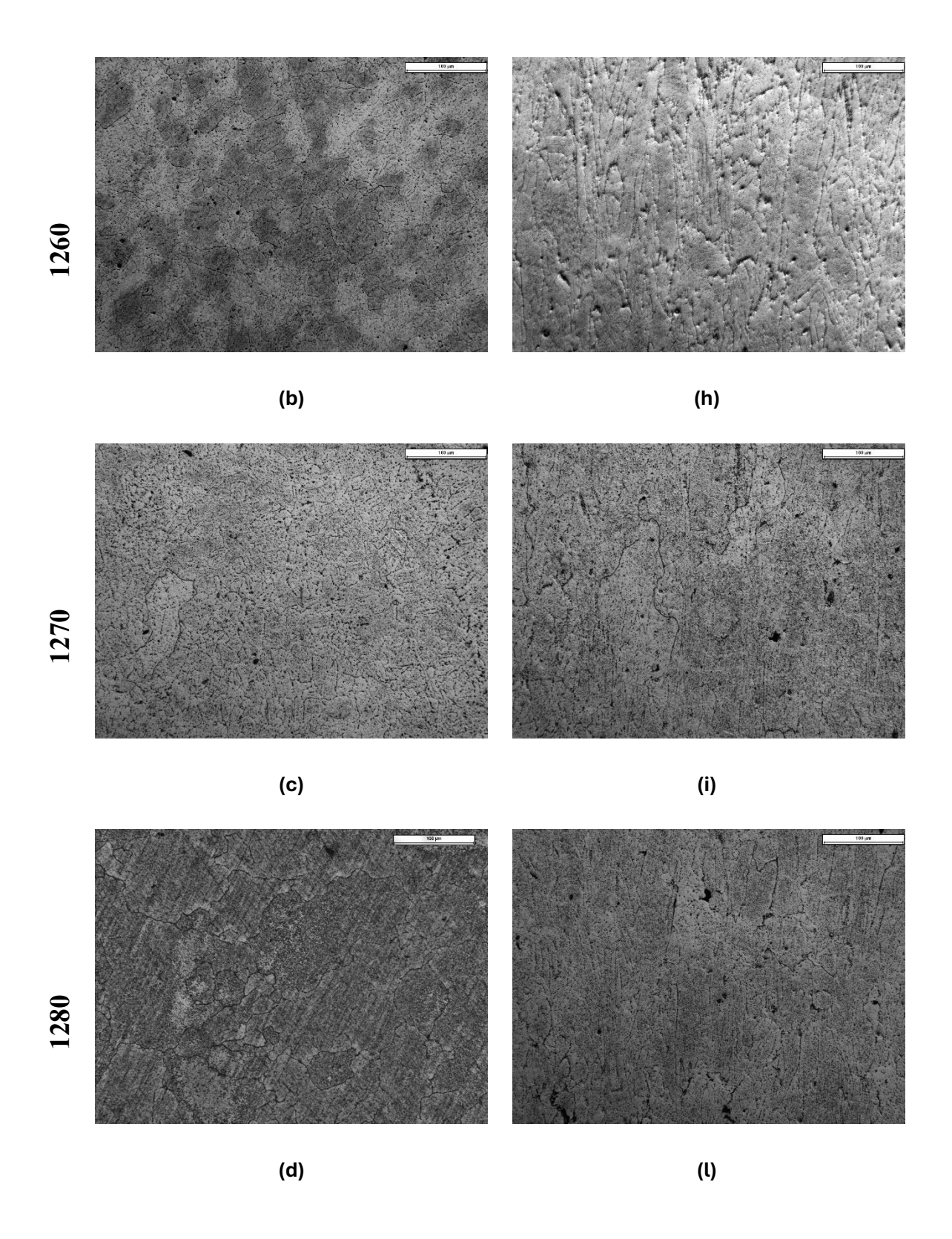


Figure 3.13. Aspect ratios in air heat-treated samples.

As concerns to the grain size evolution, *Figure 3.14* gives a general overview of how the grains have changed passing from 1250°C to 1300°C investigating both XZ and XY plane. All the images were taken with a light optical microscope at 200x magnification.





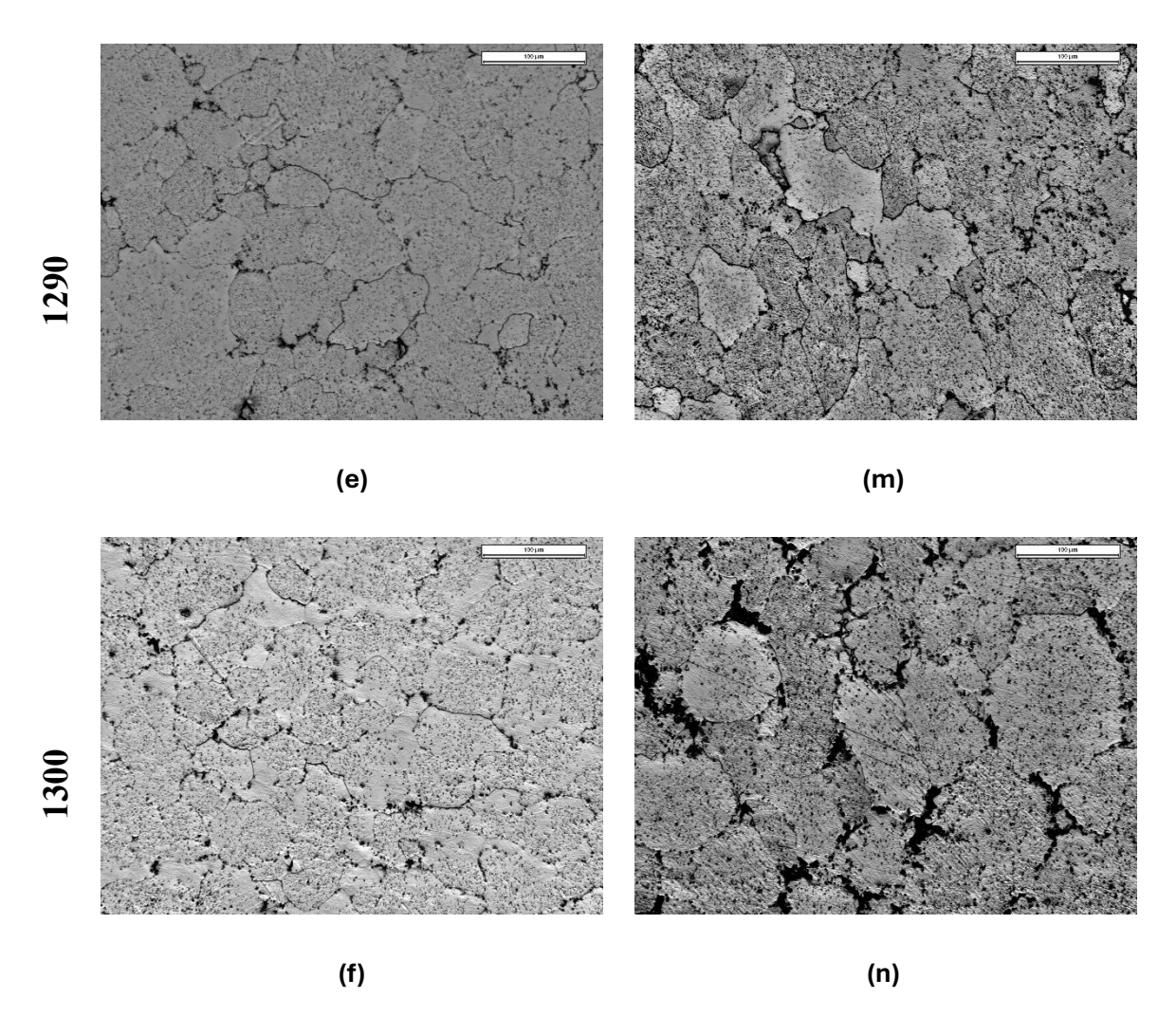


Figure 3.14. Evolution of grain microstructure of non-standard heat-treated samples IN939 in the XY (left) and XZ (right) planes at temperature of: (a, g) 1250 °C, (b, h) 1260 °C, (c, i) 1270 °C, (d, l)1280 °C, (e,m) 1290 °C, (f, n)1300 °C.

Focusing on XZ direction, qualitatively it is possible to notice that increasing the temperature the grains slowly start to increase their size but continue to maintain their columnar and elongated shape throughout the building direction until the temperature of 1280°C. Instead, from 1290°C a different situation can be observed: the grains begin to lose their previous shape and become more equiaxed (Figure m,n). Particularly in the sample at 1300°C the grains show a similar geometry in both planes XZ and XY losing definitively their oriented shape. A possible reason for this phenomenon could be related to the fact that the material undergoes only a grain growth process up to 1270°C due to the increasing of temperature. Exceeding this temperature, a recrystallization process can occur causing a progressive loss of the elongated shape typical of additive manufacturing product. At 1300 °C both XZ and XY planes show an equiaxed grain structure. Through the grain size analysis is possible to confirm this evaluation as reported in *Figure 3.15* and *Figure 3.16*.

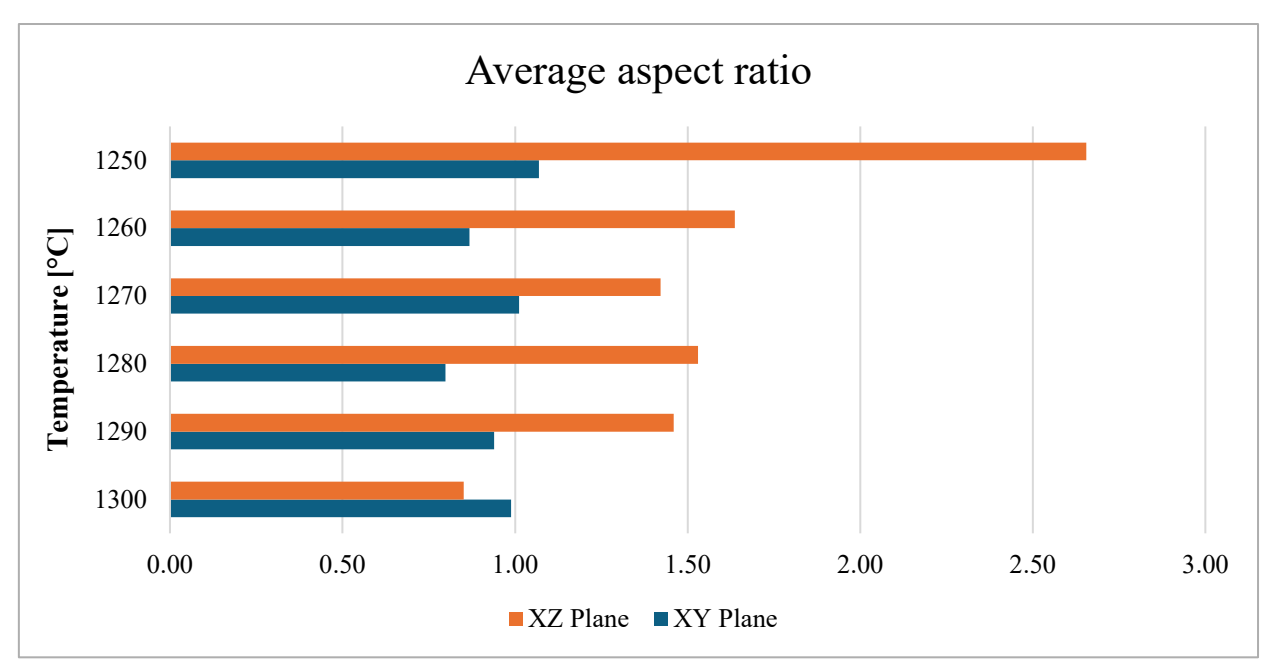


Figure 3.15. Comparison of non-standard heat-treated average aspect ratio.

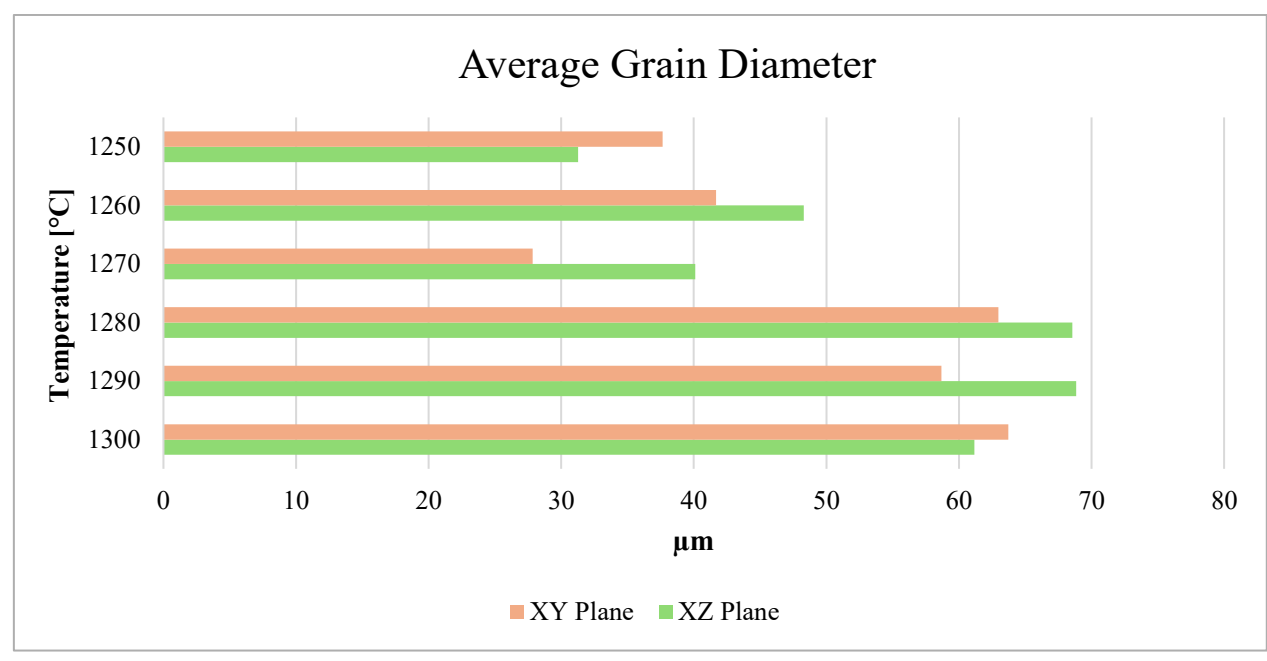


Figure 3.16. Comparison of non-standard heat-treated average grain diameters samples

To complement the quantitative grain size data, Figure 3.17 presents optical micrographs of samples heat-treated in air at 1290 °C and 1300 °C in XZ plane. The 1290 °C condition (a) shows a heterogeneous grain structure, with coarse grains coexisting alongside smaller ones, reflecting uneven growth. In contrast, the 1300 °C sample (b) exhibits a little finer but more homogeneous distribution. This observation is consistent with the modest reduction in average grain size reported at 1300 °C, confirming that incipient melting and subsequent re-solidification hinder abnormal coarsening.

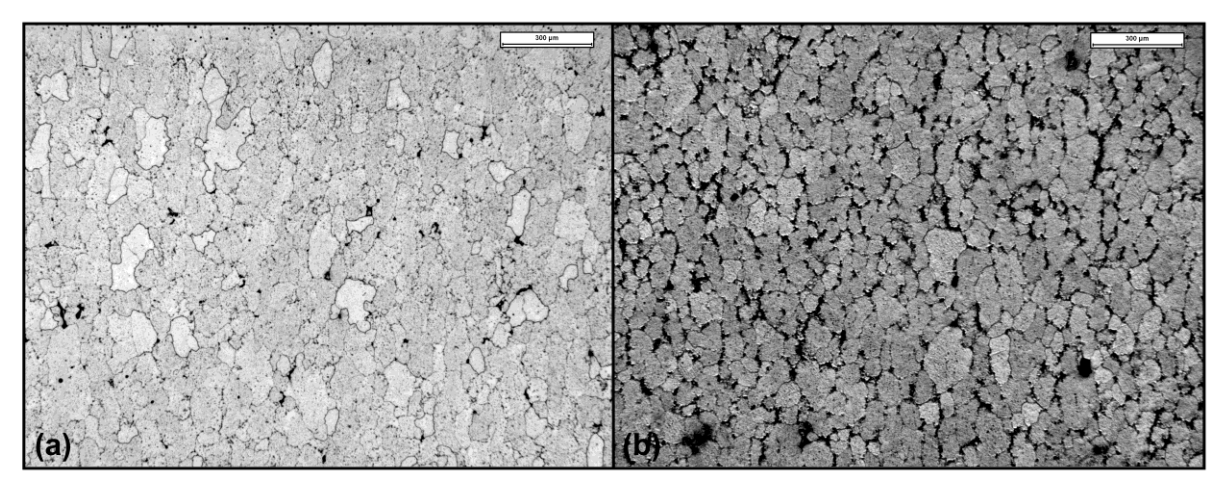


Figure 3.17. Optical microscope image of non-standard heat-treated samples in XZ plane at 50x magnification at (a) 1290°C, (b) 1300°C

As it is possible to notice in *Figure 3.16*, the sample treated at 1280°C shows bigger grain than 1290°C heat treated sample. As it is presented in a schematic representation in *Figure 3.18*, gamma prime it is not present at these temperatures, so Ti and Ta can move away (composition of gamma prime Ni₃(Al,Ti,Ta) where Ti and Ta are substitutes for aluminum) following solid diffusion mechanism. At 1280°C the presence of carbides at grain boundary (GB) starts to be consistent, the grains grow up but there is no liquid formation. The number of carbides at grain boundary increases at 1290°C, leading to a consistent pinning of the grain. In conclusion, the reason for bigger grains at 1280°C compared to 1290°C can derive from the fact that by increasing the temperature it is more effective the carbide pin effect that blocks the grains growth considering that the time of diffusion process is the same for all the treatments.

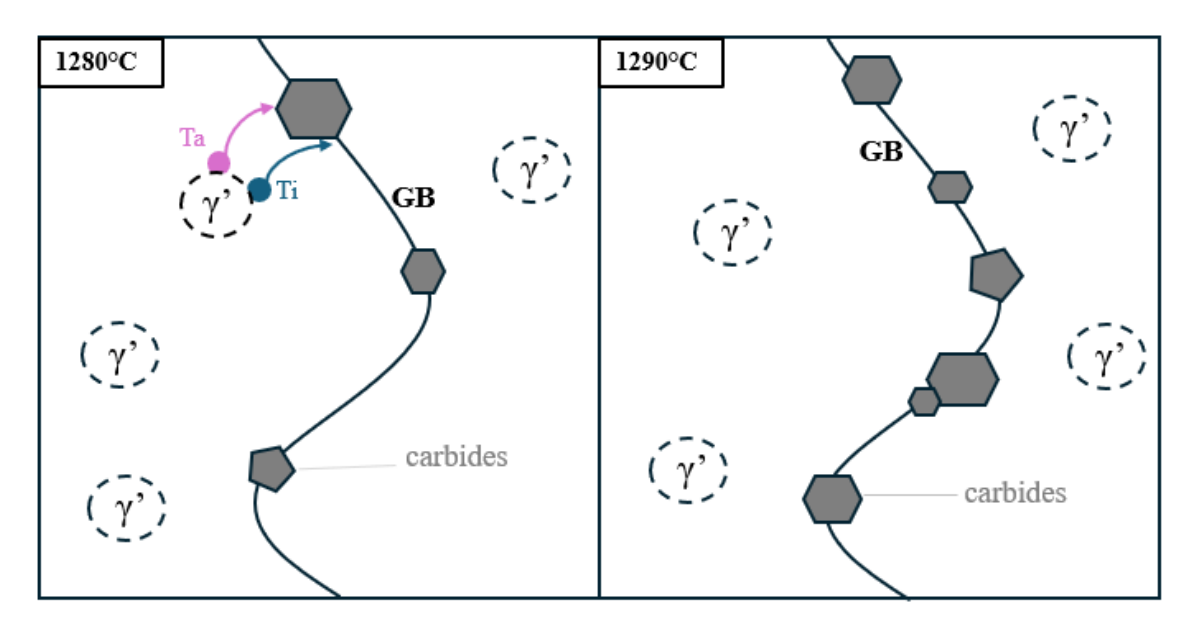


Figure 3.18. Schematic representation of solid diffusion of Ti and Ta and carbides pinning at 1280°C and 1290°C.

60

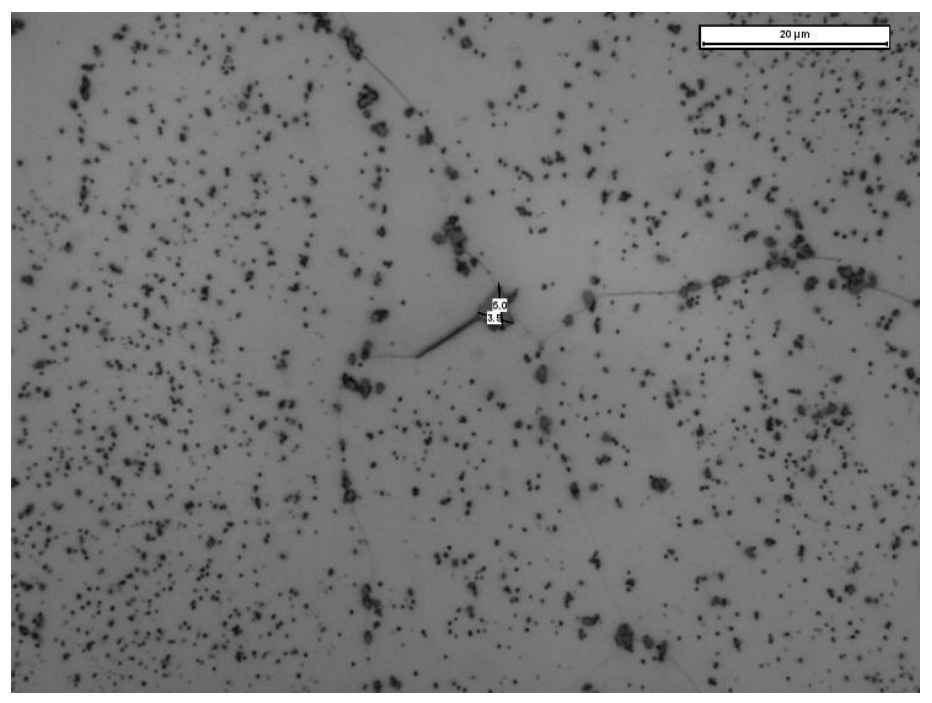


Figure 3.19. Optical Microscope image of IN939 sample heat treated at 1290°C with 1000x magnification showing carbides.

A deep investigation of sample heat treated at 1250°C was conducted. A general view of the microstructure is given in *Figure 3.20*. It is possible to appreciate the decoration of grain boundaries with particles such as carbides. These secondary phases are present in lower amounts compared to the sample heat treated at 1300°C as detailed later in this work.

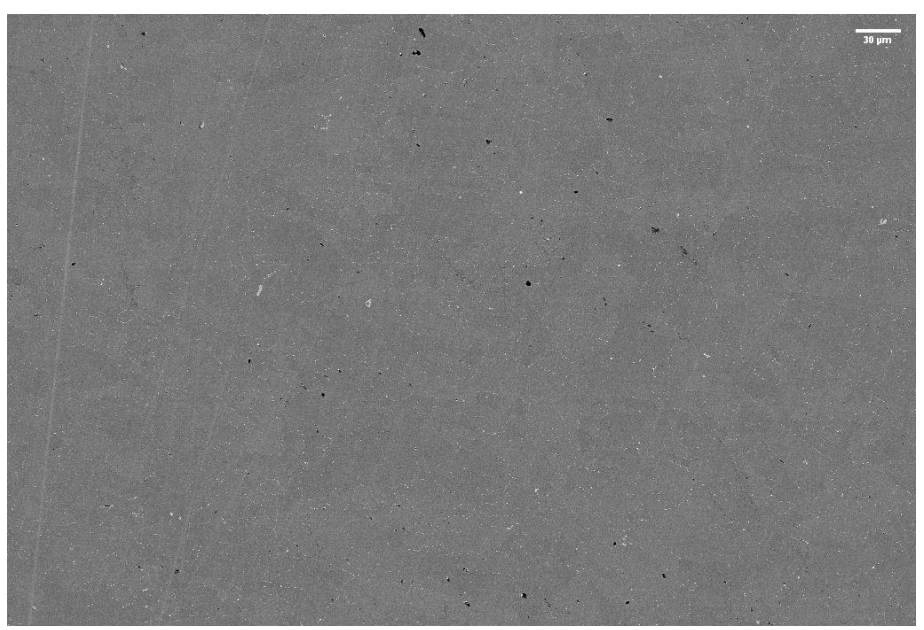


Figure 3.20. SEM image of heat-treated sample of IN939 at 1250°C taken with backscattered electron at 500x magnification.

For the sample subjected to a heat treatment at 1250 °C, microstructural analysis of XY plane confirms that carbides are present, but at this temperature no significant enrichment of these precipitates is observed (*Figure 3.21*).

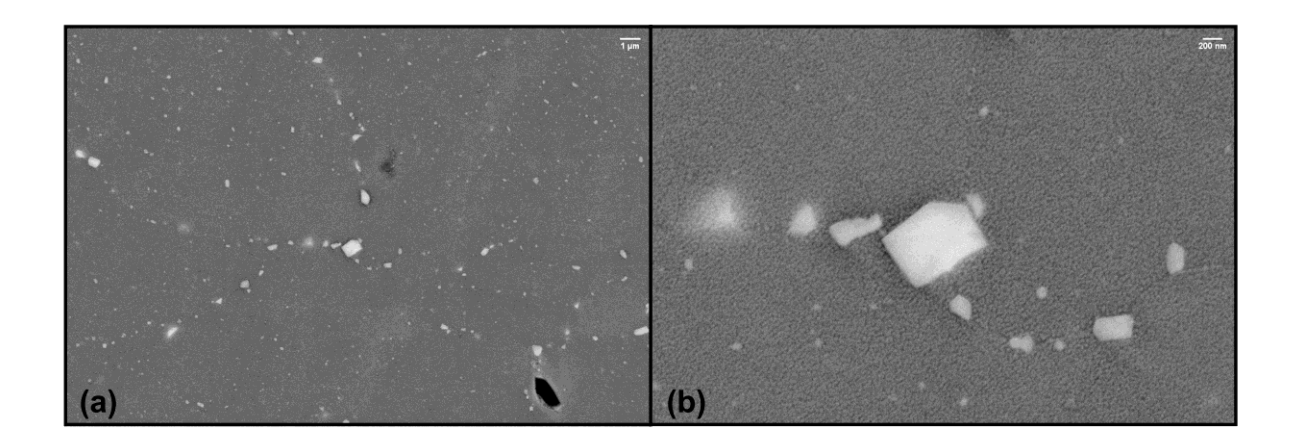
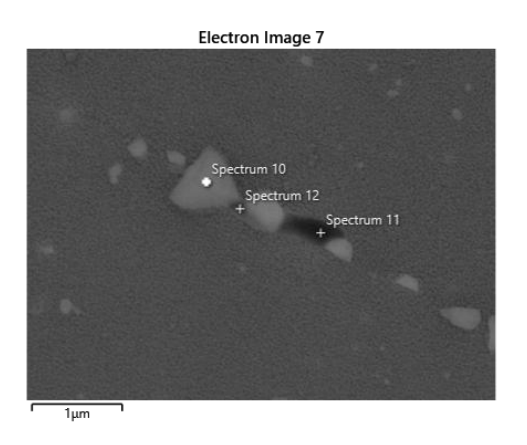
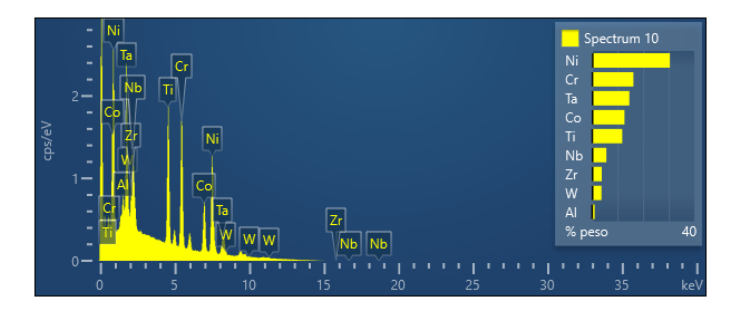


Figure 3.21. SEM image of heat-treated sample of IN939 taken with backscattered electrons in XY plane at (a) 10.000x magnification and (b) and 50.000x magnification.

An EDS analysis was carried out. The elemental spectrum presented in *Figure 3.22 (b)* indicates a significant presence of titanium and tantalum, about 11wt% and 14t%, confirming the formation of "Ti-TaC" mixed carbides. Furthermore, the results suggest that elevated temperatures promote the segregation of these specific alloying elements to the grain boundaries, which in turn enhances the stability of the carbide phases. A particular point analyzed in spectrum 12 in *Figure 3.22 (d)* shows a composition with a concentration of Cr of about 22wt% and Ti 4wt% with a high presence of Ni (46wt%) indicating a combination with carbides and matrix elements.



(a)



(b)

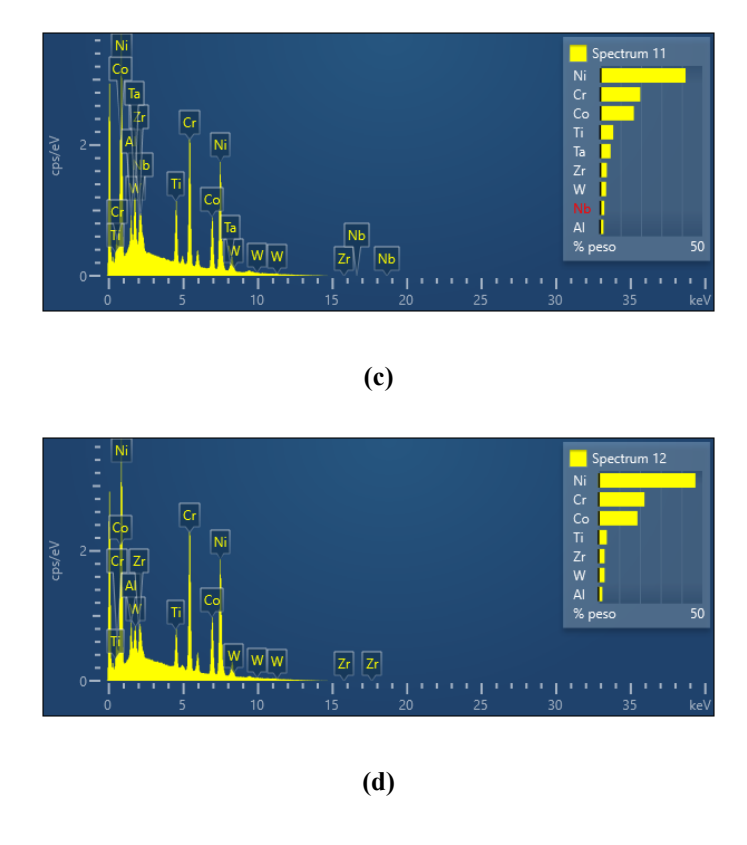
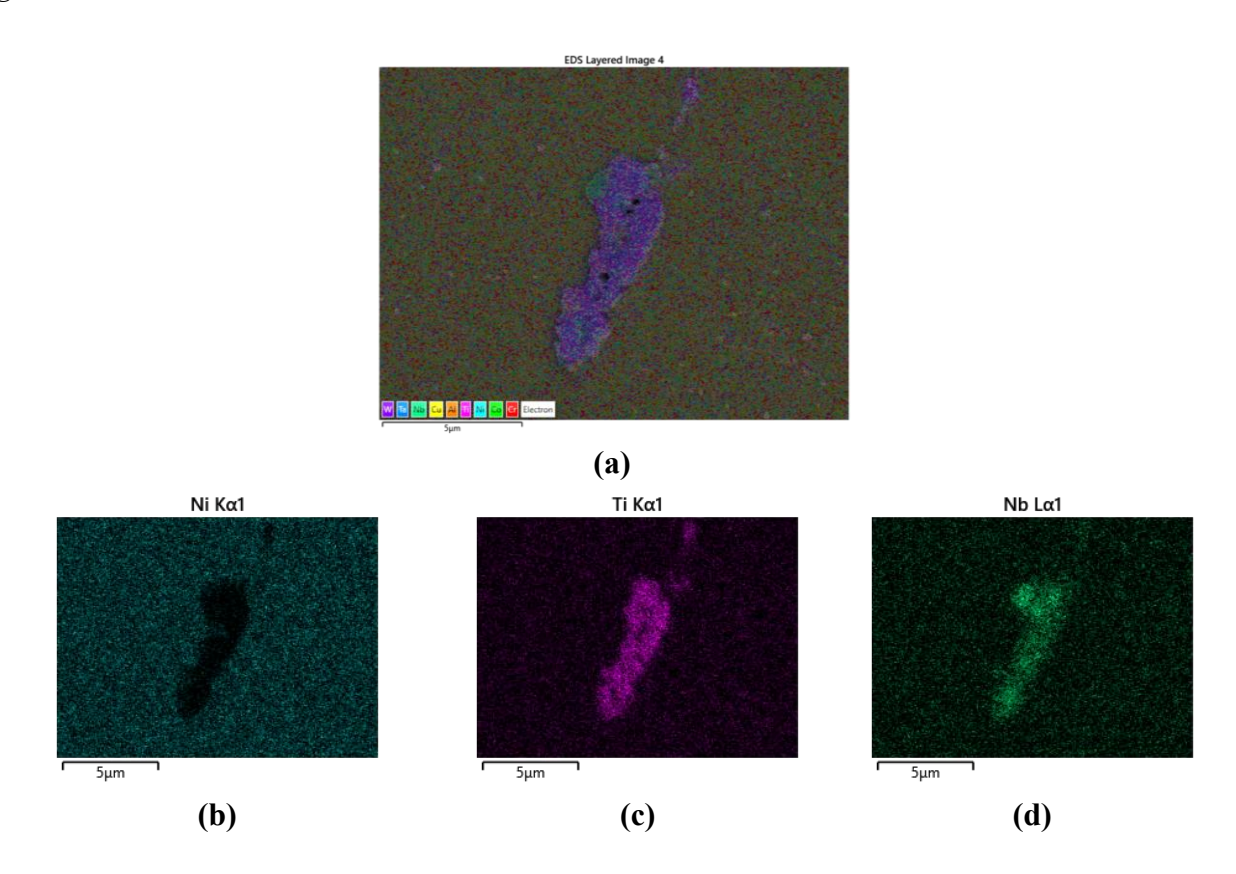


Figure 3.22. EDS analysis of heat-treated sample of IN939 at 1250°C (a) image (b), spectrum10 (c), spectrum 11 and (d) spectrum 12.

Carbides of mixed composition were found, and the investigation is reported in the map analysis in *Figure 3.23*.



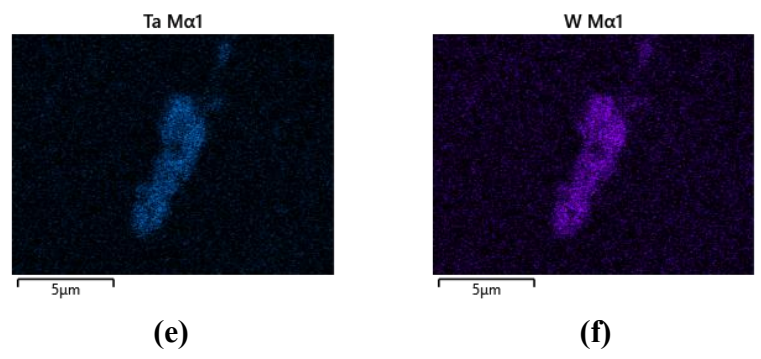


Figure 3.23. EDS map analysis on-air heat-treated sample at 1250°C showing carbides.

Analysis of the elemental distribution indicates a correlation between Ti and Ta (*Figure 3.23 (c), (e)*). In contrast, Nb (*Figure 3.23 (d)*) is predominantly concentrated within the darker phases evident in the micrograph (*Figure 3.23 (a)*).

As it concerns gamma prime (γ') evaluation, Figure presents its morphology. It can be asserted that the process is largely independent of the solution heat treatment temperature, provided it is consistently maintained above the solvus temperature. Under this condition, the governing factor is the cooling rate. Since all samples were cooled in an identical manner, with only negligible variations in few degrees per minute, the microstructure of the γ' (gamma prime) phase remains effectively unchanged. As shown in *Figure 3.24(b)*, imaging at 200.000x magnification reveals that the γ' precipitates possess a spherical shape.

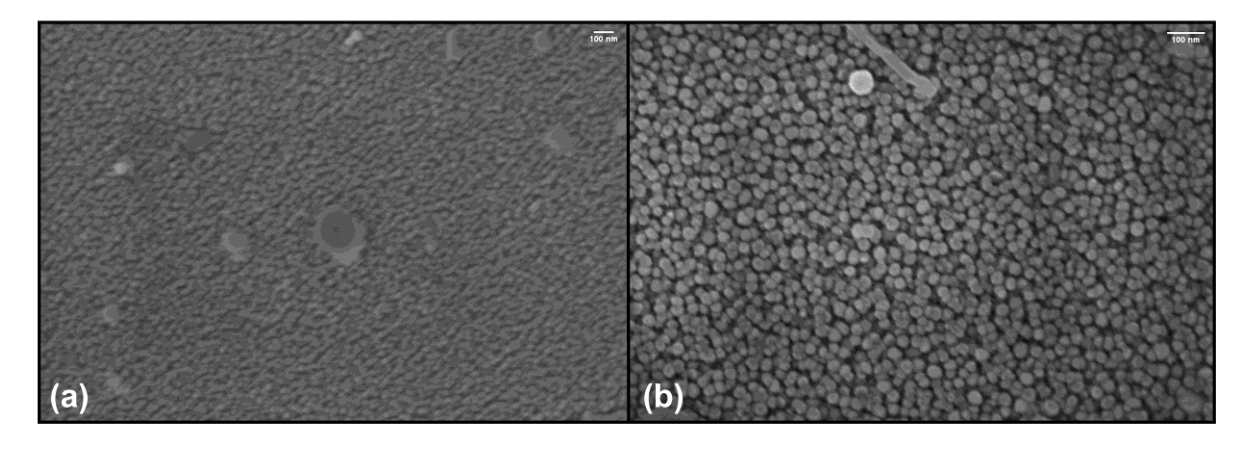


Figure 3.24. SEM image of heat-treated sample of IN939 at 1250°C taken with secondary electrons in XY plane at (a) 101.000x magnification and (b) and 200.000x magnification.

Also, XZ plane was investigated (Figure 3.25).

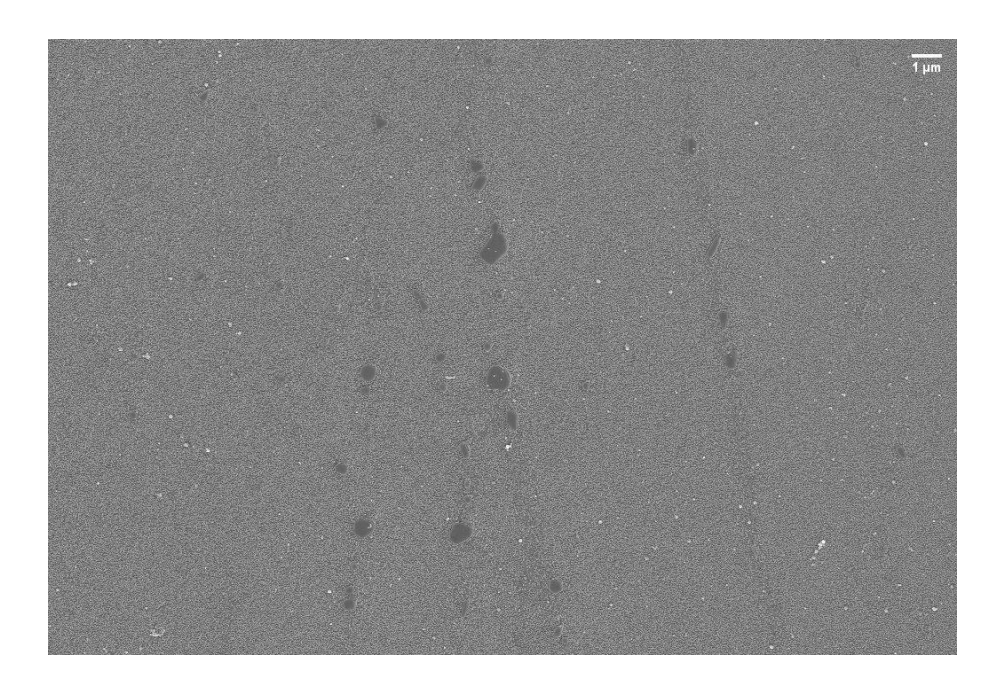


Figure 3.25. SEM image of heat-treated sample of IN939 at 1250°C taken with secondary electrons at 10.000x magnification in XZ plane.

The γ' precipitates exhibit a highly uniform size distribution. Indeed, *Figure 3.26* shows the γ' (gamma prime) precipitates distributed throughout the matrix and their morphology adjacent to the primary carbides. Unlike the sample treated at 1300 °C, which exhibites a microstructure with regions of fine and coarse γ' , the microstructure presented here is homogeneous and devoid of such spatial variations. A magnification reported in *Figure 3.26* (b) clearly illustrates this.

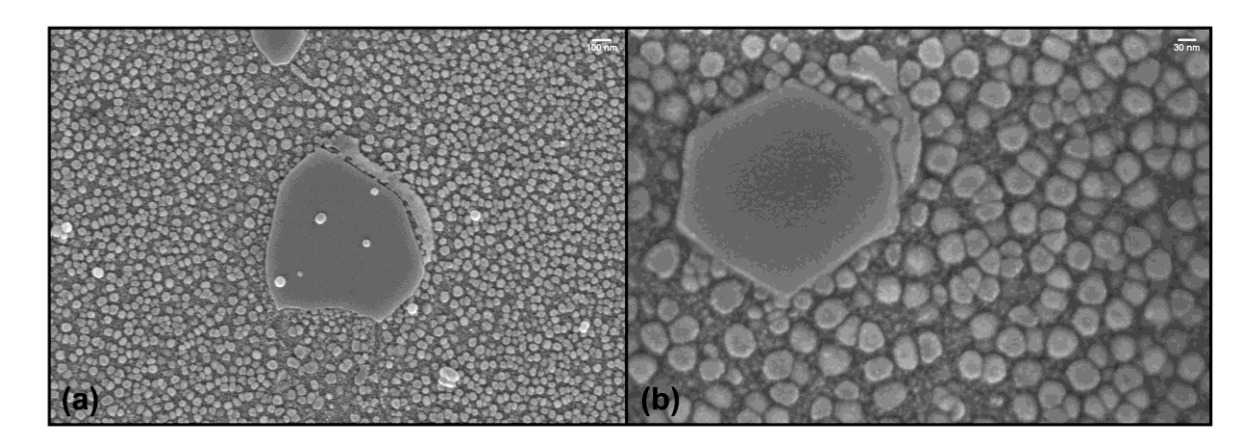


Figure 3.26. SEM image of heat-treated sample of IN939 at 1250°C taken with secondary electrons in XZ plane showing gamma prime and carbides at (a) 100.000x magnification and (b) 300.000x magnification.

As a conclusion it is possible to declare that gamma prime shows a different dimension compared to XY plane.

A deep investigation of sample heat treated at 1260°C was conducted. At this temperature the diffusion of titanium occurs, facilitating the formation of a limited population of discrete, well-defined primary MC-type carbides as it is possible to see in *Figure 3.27* in XZ (a) and XY (b) planes. It suggests the cooling rate is sufficiently rapid to suppress the precipitation of secondary phases along

grain boundaries yet controlled enough to promote a precipitation of fine, spherical γ' (gamma prime) within the γ matrix. Furthermore, this thermal profile results in a microstructure devoid of any evidence of localized melting or microfusion.

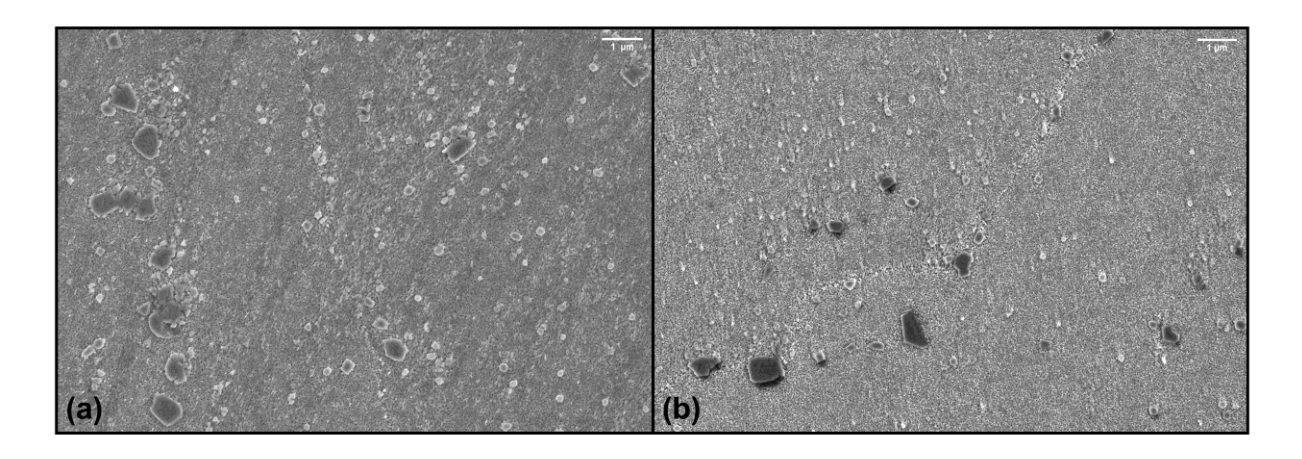


Figure 3.27. SEM image of heat-treated sample of IN939 at 1260°C taken with secondary electrons at 20.000x magnification in (a) XZ plane and (b) XY plane.

Analysis of the γ' (gamma prime) precipitates at higher magnification (*Figure 3.28*) reveals a non-uniform morphology. However, a distinct directional alignment is observable within the XZ plane (*Figure 3.28 (a)*). This alignment is interpreted as a microstructural inheritance from the original columnar grain structure of the material in this orientation.

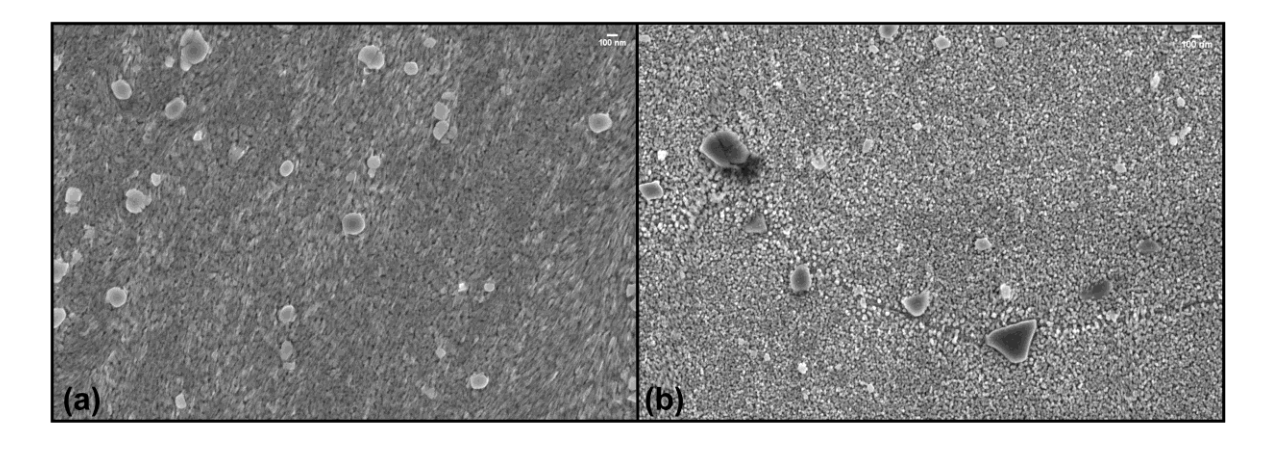


Figure 3.28. SEM image of heat-treated sample of IN939 at 1260°C taken with secondary electrons at 50.000x magnification in (a) XZ plane and (b) XY plane.

Furthermore, in the corresponding XY plane (Figure 3.28 (b)), the grain boundaries present a clean, precipitate-free state. This indicates that the heat treatment was effective in suppressing heterogeneous precipitation at the grain boundaries, thereby promoting intragranular γ' formation. Imaging at 100.000x magnification (Figure 3.29) provides a detailed view of the spherical morphology and distribution of the γ' (gamma prime) precipitates, including their configuration adjacent to the primary carbide particles in XZ (a) and XY(b) planes.

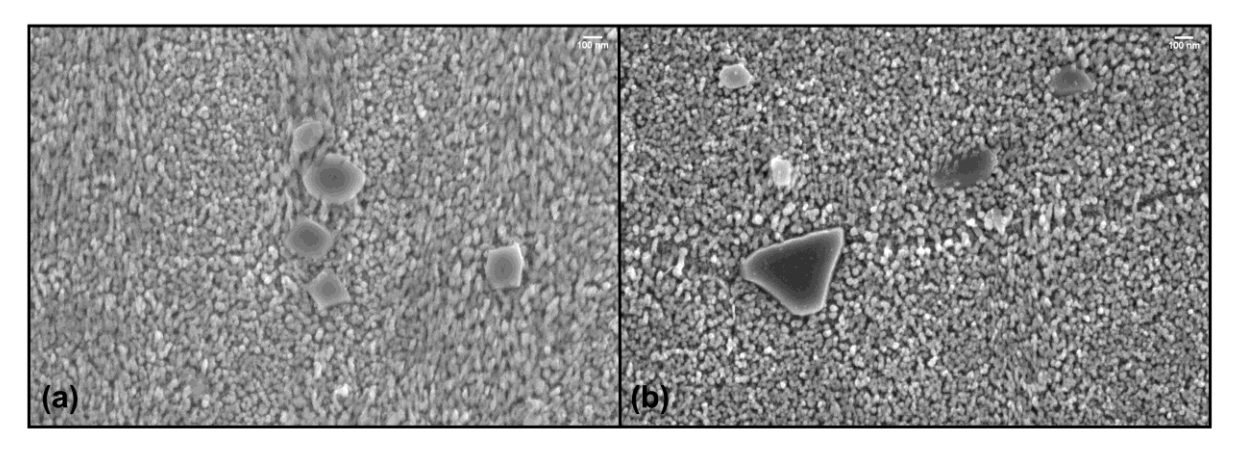


Figure 3.29. SEM image of heat-treated sample of IN939 at 1260°C taken with secondary electrons at 100.000x magnification in (a) XZ plane and (b) XY plane.

In Figure 3.30 in both XZ and XY planes microcracks are visible within the carbides.

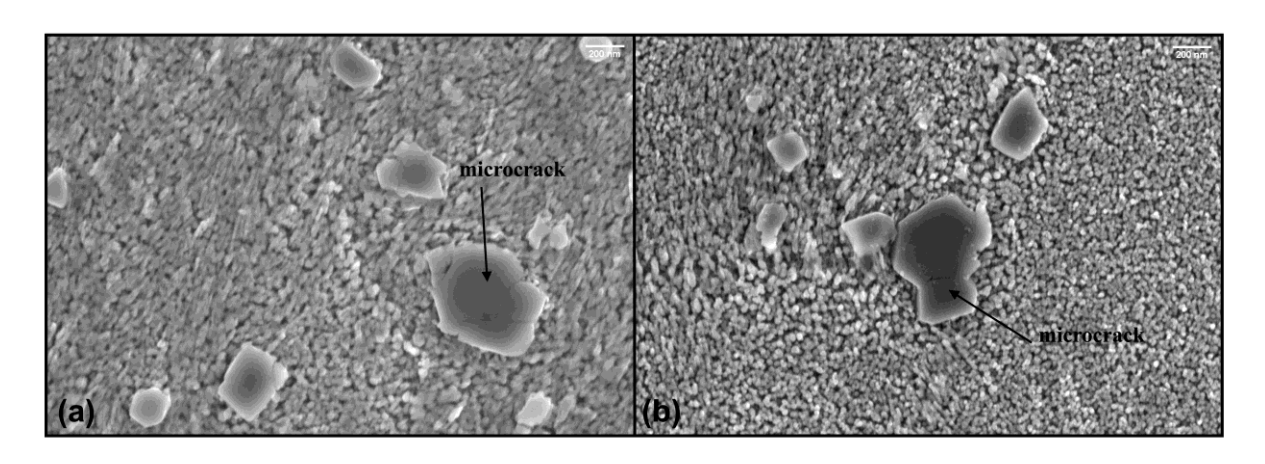


Figure 3.30. SEM image of heat-treated sample of IN939 at 1260°C taken with secondary electrons at 100.000x magnification.

A comprehensive investigation of the sample heat-treated at 1300°C was conducted using scanning electron microscopy (SEM) and energy-dispersive X-ray spectroscopy (EDS). The analysis focuses on characterizing the grain size and morphology, as well as identifying the precipitates, with particular emphasis on the composition and distribution of carbide phases.

Focusing on the sample treated at 1300 °C, in *Figure 3.31* a comparison of grains in XY (a) and XZ (b) is shown. These two images taken by light optical microscope at 50x magnification confirm that the grains have reached a similar geometry in both XY and XZ planes.

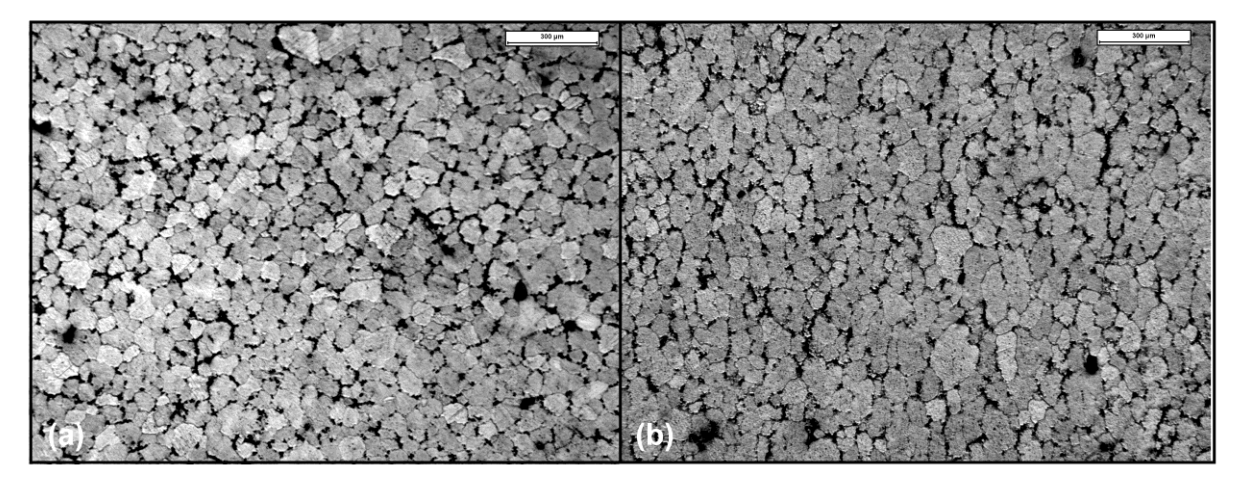


Figure 3.31. Grain microstructure of non-standard heat-treated samples IN939 at temperature of 1300°C at 50 x magnification in the (a) XY and (b) XZ planes.

In *Figure 3.32* it is possible to see the grains in both XY (a) and XZ (b) planes at a magnification of 500x and it is possible to appreciate the grain boundaries highlighted by severe carbides precipitation.

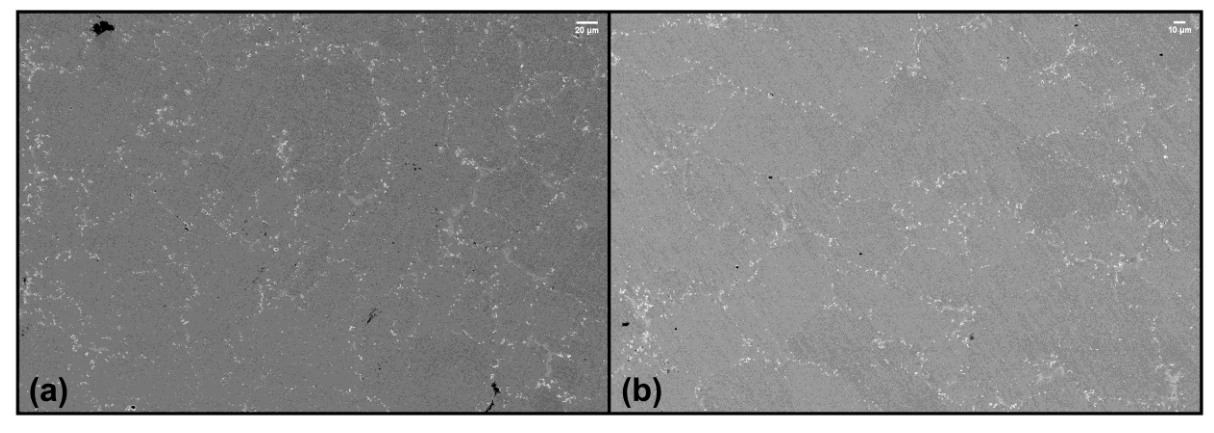


Figure 3.32. SEM image of heat-treated sample of IN939 at1300°C taken with backscattered electron at 500x magnification in (a) XY plane and (b) XZ plane.

Figure 3.33 allows a better visualization of the different types of precipitates present on the material after the treatment. Three types can be identified: the first type, occurring at grain boundaries with characteristic frequency, exhibits brighter contrast in backscattered electron imaging (highlighted in green rectangles), suggesting their heavier nature. The second type shows similar brightness levels but consists of finer particles distributed uniformly within grains (blue rectangles). The third type appears exclusively along grain boundaries (red rectangles), displaying distinct contrast characteristics from the first population.

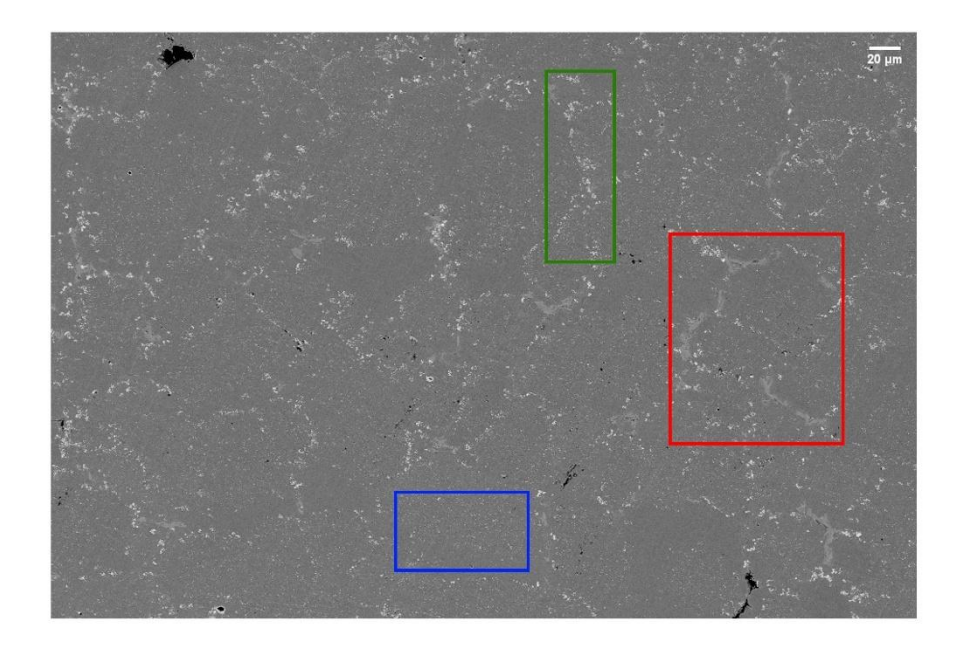


Figure 3.33. SEM image showing different types of precipitates in different colored rectangles.

The nature of precipitates in the green rectangle refers to MC carbides while a further investigation of the precipitates in red rectangles was carried out. A magnification of them is reported in *Figure 3.34*. The hypothesis suggests that this may be a eutectic phase formed from the liquid during solidification, enriched with elements that exhibit preferential liquefaction behavior.

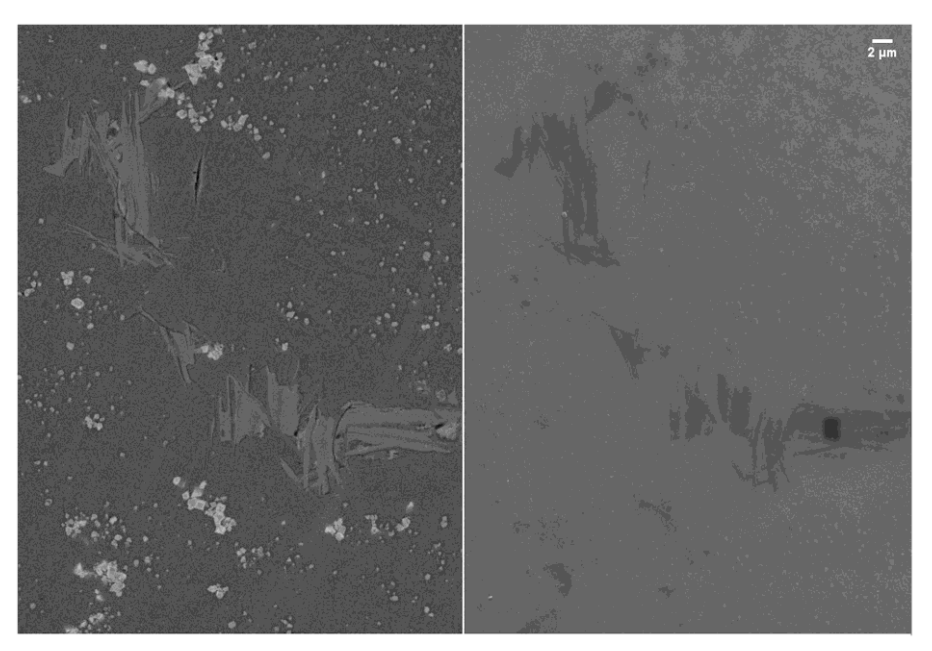


Figure 3.34. SEM image of heat-treated sample of IN939 at1300°C taken with backscattered electron(left) and secondary electron (right) showing phases formed from the liquid during solidification.

An EDS map analysis was conducted to understand the composition of the phases present in the red rectangles in image above. The results, presented in *Figure 3.35*, demonstrate that the brighter particles correspond to carbides enriched in Ti, Ta and W elements as expected, while the phase at the

center of the image shows a composition of Ni, Al with notably significant contribution from Ti and Nb, as evident in *Figure 3.35 (d)* and *(e)*.

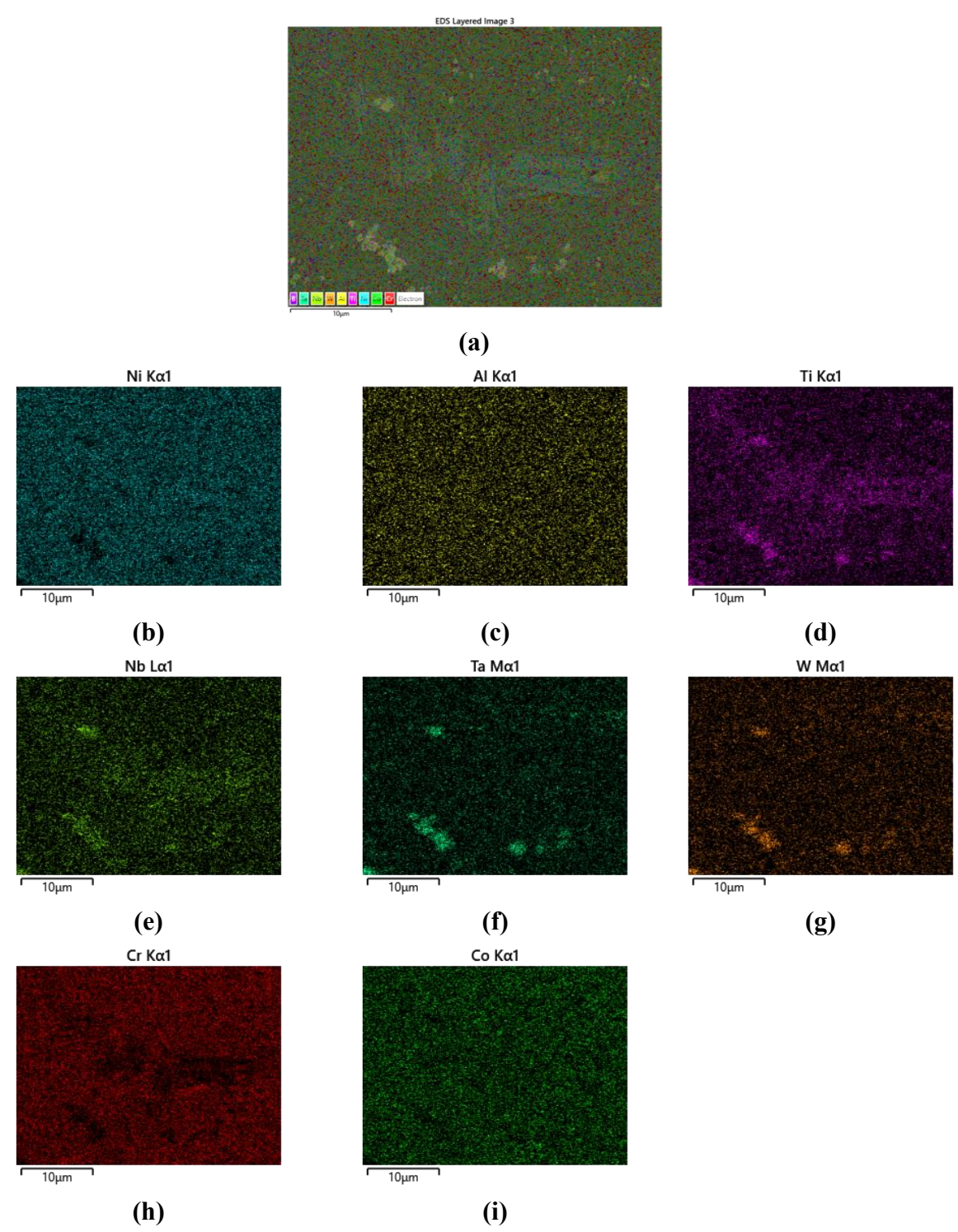
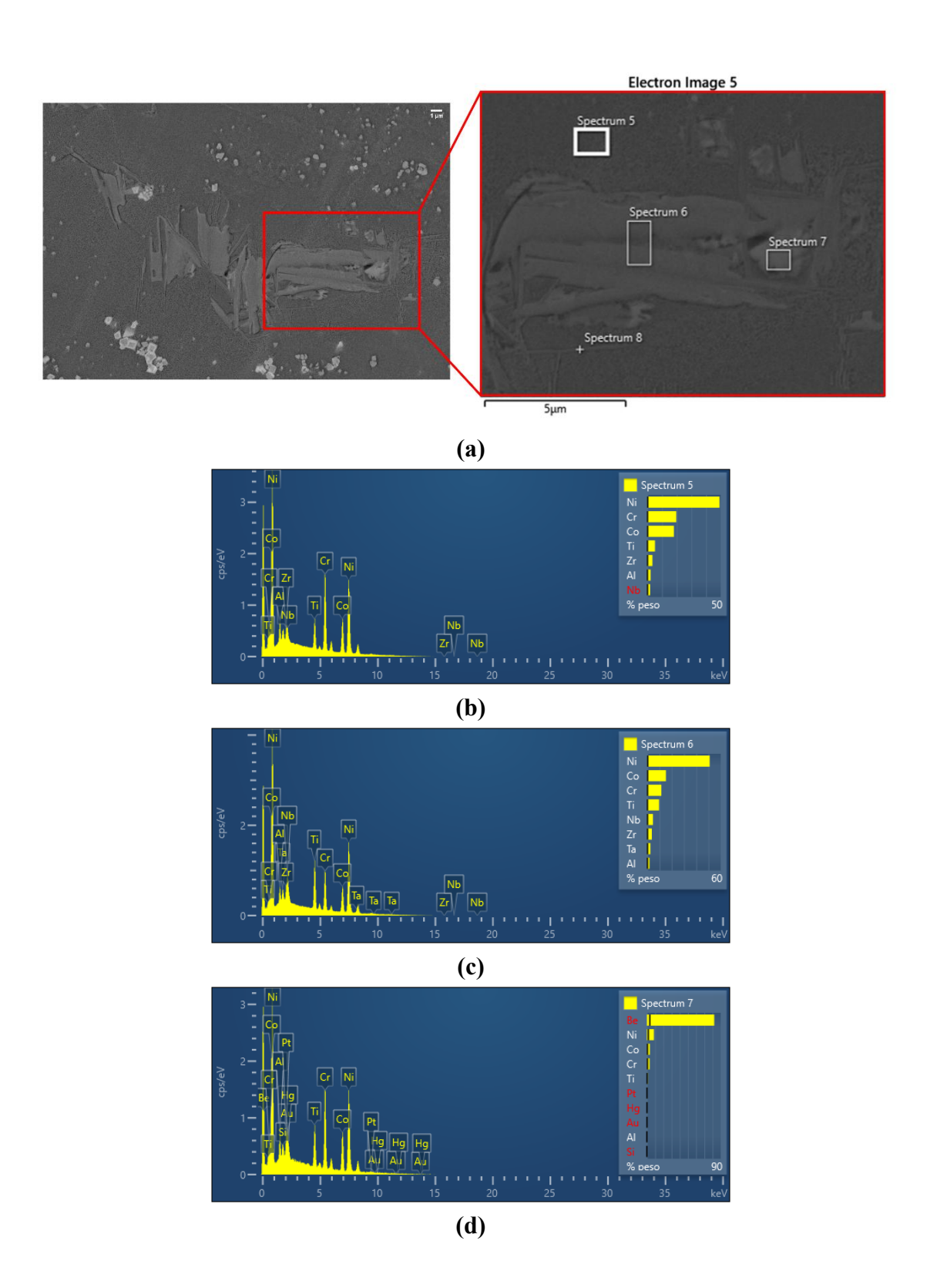


Figure 3.35. EDS survey on-air heat-treated sample at 1300°C.

To understand exhaustively the nature of these phases a point analysis by SEM was conducted. Four points were investigated. The first was fixed on the matrix whose composition enriched in Ni, and the presence of Cr and Co, is confirmed by the Spectrum5 in *Figure 3.36 (b)*. In Spectrum 6 (*Figure 3.36 (c)*) a high presence of Ti is visible, 9.5 wt%, and a consistent presence of Nb equal to 4.7 wt%.

Spectrum 7 in *Figure 3.36 (d)* related to the embedded particle confirms the nature of carbide, while Spectrum 8 in *Figure 3.36 (b)* is objective of a rigorous evaluation.



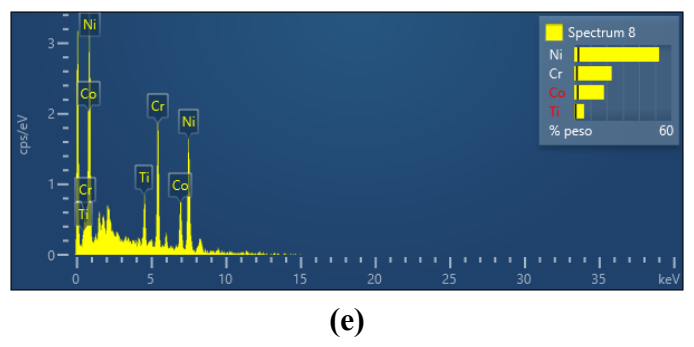


Figure 3.36. SEM image of heat-treated sample of IN939 taken with backscattered electron in XY plane (a) and specific area analyzed with EDS (b) spectrum 5, (c) spectrum 6, (d) spectrum 7 and (e) spectrum 8.

The chemical composition, acquired from Spectrum 8 in *Figure 3.22 (a)*, reveals a high titanium (Ti) concentration within these acicular features, about 6 wt.%. Combined with their distinct morphology, this provides conclusive evidence for their identification as the eta (η) phase. This phase as reported in Chapter1 is a detrimental phase that impedes the elevated temperature creep properties of the alloy. It exists in the form of platelets, which are formed at the periphery of the γ/γ eutectic [35]. In *Figure 3.37* is shown η phase formed during casting process investigated in the article.

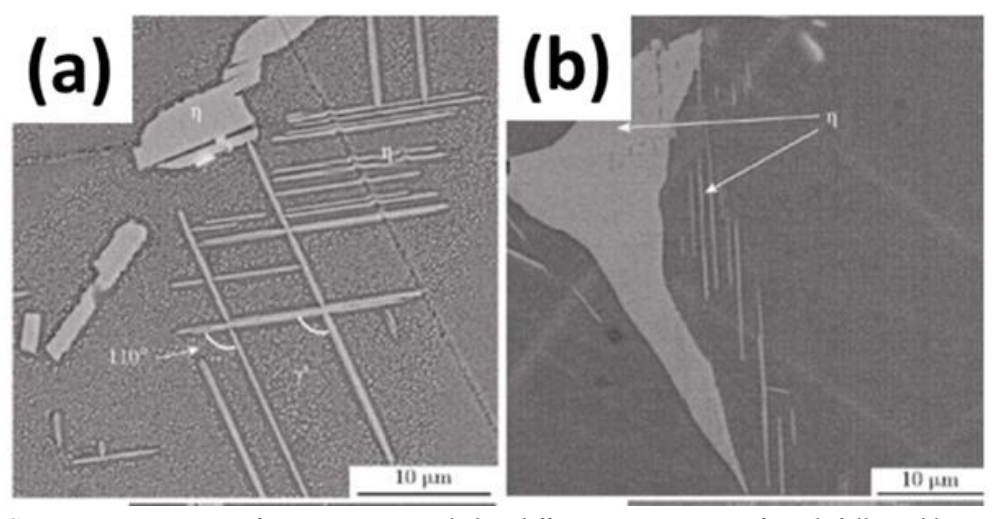


Figure 3.37. SEM microstructures of specimens annealed at different temperatures for 4 h followed by water quenching: (a) 1100° C, (b) 1150° C [35].

Elements like Titanium are pushed into the remaining liquid, creating localized regions that are incredibly rich in Ti becoming perfect sites for the η phase nucleation and growth. Eta phase typically dissolves at temperature above 1150°C [35], meaning that it has formed upon cooling. Further point analysis in SEM was performed and is reported in *Figure 3.38*.

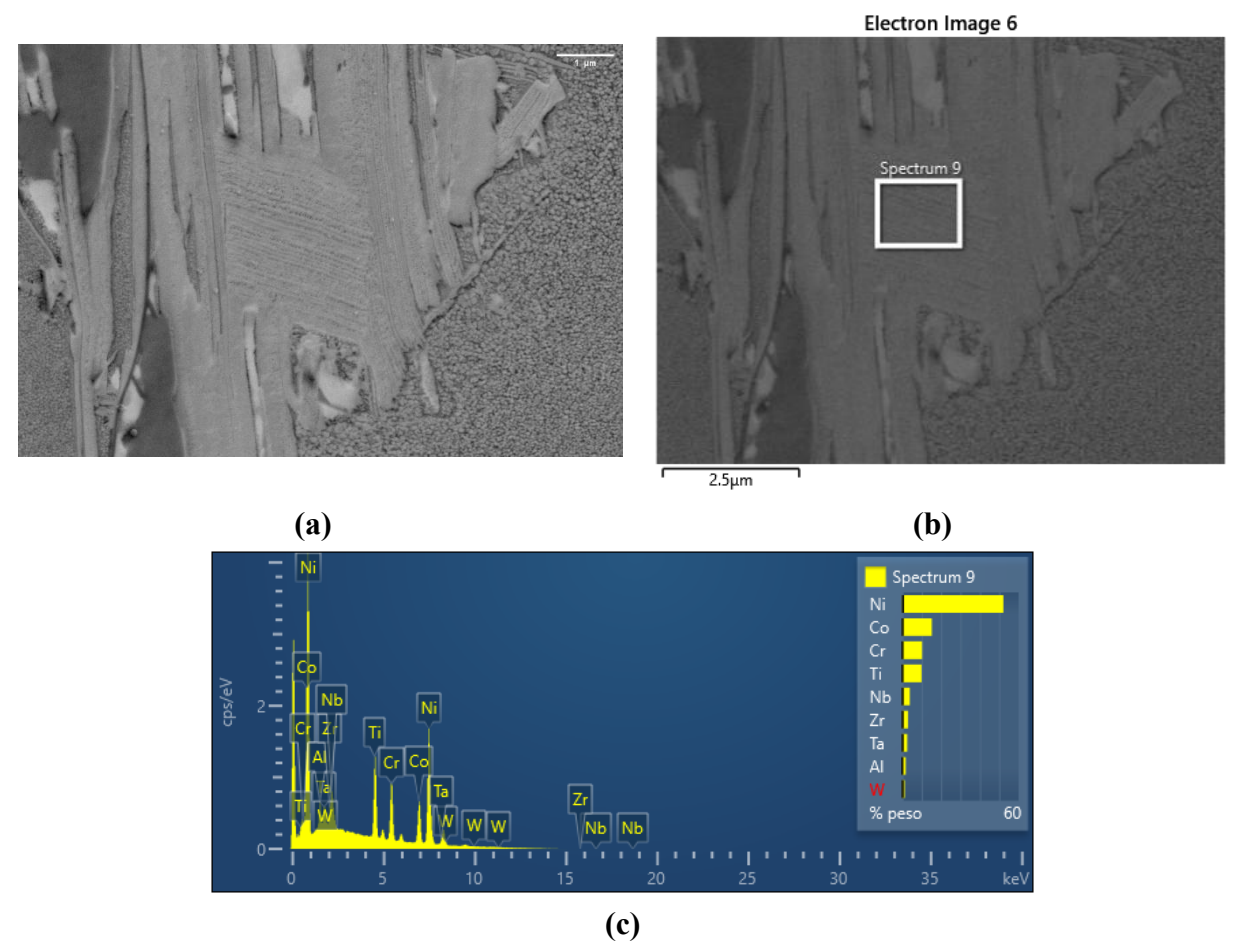


Figure 3.38. SEM image of heat-treated sample of IN939 taken with backscattered electron in XY plane(a) and specific area analyzed with EDS (b) spectrum 9 (d).

It is possible to notice the typical lamellar structure between the phases.

Depending on the composition of the primary MC carbide and the constituent elements present in the alloy, subsequent solid-state transformation can decompose the MC carbide into the variety of $M_{23}C_6$ and M_6C carbides during heat treatment or in service. Carbides such as $M_{23}C_6$ form at lower temperatures, around 750 °C, during protracted periods of service exposure, particularly in alloys which are rich in Cr [6]. Their formation has been attributed to the breakdown of the MC carbides, via reaction (1.1) and (1.2) reported in Chapter 1. The $M_{23}C_6$ carbide is favored by exposure temperatures of about 790 to 820 °C and it's usually found to precipitate on the γ -grain boundaries [6].

The spectrum reported in *Figure 3.38 (c)* reveals the presence of all constituent elements. A key finding is the significant titanium content, measured at 10 wt%, which substantiates a direct association with carbide formation. This phase is likely a eutectic compound consisting of MC-type carbides that have reacted with the matrix, as indicated by the formula provided.

In Figure 3.39 it is possible to appreciate gamma prime, carbides as brighter areas and η phase with its platelet shape.

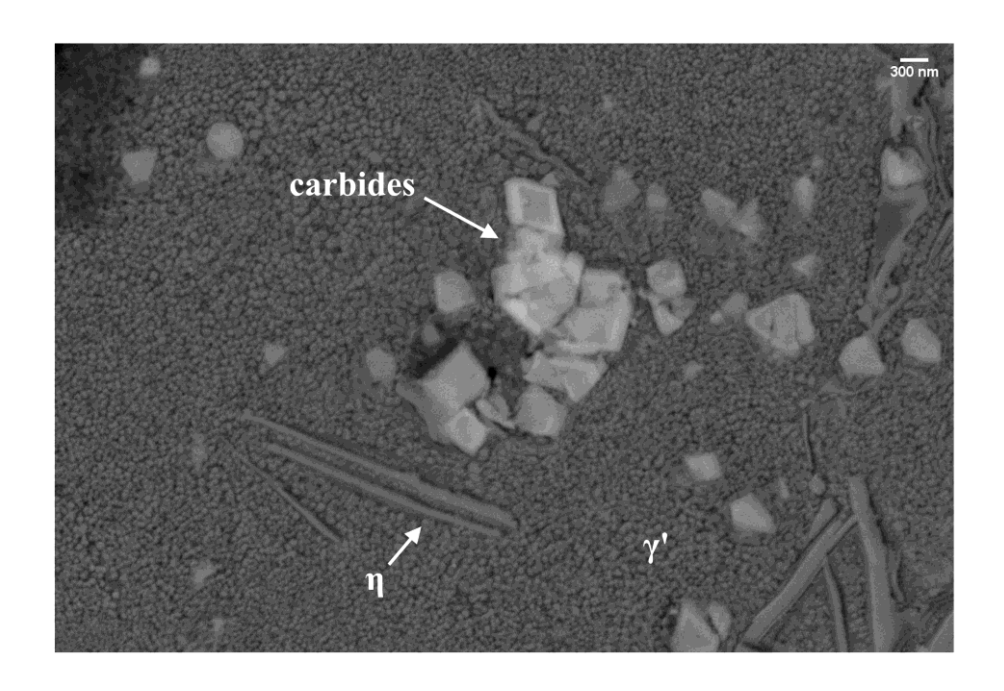


Figure 3.39. SEM image of heat-treated sample of IN939 taken with backscattered electron showing carbides, gamma prime and η phase.

The chemical etching with oxalic acid was successful and highly effective as it revealed all microstructural features. The carbides remain unaffected by the etchant, while the matrix is selectively dissolved, allowing the γ' (gamma prime) precipitates to be clearly highlighted. In XY plane (Figure 3.40 (a) and (b)) gamma prime presents a dimension of the order of 34 nanometers, so it is very fine but extremely irregular. On the other hand, the γ' precipitates in the XZ-plane appear coarser. Their size distribution is heterogeneous, with some regions exhibiting finer precipitates and others coarser ones as it is possible to appreciate in Figure 3.40 (c). This non-uniformity suggests a local variation in coarsening kinetics. The coarser γ' is observed in proximity to carbides, likely due to local chemical segregation of γ' -forming elements (e.g., Al, Ti) to these regions during processing. Conversely, the interfacial region near certain phases as shown in Figure 3.40 (e) is devoid of γ' , or it is present in an extremely fine form. Figure 3.40 (f) shows a high-magnification view (500.000x) of the γ' precipitates, revealing their detailed morphology.

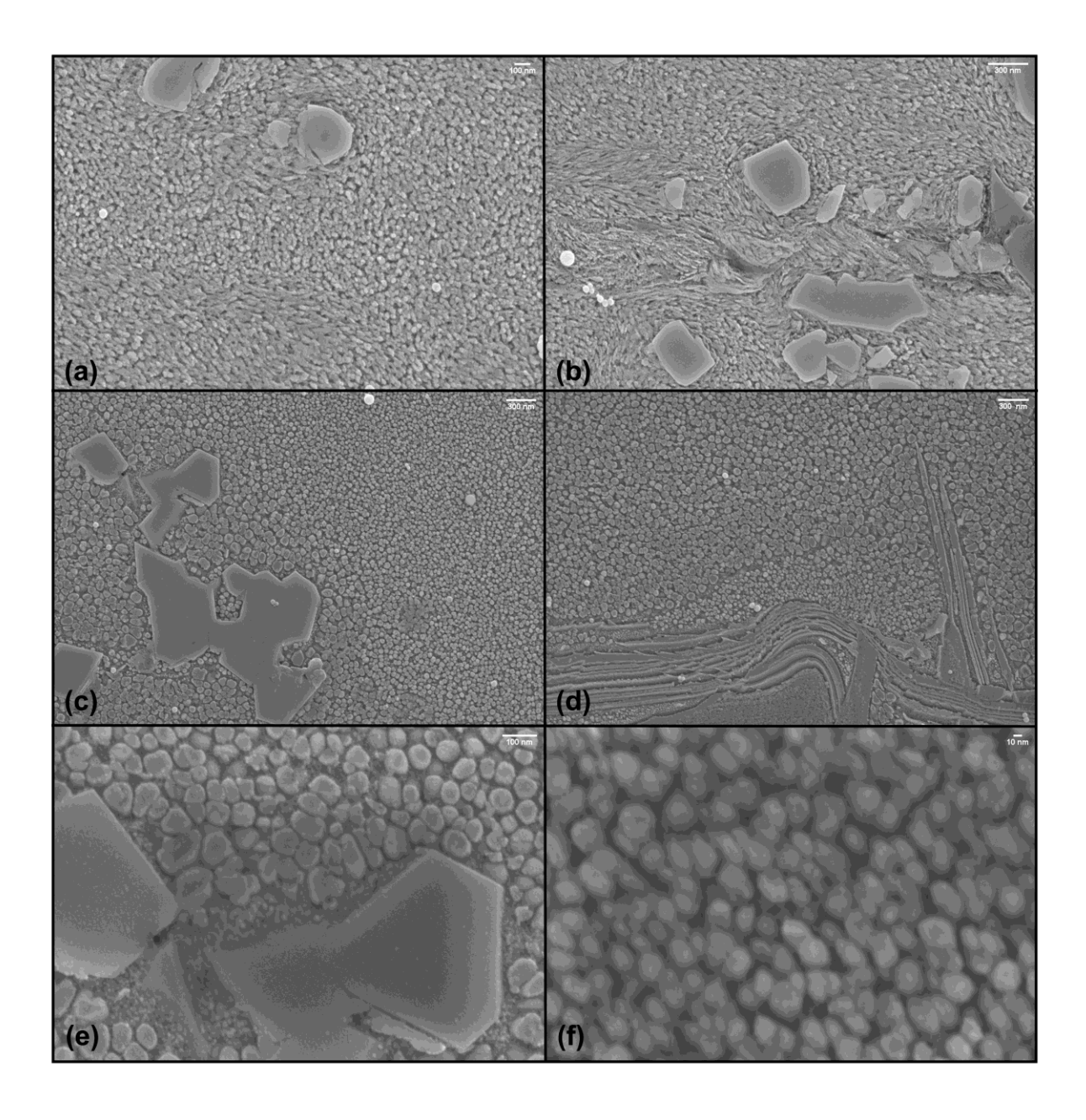


Figure 3.40. SEM image of heat-treated sample of IN939 taken with secondary electron showing carbides and γ' in XY plane (a) and (b) and in XZ plane (c,) (d,) (e) and (f).

Pertaining to the investigation of defects, *Figure 3.41* reveals significant microstructural damage within the resolidified zone, contrasting with the adjacent, unaffected carbide. This damage is consistent with the known poor weldability of this class of alloys, which are prone to cracking during thermal cycling. The grain boundaries exhibit an irregular and serrated morphology. This is attributed to incipient melting at these locations during the process, followed by subsequent solidification. Another evidence of incipient melting is the presence of some spherical features visible in the figure. They are dendritic solidification structures which form from the solidification of liquid pools. A microcrack is evident in *Figure 3.41* (b).

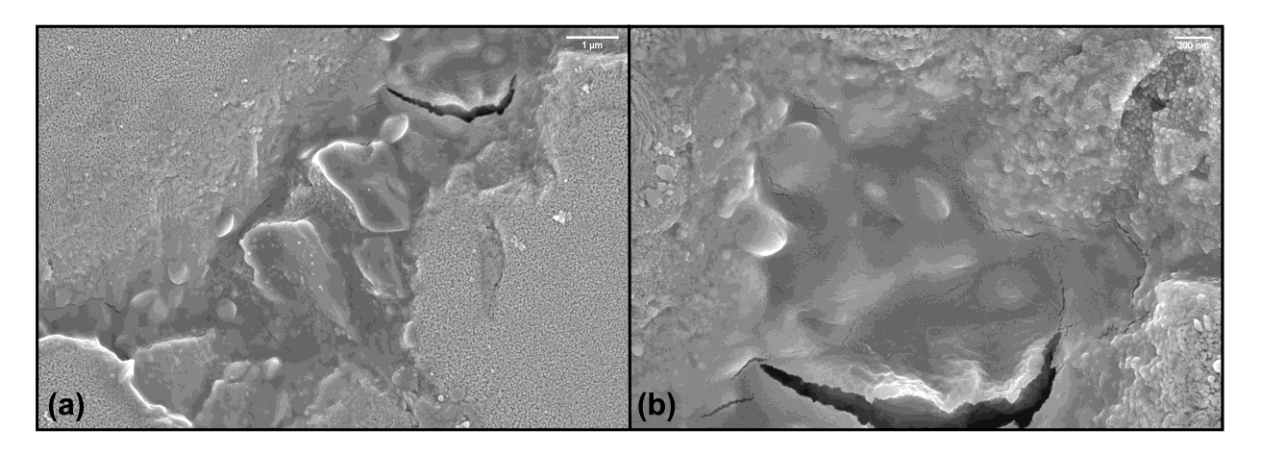


Figure 3.41. SEM image of heat-treated sample of IN939 taken with secondary electron in XY plane at (a) 26.000x magnification and (b) and 61.000x magnification.

The anomalies observed in the upper section are attributable to the thermal treatment. In contrast, the defects potentially stem from the initial manufacturing process are visible in *Figure 3.42*. These defects are lack of fusion, typical of additive manufacturing process, characterized by unmelted powder particles that occur when the laser energy is insufficient to fully melt the material during LPBF process. Unmelted powder particles are clearly visible in the void shown in *Figure 3.42* (a).

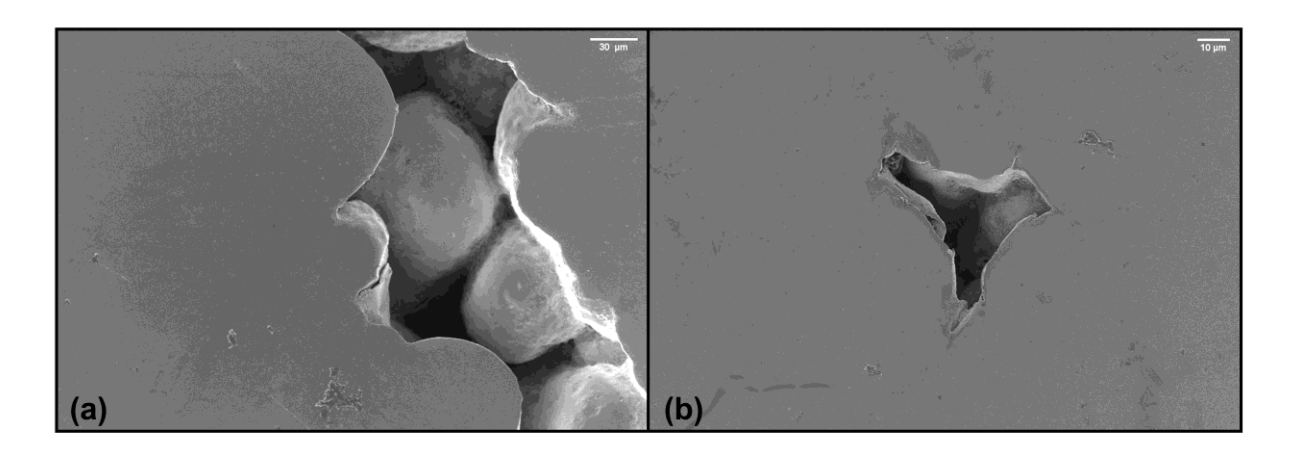


Figure 3.42. SEM image of heat-treated sample of IN939 taken with secondary electron showing damaged areas in XZ plane at (a) 26.000x magnification and (b) and 61.000x magnification.

An investigation of other types of defects was carried out and it is shown in *Figure 3.43*. A point and a map analysis with EDS revealed that a high concentration of Ti is present on the edge of the cavity as it is possible to appreciate in *Figure 3.43* (c). The residue within this cavity, which contains a high concentration of polishing-derived elements like Si (*Figure 3.43* (e)), confirms that it is a void that trapped contaminants during preparation. Spectrum 4 confirms that in the vicinity of fused macroareas there is a significant presence of Titanium (Ti), about 8.97 wt%.

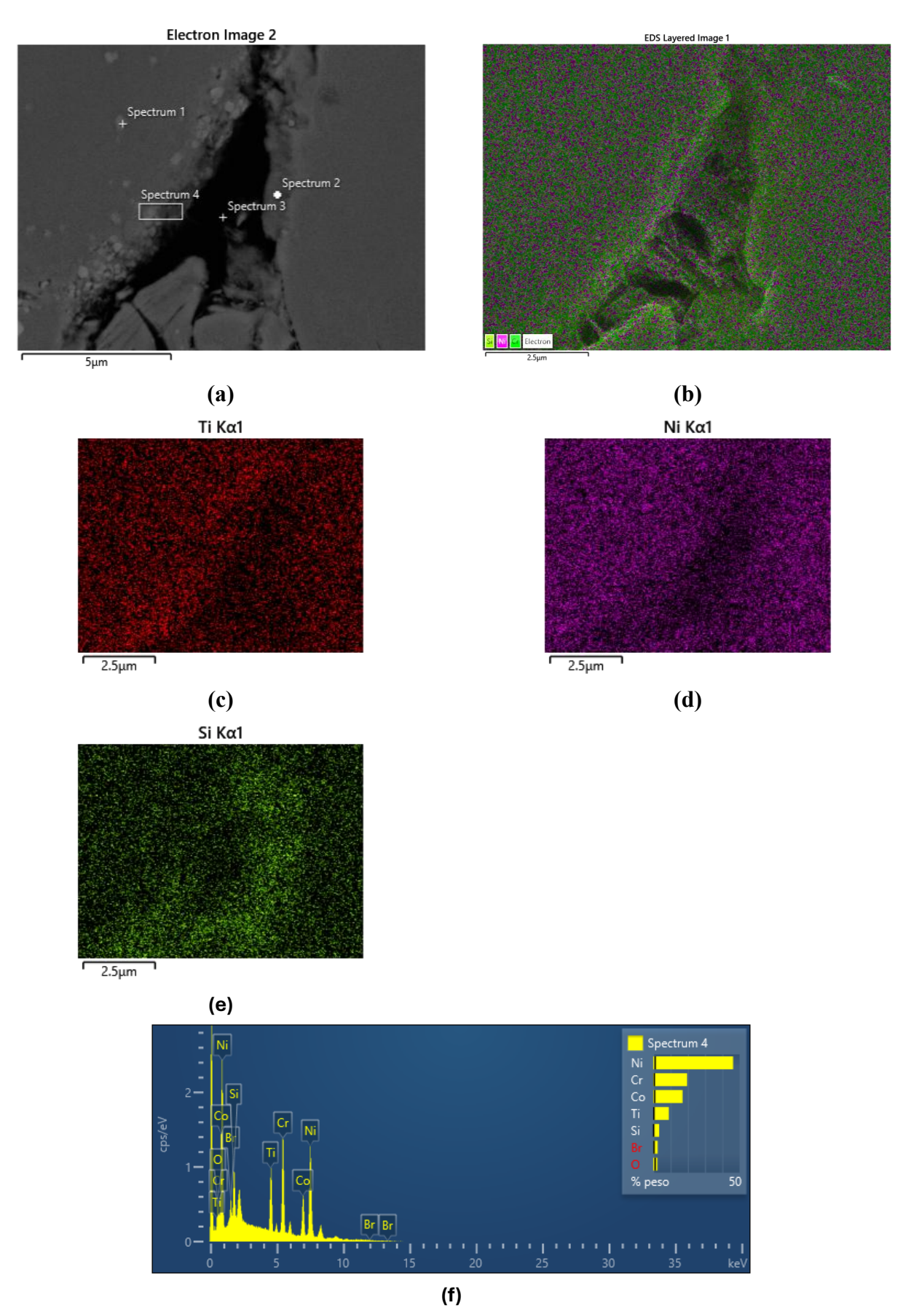


Figure 3.43. Sample treated at 1300°Cin air: (a) SEM micrograph where spectrum 4 is obtained, (b)EDS map analysis, (c) Ti distribution, (d)Ni distribution, (e)Si distribution and (f) EDS spectrum 4.

Concerning a map analysis of carbides, it is possible to appreciate a high concentration of elements such as tungsten, titanium and tantalum visible in *Figure 3.44 (b), (c)* and *(d),* composition typical of MC carbides. The characteristic blocky morphology and angular shape observed in *Figure 3.44 (a)* are consistent with those of carbide phases.

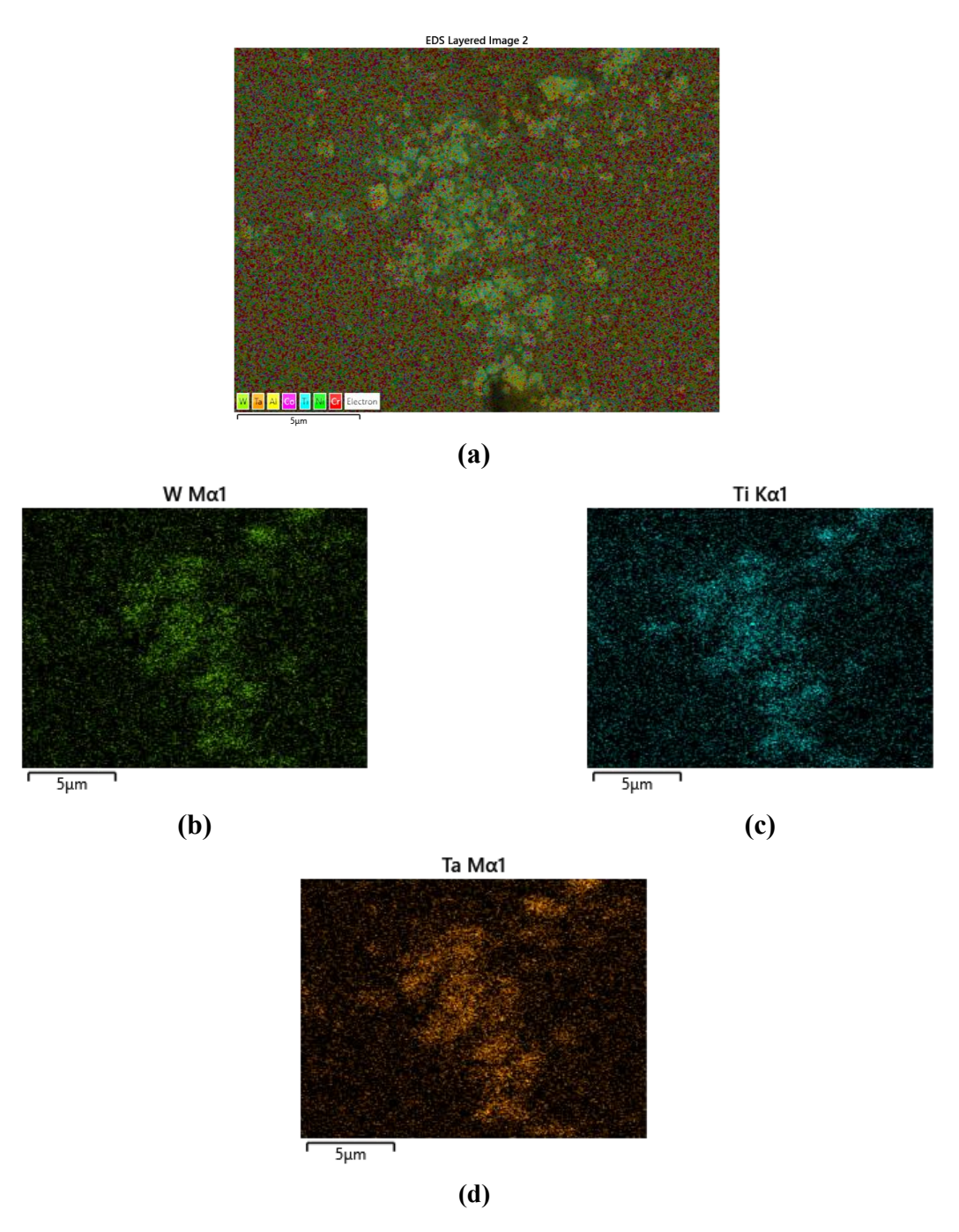


Figure 3.44. EDS map analysis on-air heat-treated sample at 1300°C showing carbides.

The analysis indicates that the sample heat-treated at 1300°C exhibits a greater degree of defects in the XZ cross-section compared to the XY plane.

In conclusion, it can be stated that a temperature of 1300° C is sufficient to activate significant diffusion processes. At this temperature, γ' (gamma prime) phase has dissolved into the solid solution. However, coarse primary carbides persist within the grain interiors. An irregular distribution of carbides is observed. While some grains are entirely devoid of these precipitates, specific grain

boundaries are extensively populated with carbides. These precipitates likely nucleated as a consequence of the selective diffusion of carbide-forming elements during thermal processing Elements such as Titanium (Ti) and Tantalum (Ta) migrate toward the grain boundaries, where they contribute to the formation of these types of secondary precipitates upon cooling. A representative example of this microstructure is provided in *Figure 3.45*.

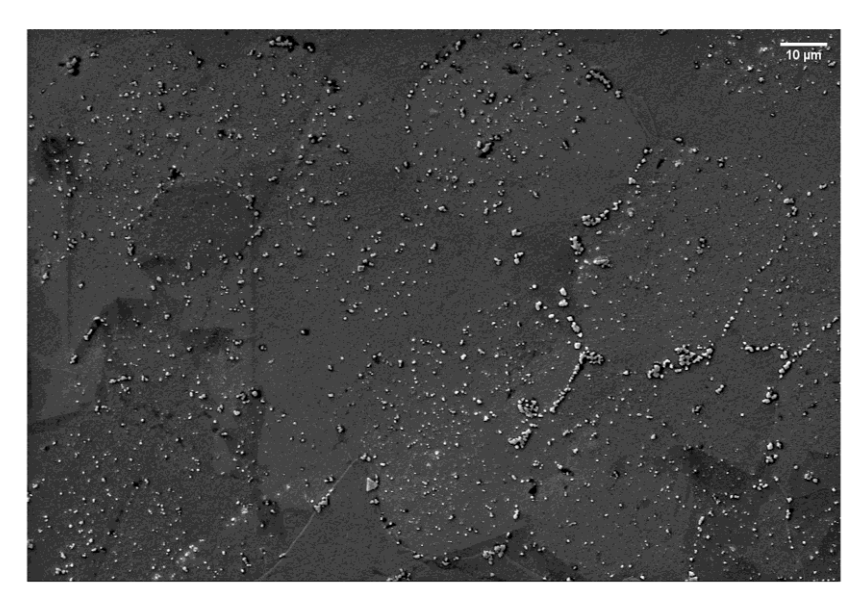


Figure 3.45. SEM image of heat-treated sample of IN939 taken with secondary electron in XY plane at 20.000x magnification.

In conclusion, microstructural analysis confirms a predominantly spherical morphology for the γ' (gamma prime) precipitates, with localized regions exhibiting significant irregularity. While no substantial differences were observed in the overall γ' distribution between the XZ and XY planes. The only peculiarity is a evident alignment of gamma prime within the XZ plane that could be interpreted as a microstructural legacy, retaining a directional signature imparted by the underlying columnar grain structure from the solidification process.

Analysis of the samples heat-treated at the previously presented different temperatures indicates that moving to melting point and especially in its proximity, significant solid-state diffusion occurs. This diffusion drives the segregation of elements such as Ti and Ta to the grain boundaries.

3.3 Characterization of hipped IN939 samples

Building upon a prior investigation into the Hot Isostatic Pressing (HIP) of Inconel 939[51], which was developed to assess the feasibility of HIP processing above the alloy's solidus temperature, a Design of Experiments (DOE) approach was employed to identify the optimal parameter set. The HIP process is governed by three fundamental and controllable parameters known to significantly influence the resultant microstructure: temperature, time, and pressure. Based on established literature indicating that applied pressures for Ni-based superalloys typically exceed 100 MPa, the selected pressure levels for this study were 100 MPa, 125 MPa, and 150 MPa. Analysis following the "larger is better" criterion identified the optimal pressure as 125 MPa, so this study considers only this value. The processing time is set at 240 hours to maintain coherence with standard air heat treatment

protocols for this material. Three distinct temperatures are investigated: 1260°C, 1280°C, and 1300°C. Subsequent microstructural analysis of the heat-treated samples revealed that the highest temperature, 1300°C, resulted in the formation of an extensive liquid-phase region throughout the sample volume. Consequently, this thesis focuses on a detailed analysis of the microstructural evolution at this critical temperature, providing a direct comparison between conventional air heat treatment and HIP processing. Accompanying figure presents the thermograms, illustrating the precise temperature and pressure profiles applied over time during the HIP cycles for samples processed at 1300°C (*Figure 3.46*).

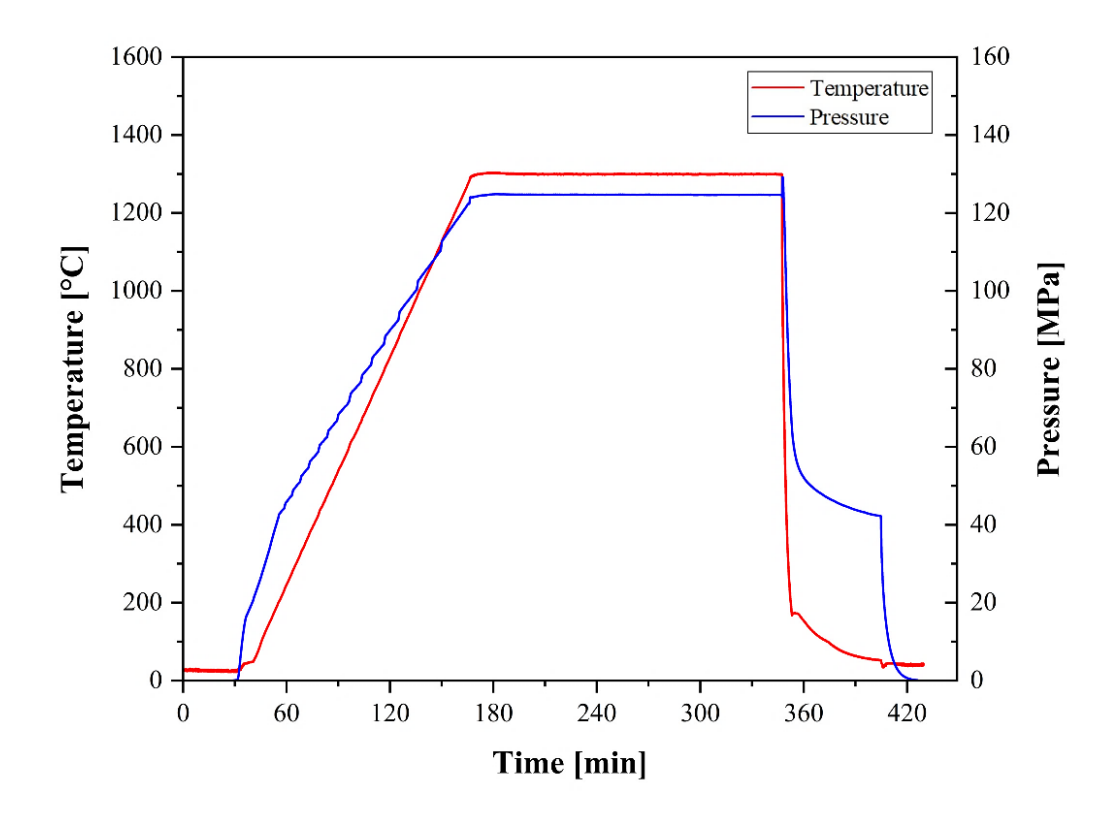


Figure 3.46. Temperature and pressure curves in HIP cycle for the temperature equal to 1300°C.

For the sake of brevity and clarity, the graphs corresponding to the other two processes are omitted from the presentation. Their behavior is analogous to that depicted in *Figure 3.46*, with the peak temperature being the sole distinguishing parameter.

The grain size analysis on the three HIPped samples reveals a critical non-linear relationship between temperature and grain growth in nickel-based superalloys as shown in *Figure 3.47*. The observed trend indicates significant grain coarsening between 1260°C and 1280°C, followed by a slight decrease in average grain size at 1300°C. The significant grain growth observed between 1260°C and 1280°C is a classic result of thermally activated grain boundary migration, enhanced by the application of isostatic pressure [54]. The critical event at 1300°C is that this temperature likely exceeds the alloy's solidus temperature. The slight decrease in grain size is a classic indicator of incipient melting. The liquid phase that forms at grain boundaries pins and isolates grains. This small amount of liquid phase formed in these zones rich in lower-melting-point eutectics (e.g., γ/γ ' or TCP phases) alters the mechanics of densification and coarsening causing grain refinement through boundary pinching and fragmentation, explaining the slight decrease in average grain diameter [54].

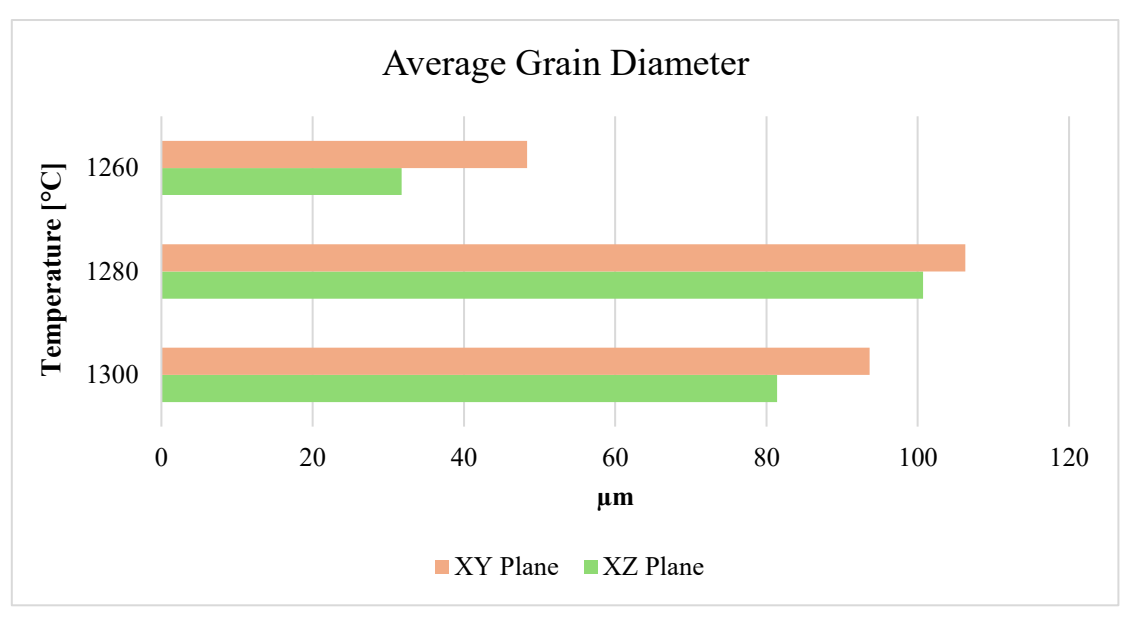


Figure 3.47. Comparison of average grain diameters samples under HIP processes.

The results obtained from the Hot Isostatic Pressing (HIP) process, following comprehensive microstructural characterization, are presented and discussed in the following sections. The initial qualitative assessment was conducted via optical microscopy (OM). The OM investigation established that the HIP-treated samples were fully densified and free from detectable porosity, indicating the process's high efficacy in eliminating void spaces inherited from the initial manufacturing stages.

3.3.1 Sample 1: 1260 °C – 125 MPa – 240 min

The microstructural evaluation of the sample subjected to Hot Isostatic Pressing (HIP) at 1260 °C reveals a columnar grain structure in XZ direction. The persistence of this non-equiaxed morphology suggests that the recrystallization process was not carried to completion, halting before the formation of a fully recrystallized, equiaxed grain structure. These columnar grains are visible in *Figure 3.48*.

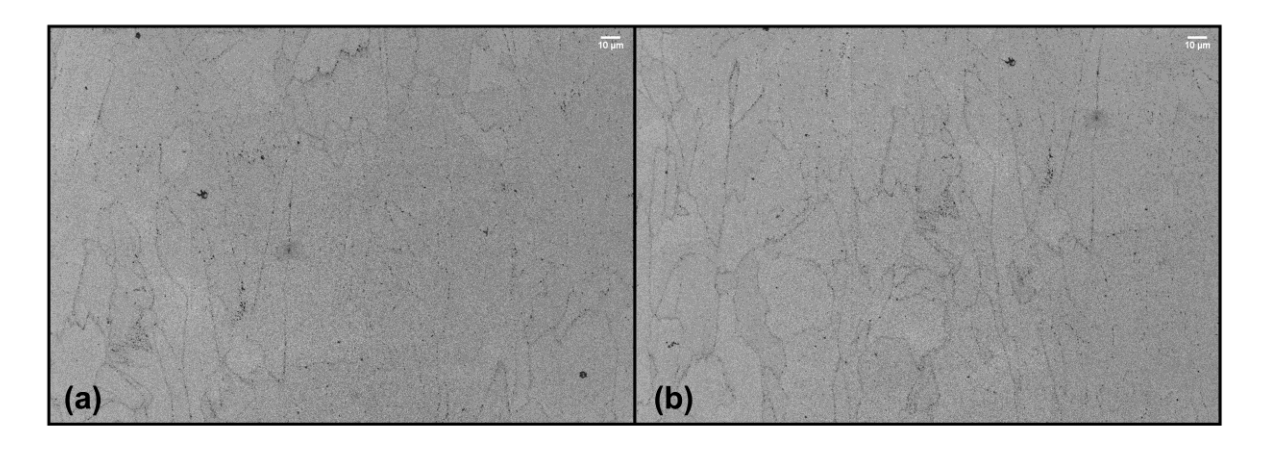


Figure 3.48. SEM image of hipped sample of IN939 at 1260° C taken with secondary electrons at 1.000x magnification in XZ plane.

The analysis of grain morphology and evolution was previously performed using optical microscopy (OM). This technique provided a fundamental, large-scale overview of the microstructure, allowing for the initial assessment of grain size distribution, shape, and general arrangement. The results of this analysis, which corroborate the finer details resolved via SEM, are presented in *Figure 3.49*.

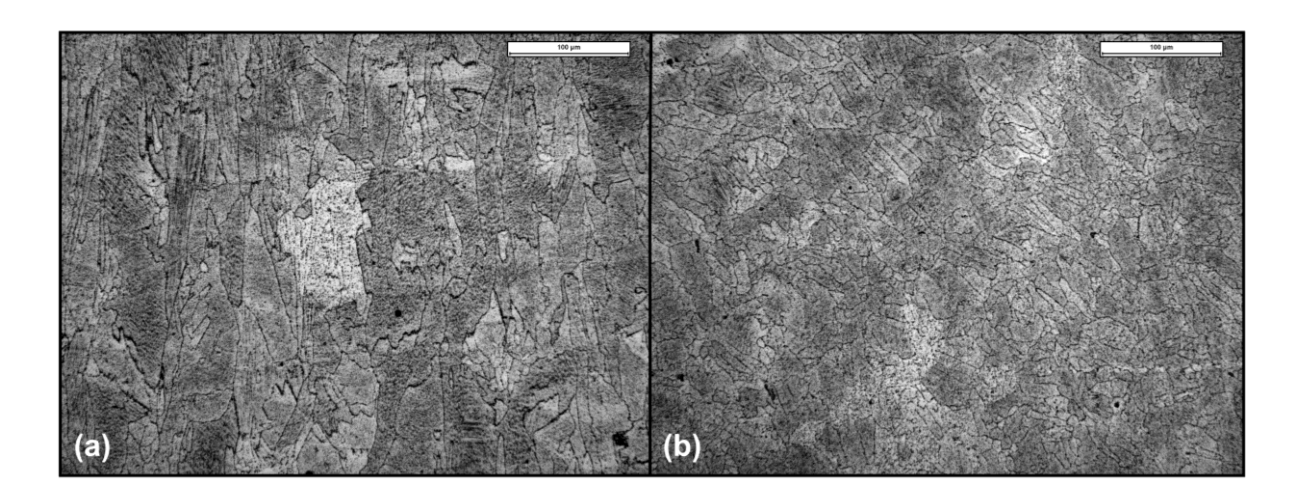


Figure 3.49. Optical Microscope image of solution heat-treated sample of IN939 at 200x magnification in (a) XZ plane and (b) XY plane.

Microstructural analysis of carbides reveals a notable limited presence within this sample. As evidenced in *Figure 3.50*, the carbide population is less dense, and the particles are less prominent in both the longitudinal and transverse orientations.

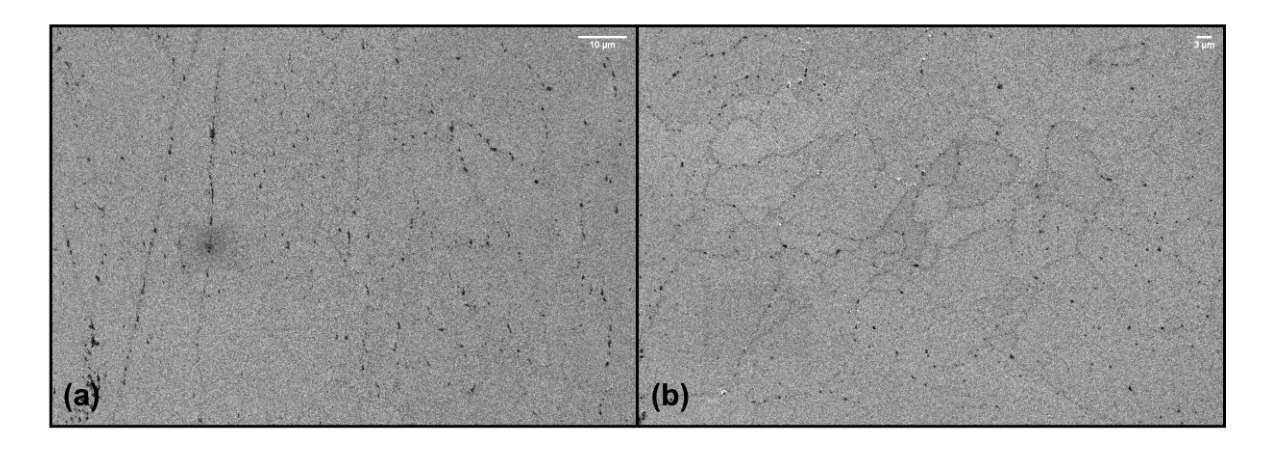


Figure 3.50. SEM image of hipped sample of IN939 at 1260°C taken with secondary electrons at 2.500x magnification in (a) XZ plane and (b) XY plane.

In XZ plane, γ' precipitates shows a morphology that is significantly influenced by the cooling rate, leading to a distinct difference between HIPped and air-cooled samples. *Figure 3.51* demonstrates that the HIP process, with its inherently lower cooling rate, results in a coarse and less dense distribution of spherical γ' precipitates. This contrasts with the finer, more numerous γ' formation resulting from the sample heat treated presented before.

As shown in *Figure 3.51 (b)*, M₂₃C₆ carbides are predominantly located at the grain boundaries, forming a near-continuous network. This situation is according to the reaction (1.1) explained in Chapter1.

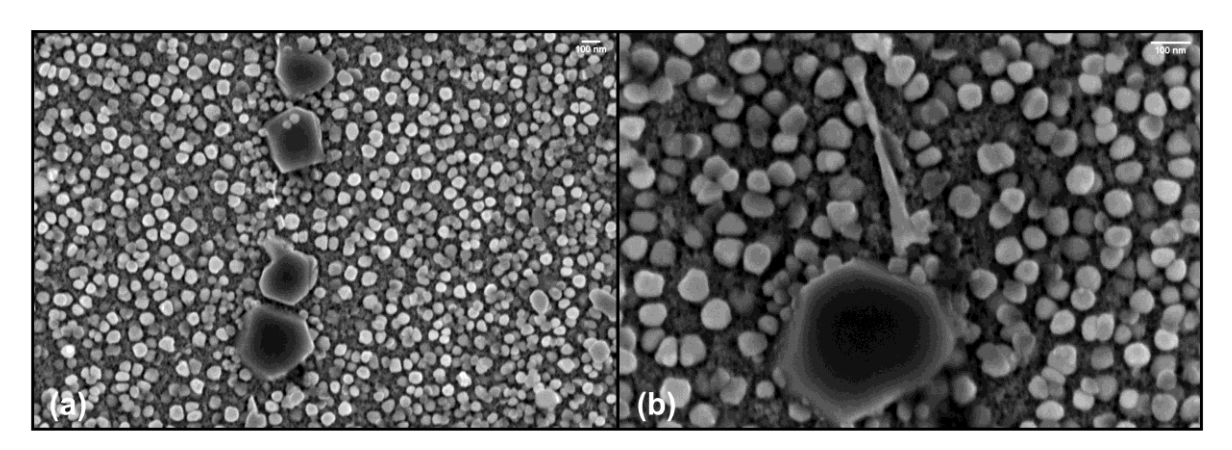


Figure 3.51. SEM image of hipped sample of IN939 at 1260°C taken with secondary electrons in XZ plane (a) at 100.000x magnification in (b)200.000x magnification.

In XY plane, M₂₃C₆ carbides are not present along the growth direction with the same continuity observed in XZ orientation. Instead, Ta-rich and Ti-rich carbides are more prevalent at the grain boundaries in this region (*Figure 3.52*).

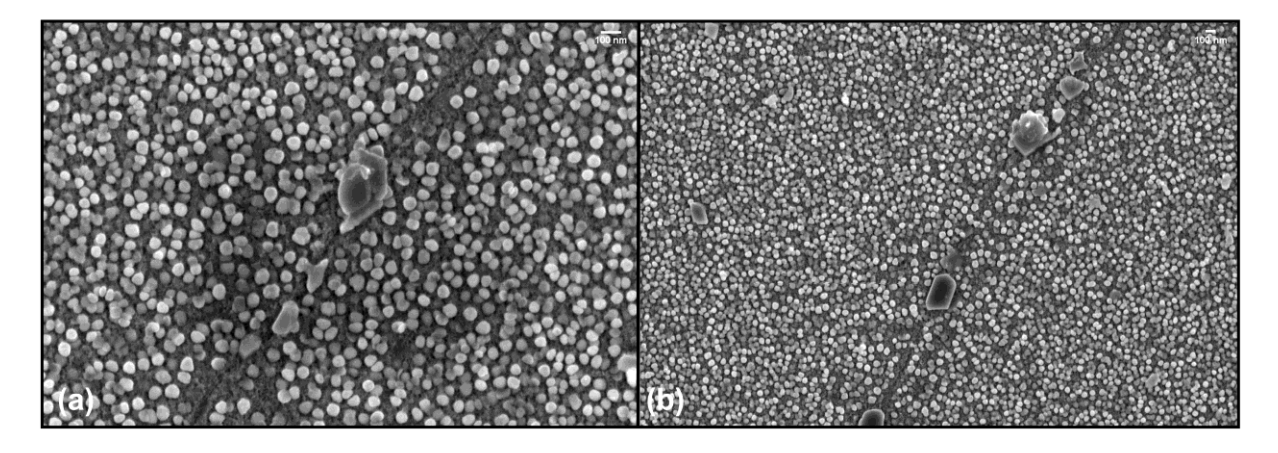


Figure 3.52. SEM image of hipped sample of IN939 at 1260°C taken with secondary electrons in XY plane (a) at 100.000x magnification in (b)50.000x magnification.

A representative M₂₃C₆ carbide is indicated in *Figure 3.53*.

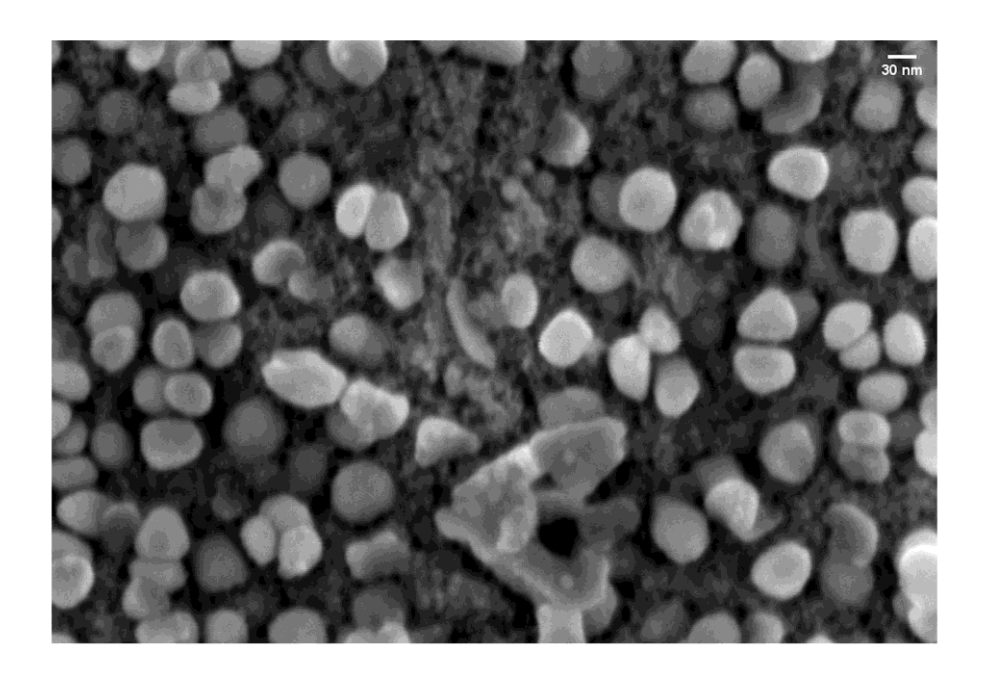


Figure 3.53. SEM image of hipped sample of IN939 at 1260°C taken with secondary electrons in XY plane showing $M_{23}C_6$ carbide.

Figure 3.54 displays an optical micrograph in which the characteristic dispersion and morphology of carbide particles within the grains is evident in both the planes analyzed.

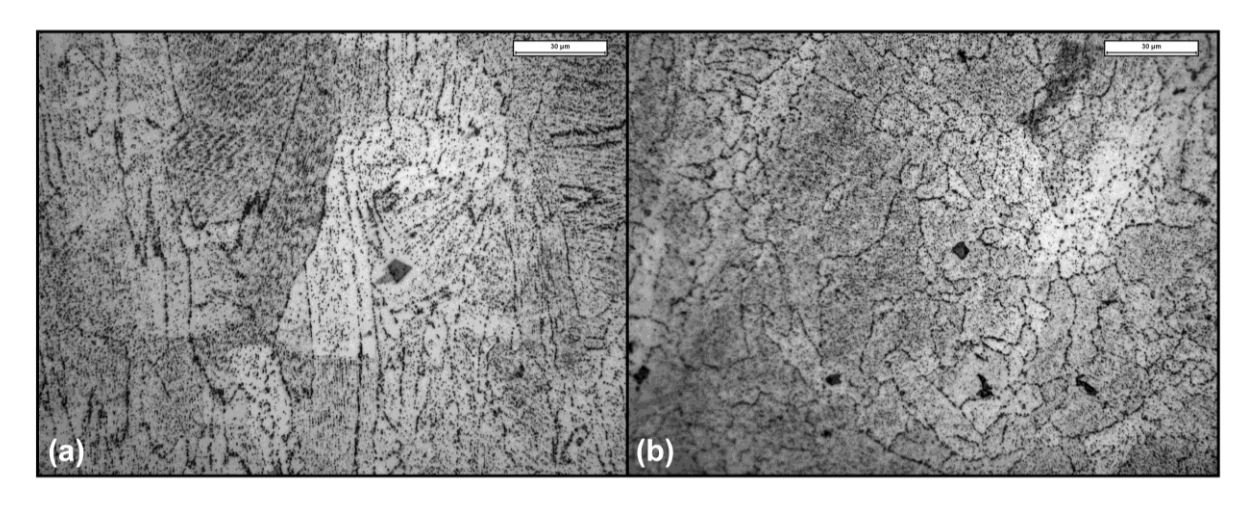


Figure 3.54. Optical Microscope image of solution heat-treated sample of IN939 at 500x magnification in (a) XZ plane and (b) XY plane.

In the XY orientation, the γ' precipitates also possess a spherical shape and a fairly regular distribution as it is possible to appreciate in *Figure 3.55* at different magnifications.

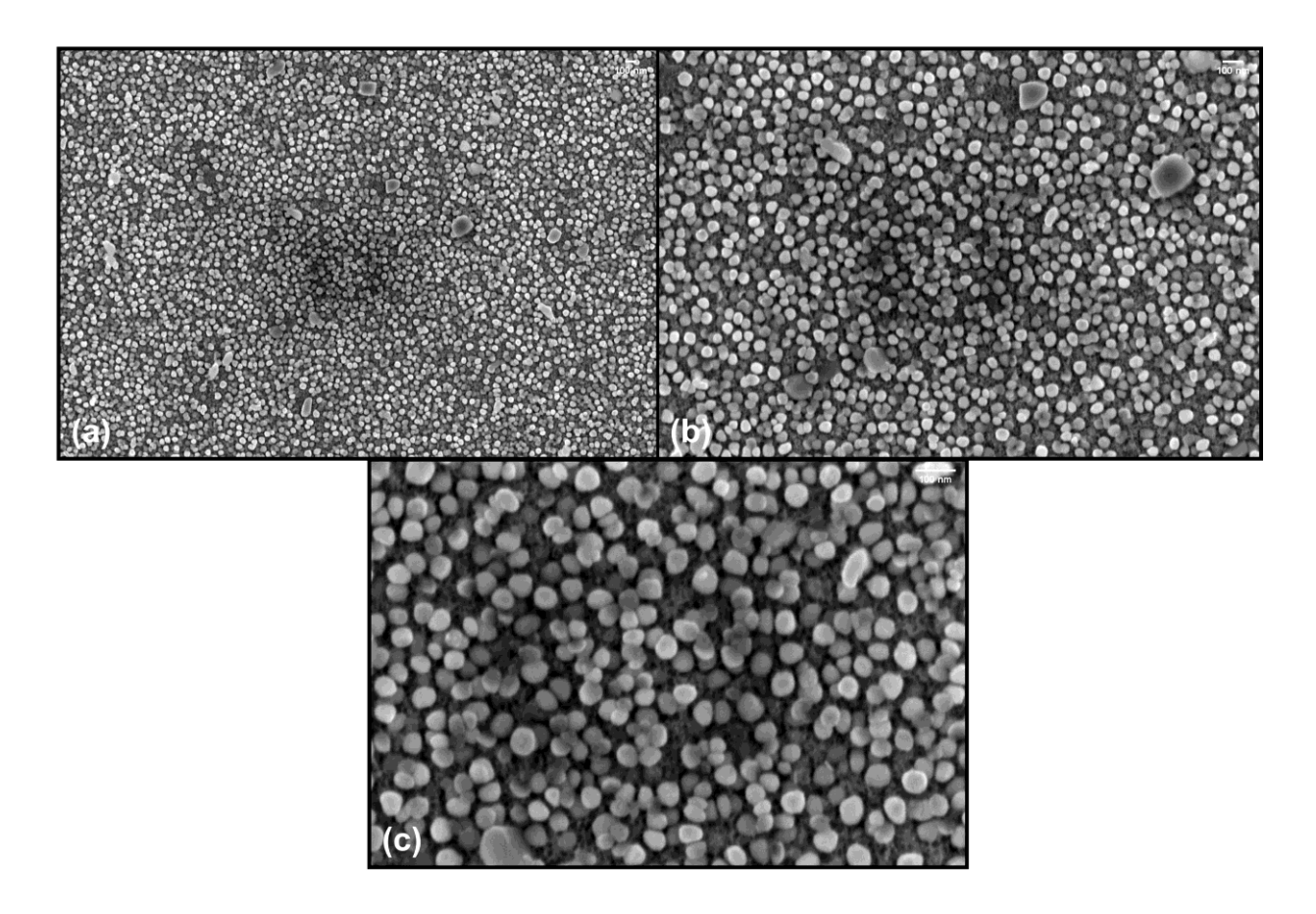


Figure 3.55. SEM image of hipped sample of IN939 at 1260°C taken with secondary electrons in XY plane (a) at 50.000x magnification in (b)100.000x magnification and (c) 200.000x magnification.

3.3.2 Sample 2: 1280 °C – 125 MPa – 240 min

The microstructural evaluation of the sample subjected to Hot Isostatic Pressing (HIP) at 1280 °C reveals an increase of grains dimension as it is possible to appreciate in *Figure 3.56*.

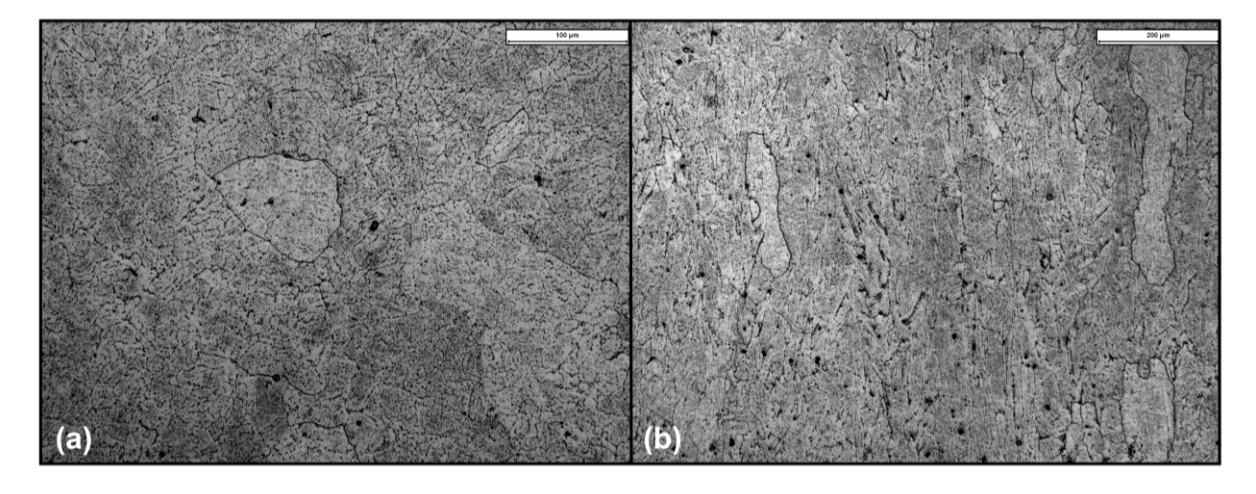


Figure 3.56. Optical Microscope image of hipped sample of IN939 at 1280°C at 200x magnification in (a) XY plane and (b) XZ plane.

Concerning carbides analysis, it is possible to notice that carbides are less present along the grain boundaries but are also randomly dispersed across the entire surface. The first type of carbides inhibit grain growth by exerting a pinning force on the grain boundaries, action probably softer in this situation. So, the sample shows the presence of different types of carbides, specifically polygonal-shaped ones associated with MC carbides and more complexly shaped ones. A visualization of them is possible in *Figure 3.57*.

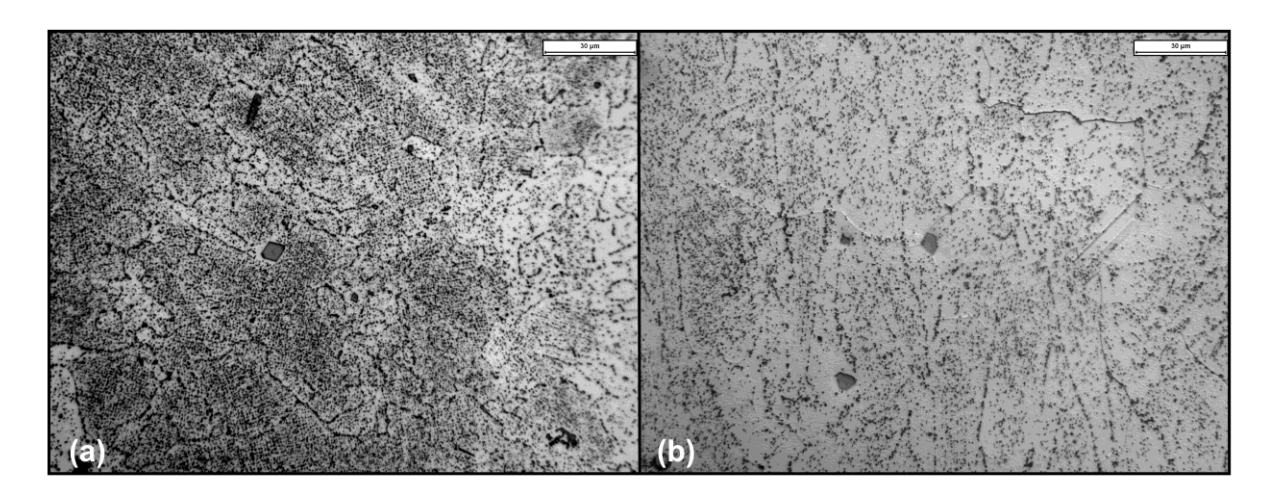


Figure 3.57. Optical Microscope image of hipped sample of IN939 at 1280°C at 500x magnification in (a) XY plane and (b) XZ plane.

A critical aspect of this microstructural investigation is the quantification of carbide dimensions, which directly influence the alloy's performance. Figure 1 reports an example of carbides morphology and dimension in sample XZ and XY planes. The image captures the characteristic morphology and dispersion of the carbides, enabling the evaluation of particle size and distribution. *Figure 3.58 (a)* reveals a carbide with a length of approximately 4 μ m. In contrast, the XZ plane view presented in *Figure 3.58 (b)* shows two notably larger carbides: one, measuring 7.7 μ m in length, is situated at a grain boundary intersection, while another, of a similar size (7 μ m), is located within the grain interior.

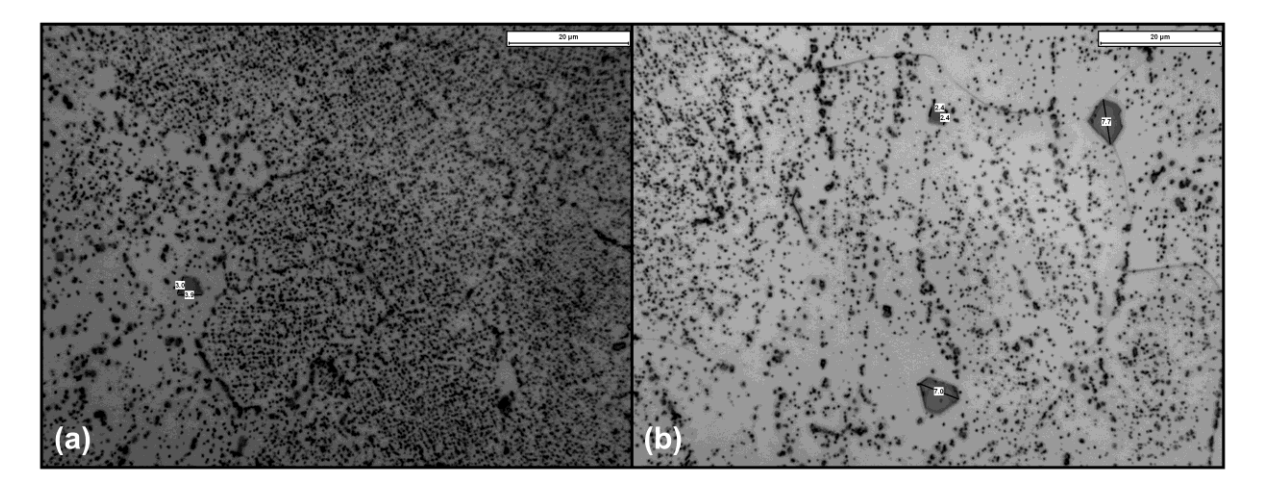


Figure 3.58. Optical Microscope image of hipped sample of IN939 at 1280°C at 1000x magnification in (a) XY plane and (b) XZ plane.

3.3.3 Sample 3: 1300 °C – 125 MPa – 240 min

The microstructural evaluation of the sample subjected to Hot Isostatic Pressing (HIP) at 1300 °C in XZ plane reveals that the sample exhibits more elongated grains than the sample heat-treated in air at an equivalent temperature. This morphological difference indicates that the HIP process inhibits normal grain growth. This effect is illustrated in *Figure 3.59*.

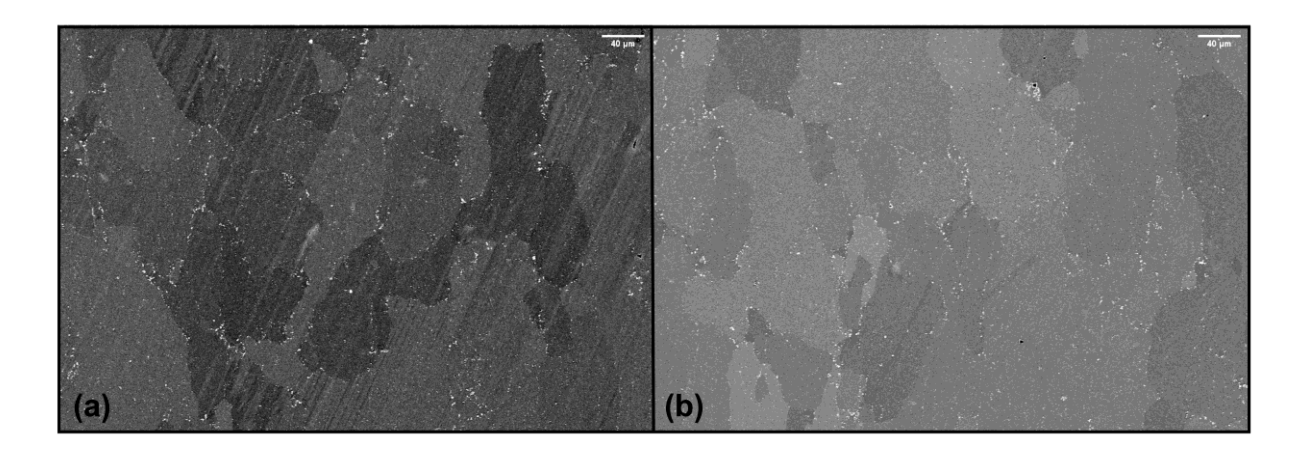


Figure 3.59. SEM image of hipped sample of IN939 at 1300°C taken with backscattered electrons in XZ plane at 500x magnification

Microstructural analysis reveals the presence of a liquid phase, although its formation is notably diminished relative to the specimen subjected to a 1300°C treatment in an air atmosphere. Two micrographs reported in Figure 3.60 (a) and (b) at different magnifications reveal the polycrystalline structure with clearly defined grain boundaries, characteristics of extensive grain growth promoted by prolonged exposure to high temperature. The grains appear equiaxed, with relatively uniform dimensions in all directions, indicating that recrystallization and diffusional processes have been effective in eliminating deformation textures or directional solidification features. At lower magnification (a), the overall microstructure is dominated by large grains, with average sizes approaching the order of hundreds of micrometers, while the higher magnification view (b) highlights the smooth and continuous grain boundaries as well as the absence of pores or cracks along them. In image (c), the equiaxed grain structure remains evident, with grain sizes consistent with the extensive coarsening already observed at lower magnification. Grain boundaries are continuous and clearly visible. The lighter zones observed at the grain boundaries indicate areas that experienced localized melting during the HIP treatment, followed by solidification on cooling. These are not simply etched grain boundaries, but evidence of liquid phase formation and redistribution of segregated elements at this temperature. These particles appear as bright or dark spots depending on imaging contrast, suggesting the presence of carbides. Image (d), at even higher magnification, provides a detailed view of the grain boundary regions. The boundaries are decorated by precipitates such as carbides that in some areas appear quite large. Within the grain interiors, a finer dispersion of secondary phases is visible, indicating that despite grain coarsening, the strengthening precipitates are retained. The elimination of porosity is also confirmed here, as no cavities or shrinkage defects are apparent.

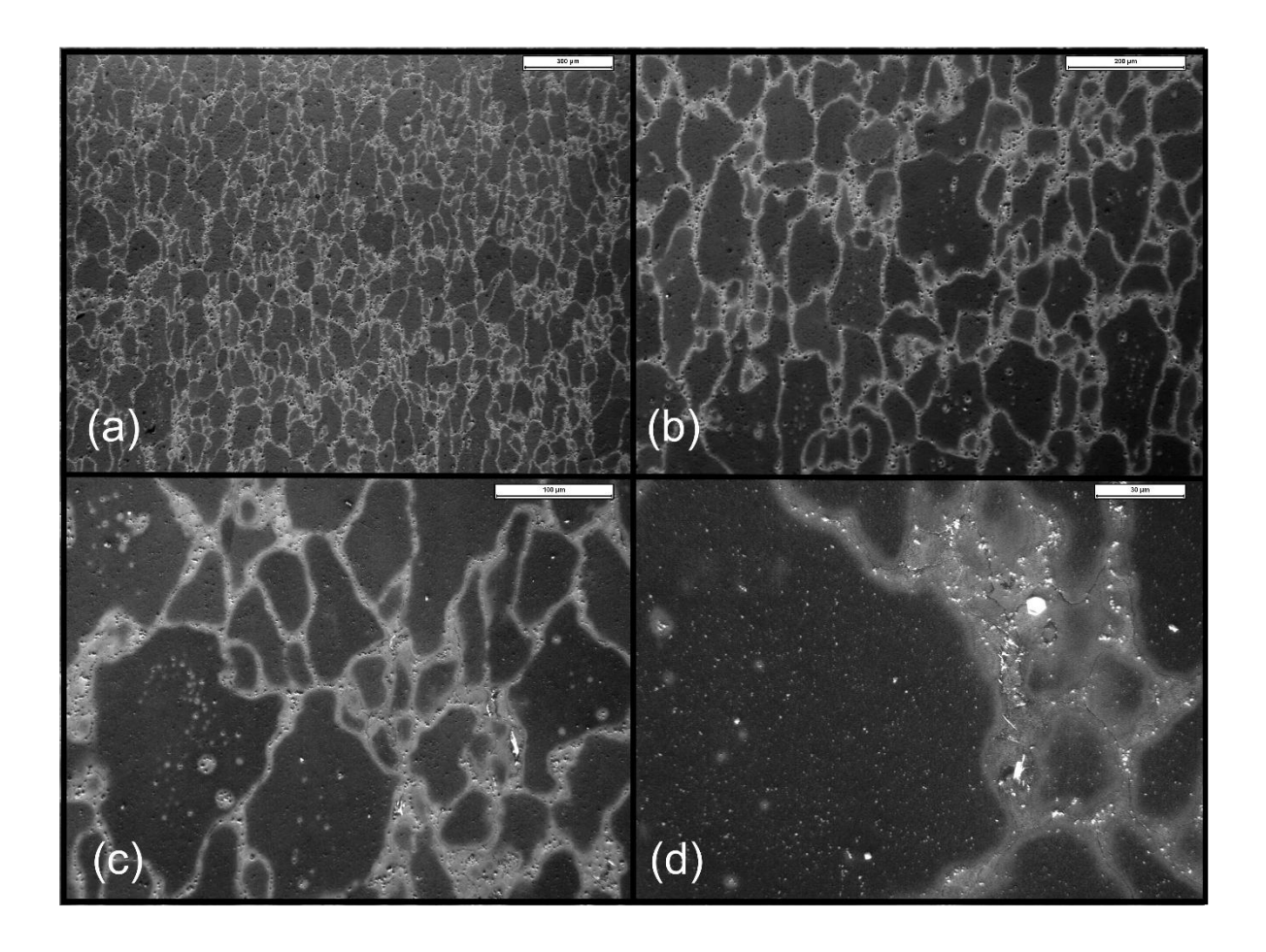


Figure 3.60. Optical Microscope image of hipped sample of IN939 at 1300°C at (a) 50x magnification, (b)100x magnification, (c) 200x magnification and (d) 500x magnification.

Figure 3.61 focuses on the grain boundary regions at higher magnification with SEM. Due to the segregation of low-melting constituents such as Ti, Ta, Nb, C, and B, incipient melting occurred at the boundaries as explained before. Upon cooling, this liquid resolidified, leaving behind networks of interdendritic phases. These resolidified regions contribute to pore healing but may embrittle the grain boundaries if present in continuous form. Figure 3.61 (a) and (b) highlight eutectic colonies located in the interdendritic regions and along grain boundaries. These colonies consist of plate-like or lamellar η phase closely associated with blocky carbides (MC or $M_{23}C_6$). Carbides frequently act as nucleation sites for η phase, explaining their co-localization. Finally, Figure 3.61 (c) and (d), captured at very high magnification, provide a close-up view of the morphology of these secondary phases. The lamellar structure of eutectic phase is visible and η phase appears as needle- or plate-like precipitates penetrating the γ matrix, while the carbides are visible as angular, bright particles embedded within or adjacent to the η plates. The background matrix also displays a fine dispersion of smaller spherical γ' precipitates. A spatial variation in the γ' phase morphology is also evident: the precipitates are finer in the regions remote from the carbides and become progressively coarser in the areas immediately surrounding them.

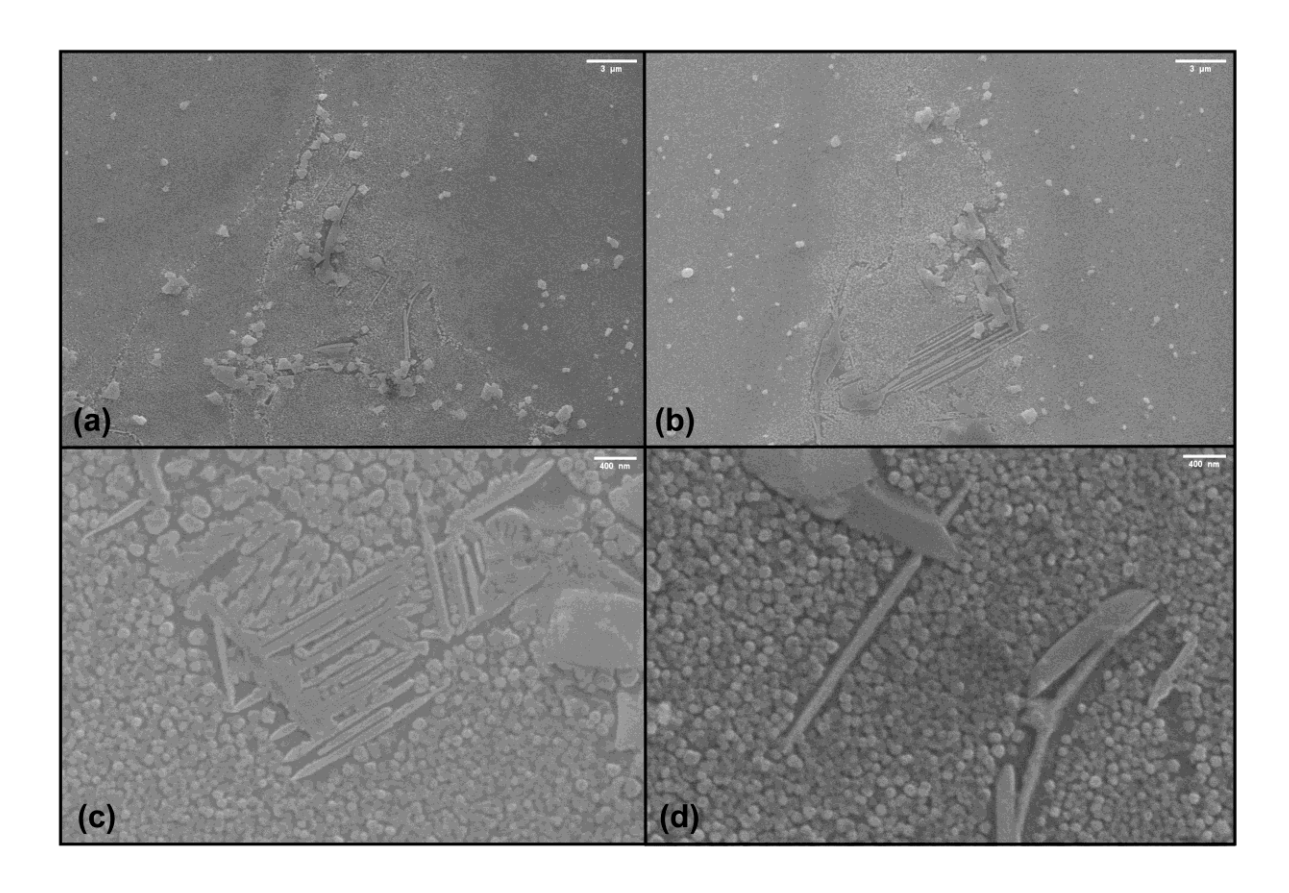


Figure 3.61. SEM image of hipped sample of IN939 at 1300°C taken with secondary electrons in XZ plane at (a, b) 8.000x magnification and (c,d) 50.000x magnification.

A visualization of grain boundary is reported in *Figure 3.62*. These high-magnification images demonstrate carbides decorating the boundaries.

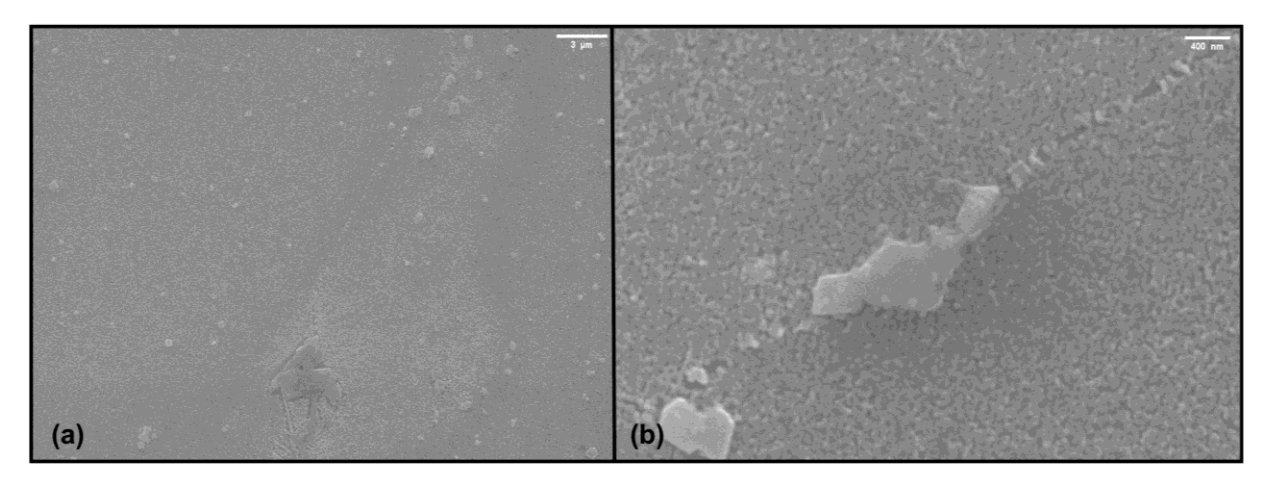


Figure 3.62. SEM image of hipped sample of IN939 at 1300°C taken with secondary electrons in XZ plane at (a) 8.000x magnification and (b) 50.000x magnification.

Higher magnification images that show the morphology and distribution of γ' within the grains are visible in *Figure 3.63*. Gamma prime phase presents its spherical shape mentioned above.

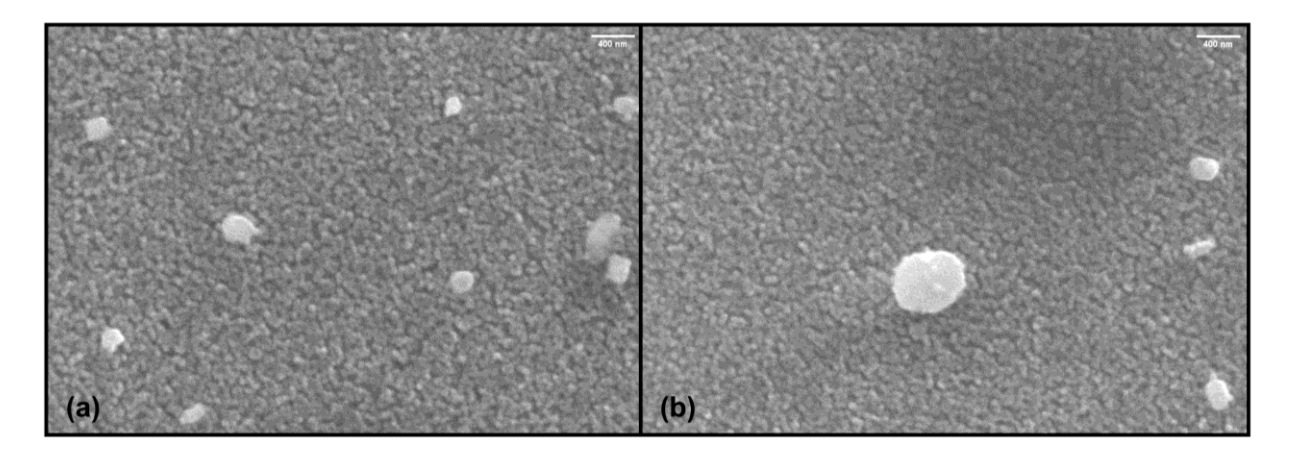


Figure 3.63. SEM image of hipped sample of IN939 at 1300°C taken with secondary electrons in XZ plane at 50.000x magnification.

In Figure 3.64 the grain boundary and carbides can be clearly distinguished. Carbides appear bright, angular particles decorating the grain boundaries. The micrographs provide dimensional information: in (a), the measured carbide is approximately 11 µm in size, while in image (b) a carbide of about 6 µm is observed. The variation in carbide size highlights the heterogeneous distribution of these particles, which may nucleate and grow to different extents depending on local chemistry and the degree of liquid phase present during HIP. The measured carbide dimensions are significant in terms of mechanical behavior: while carbides can contribute to boundary strengthening and hinder grain boundary sliding at high temperature, excessive coarsening or clustering of carbides may lead to stress concentration sites and premature crack initiation.

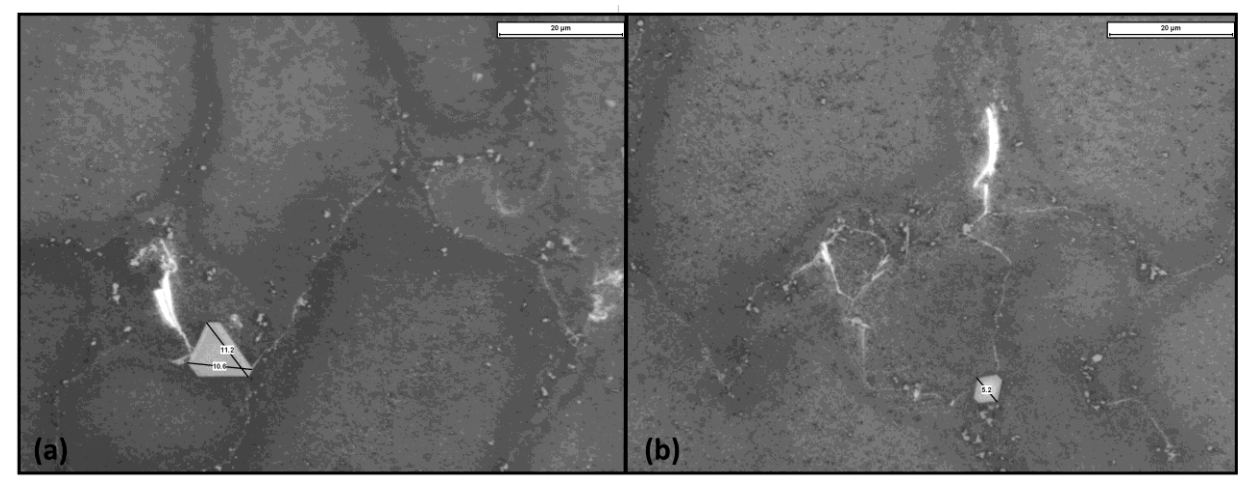


Figure 3.64. Optical Microscope image of hipped sample of IN939 at 1300°C at 500x magnification showing carbides dimensions.

CHAPTER 4

Discussion of results

The DSC of the specimen previously heat treated at 1300 °C (*Figure 4.1*) provides additional insight into the transformations occurring after exposure to such a high temperature. During heating, three distinct exothermic peaks (dotted orange circles) appear between ~700 and 900 °C, which are attributed to the precipitation or redistribution of secondary carbides, specifically M_6C and $M_{23}C_6$. The exothermic nature of these features confirms that new phases are forming. At intermediate temperatures, the curve exhibits a broad endothermic step (dotted black circle), which corresponds to the dissolution of the γ' population that had formed during cooling from the prior 1300 °C exposure. At higher temperatures, a pronounced endothermic trough is observed near ~1275–1300 °C, indicating incipient melting and the dissolution of grain-boundary constituents. On cooling, the reciprocal sharp exothermic peak confirms the resolidification of these phases, while further exothermic changes at lower temperatures reflect the re-nucleation and growth of γ' . Overall, the sequence highlights that heat treatment at 1300 °C drives the system close to the solidus, where liquation phenomena, carbide redistribution, and γ' instability strongly interact to shape the microstructural evolution.

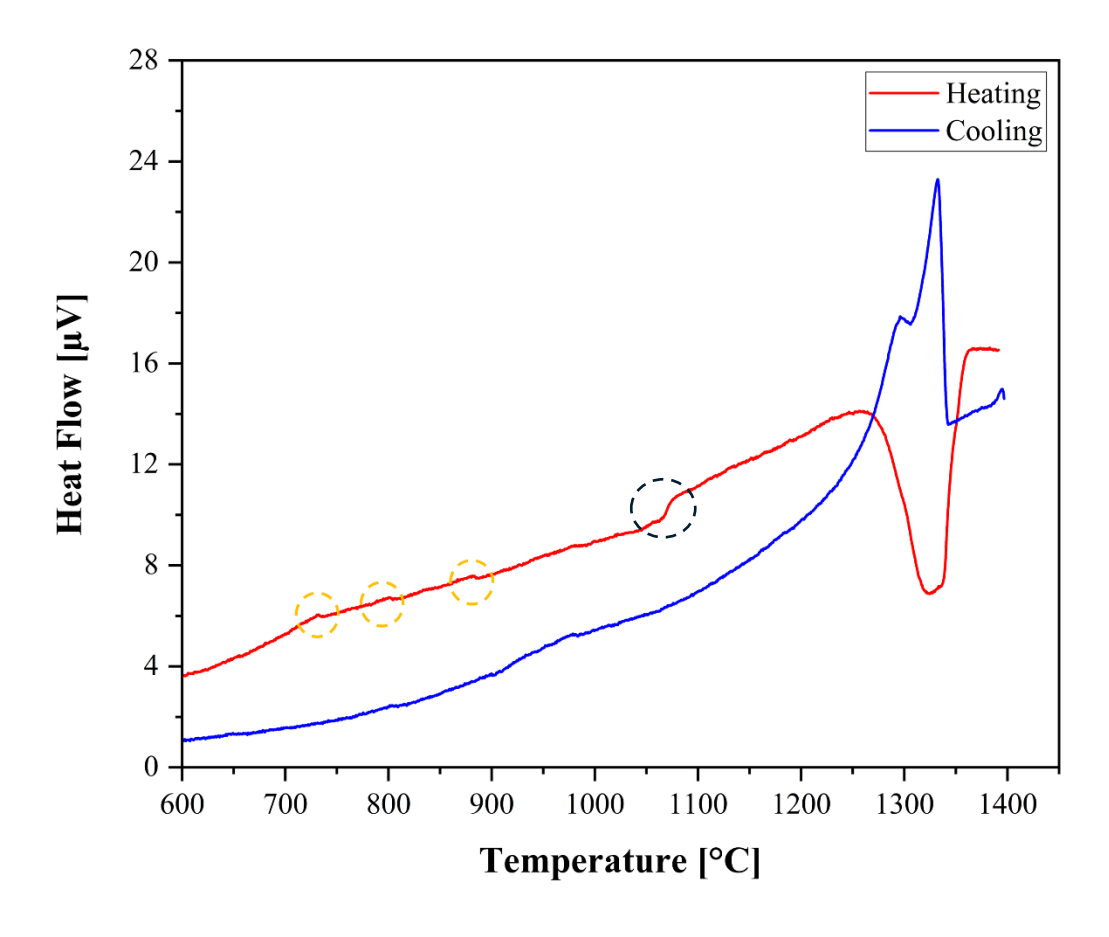


Figure 4.1. DSC cooling and heating curves for sample heat treated at 1300°C.

The comparison between this DSC response and that of the as-built condition provides a coherent basis for interpreting the grain-size evolution observed across the furnace and HIP treatments. In both cases, the heating curves highlight the critical thermal window between ~1275 and 1310 °C, where incipient melting of boundary constituents occurs. This region is particularly relevant for the samples treated at 1300 °C, since re-solidification of the liquid films formed at grain boundaries introduces additional phases that pin or subdivide grains during cooling. The effect is evident in the grain-size measurements: in air, the average grain size increases steadily from 1250 to 1270 °C, peaks at 1280-1290 °C, and then decreases slightly at 1300 °C. The modest reduction at the highest temperature is consistent with the DSC evidence, which demonstrates that liquation and re-solidification processes hinder uniform coarsening and promote heterogeneity. In contrast, HIP samples follow a similar overall trend, with maximum grain size at 1280 °C and a smaller decrease at 1300 °C, but the absolute values are larger and the distributions narrower. The pressure applied during HIP not only eliminates porosity but also suppresses extensive grain-boundary liquation, allowing recrystallization and boundary migration to proceed more uniformly. As a result, HIP promotes the development of coarse, equiaxed, and homogeneous grains even at 1300 °C, whereas air treatments at the same temperature lead to a more heterogeneous and partially pinned structure. Taken together, these results show that the grain-size bar charts and DSC curves are fully consistent. The thermal analysis identifies the solidus-adjacent window where liquation occurs, while the grain-size measurements confirm its microstructural consequences under different processing atmospheres. These findings provide the necessary foundation for the Electron Backscatter Diffraction (EBSD) observations and nanoindentation maps, which further elucidate the crystallographic and mechanical implications of the treatments at 1300 °C. Indeed, EBSD analysis was carried out to evaluate the effect of air and HIP (125 MPa) treatments at 1300 °C on the recrystallization and grain morphology of LPBF-processed IN939. EBSD maps reported in Figure 4.2 provide an overview of the recrystallized structure across a wider field of view. In the HIP-treated sample (a), the grains appear equiaxed and homogeneously distributed, with only minor orientation variations and no evidence of abnormal grain growth. The uniform blue color dominating the map reflects the prevalence of <001> orientations, but scattered grains with other orientations are also present, indicating a random orientation distribution. In the airtreated sample (b), the microstructure is markedly more heterogeneous. Orientation clustering is more pronounced, with regions of green, yellow, and red grains forming patches across the map. Grain sizes are also more variable, with fine grains adjacent to abnormally coarse ones. This heterogeneity reflects the combined effects of incipient melting, precipitation of η-phase and carbides, and incomplete recrystallization, which locally stabilize certain boundaries while allowing uncontrolled growth elsewhere.

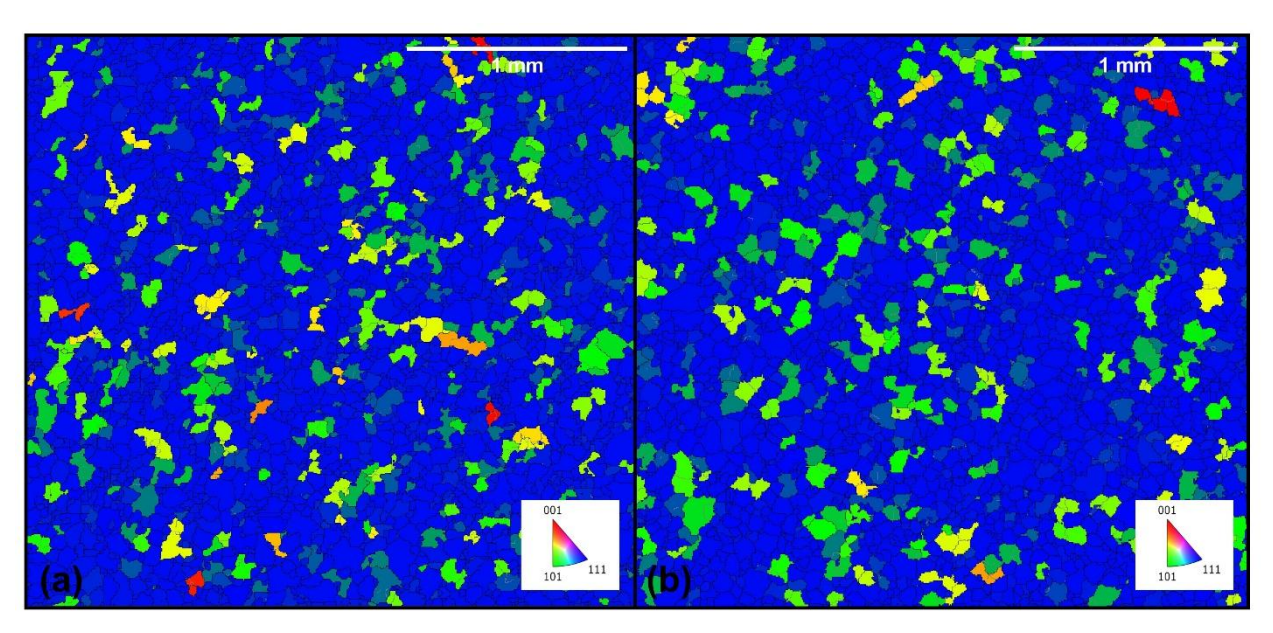


Figure 4.2. Inverse pole figure (IPF-Z) map of IN939 samples treated by (a) HIP and in (b) air.

Inverse Pole Figure (IPF) maps were acquired along the X, Y, and Z directions, together with higher-magnification images, to characterize grain size, morphology, and crystallographic orientation distribution. The comparison between the two conditions highlights the different mechanisms of grain growth and boundary stabilization occurring during high-temperature exposure. The IPF maps along the X-axis (*Figure 4.3*) show that both HIP- and air-treated samples achieved a fully recrystallized microstructure with equiaxed grains and random orientation distribution, confirming the absence of a strong crystallographic texture. In the HIP-treated sample, the grain population is slightly coarser but highly uniform, with minimal orientation clustering. In contrast, the air-treated condition reveals a more heterogeneous structure: fine grains coexist with coarser ones, generating a bimodal distribution. Local orientation clustering is also visible, consistent with pinning by carbides and η -phase at grain boundaries.

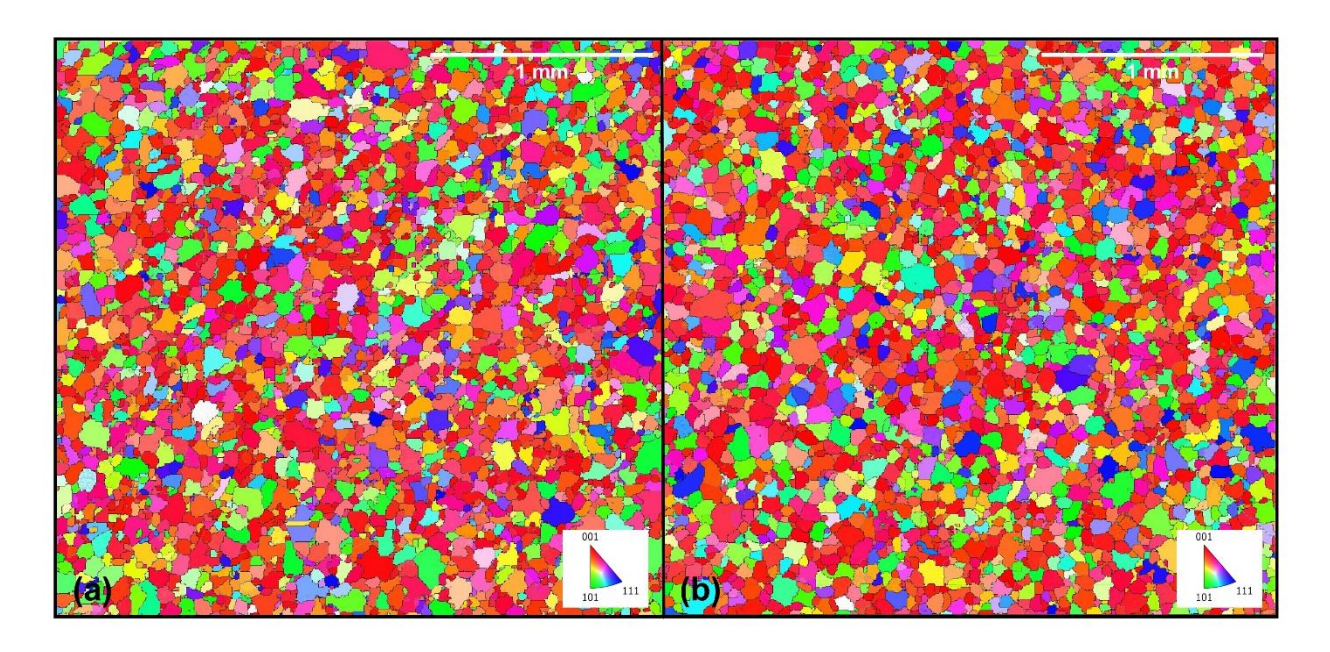


Figure 4.3. Inverse pole figure (IPF-X) map of IN939 samples treated by (a) HIP and in (b) air.

In the Y-axis maps (*Figure 4.4*), the HIP-treated condition again demonstrates a homogeneous distribution of equiaxed grains, with clean boundaries and a narrow grain-size spread. This uniformity indicates efficient recrystallization assisted by the applied pressure. Conversely, the air-treated condition shows irregular grain morphology, including several fine grains together with larger ones. This unevenness is attributed to the formation of secondary phases at grain boundaries, which locally hinder boundary migration and promote the development of smaller recrystallized grains adjacent to coarse ones.

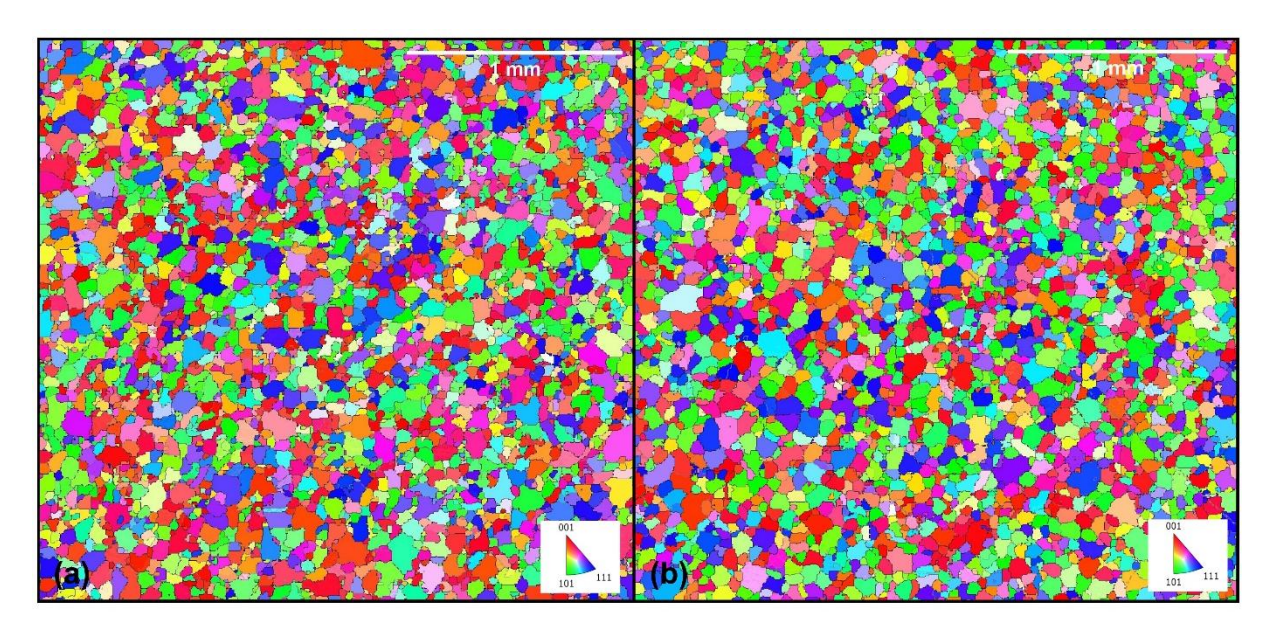


Figure 4.4. Inverse pole figure (IPF-Y) map of IN939 samples treated by (a) HIP and in (b) air.

The Z-axis orientation maps (*Figure 4.5*) confirm the same general trends observed in X and Y. The HIP sample exhibits a highly consistent equiaxed grain structure, with grains distributed within a narrow size range and lacking abnormally coarse grains. The air sample, however, contains a broader distribution of grain sizes and clusters of grains with similar orientations, suggesting heterogeneous recrystallization. These features reflect the role of incipient melting and boundary segregation in air treatments, which destabilize uniform grain growth.

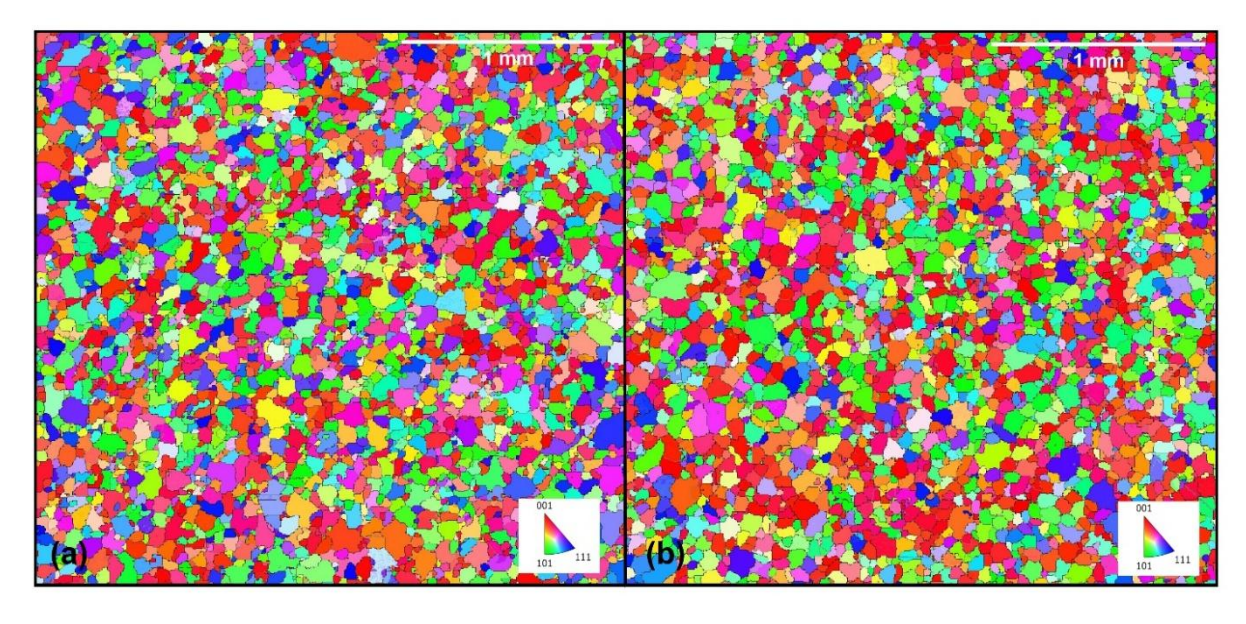


Figure 4.5. Inverse pole figure (IPF-Z) map of IN939 samples treated by (a) HIP and in (b) air.

Higher-magnification EBSD maps (*Figure 4.6*) further emphasize the differences between the two treatments. In the HIP-treated condition (a), the grains are predominantly in the 35–45 μ m range, with smooth boundaries and no evidence of abnormal fine grains. By contrast, the air-treated condition shows a bimodal grain population: clusters of fine recrystallized grains are observed together with larger grains. While these smaller features might initially resemble carbides, EBSD indexing confirms that they correspond to fine γ matrix grains or annealing twins. The presence of these small grains highlights the impact of secondary phases in subdividing or pinning grains during the air treatment.

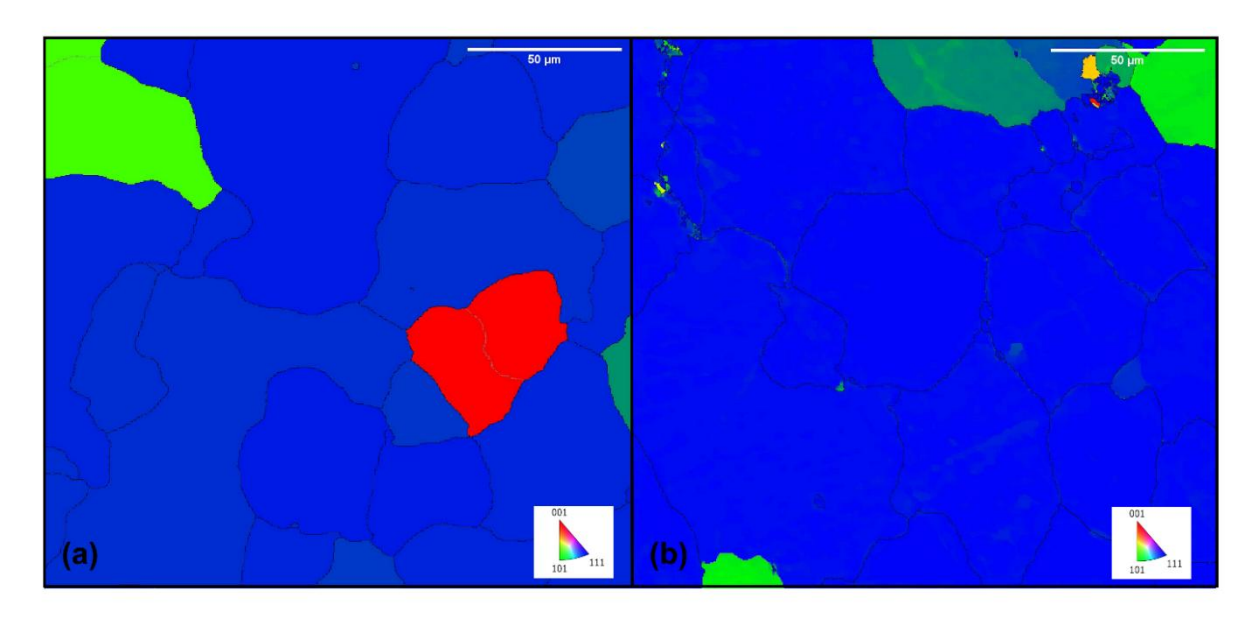


Figure 4.6. Higher magnification inverse pole figure (IPF-Z) map of IN939 samples treated by (a) HIP and in (b) air.

EBSD analysis across multiple scales demonstrates that HIP treatment at 1300 °C promotes a homogeneous recrystallized microstructure, with equiaxed grains, narrow size distribution, and random orientations. By contrast, air treatment leads to a heterogeneous structure, characterized by bimodal grain size, orientation clusters, and evidence of grain-boundary pinning and subdivision caused by secondary phases. These differences are consistent across X, Y, and Z directions, at both large and small scales. The observed uniformity in HIP samples explains their more consistent mechanical response in nanoindentation, while the heterogeneity of air-treated samples accounts for the broader hardness scatter.

To complement the crystallographic and microstructural characterization obtained from EBSD, nanoindentation testing was performed in order to evaluate the local mechanical response of IN939 after treatment at 1300 °C in air and HIP conditions. A 13x13 indent grid was applied over the sample surface, providing 169 measurements of hardness per condition. This approach allows not only the determination of average hardness values, but also the visualization of spatial variations across the surface, which can be directly correlated with the microstructural features identified by EBSD, such as grain size distribution, boundary morphology, and the presence of secondary phases. By combining EBSD with nanoindentation mapping, it becomes possible to link microstructural homogeneity or heterogeneity with mechanical uniformity, thereby clarifying the influence of the processing route on local mechanical performance. The visualization of the indenter prints in both samples is reported in *Figure 4.7* and *Figure 4.8*.

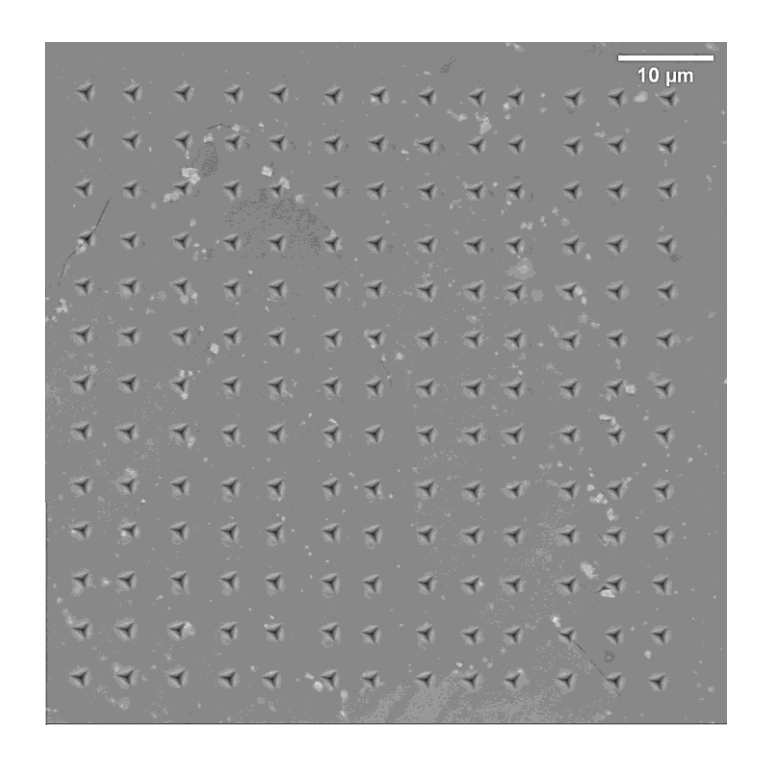


Figure 4.7. Nano Hardness grid of sample HIPped.

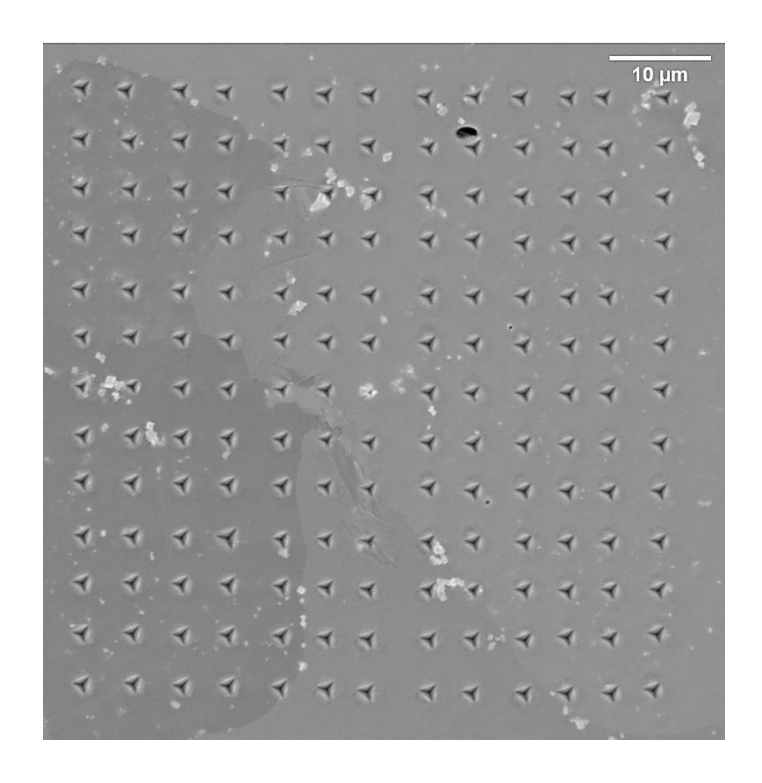


Figure 4.8. Nano Hardness grid of sample heat-treated in air.

Several parallel nanoindentation profiles were repeated in order to improve standard deviation and significance of the measurements. A statistical analysis was carried out to determine if there is a statistically significant difference in the nanoindentation hardness between the two differently processed samples: one treated in air (denoted as AIR) and one treated via Hot Isostatic Pressing (denoted as HIP). A robust statistical methodology was applied to ascertain whether the observed

differences in central tendency are statistically meaningful or attributable to random variation. Preliminary analysis provides measures of central tendency and dispersion, summarizing the data distribution for each group as reported in *Table 4.1*.

Table 4.1 Statistics of hardness	Table 4	1.1 S	Statistics	of l	hardness
----------------------------------	---------	-------	------------	------	----------

Sample	Mean	St.Dev.	Minimum	Median	Maximum
AIR	8.11	1.66	4.75	7.9	27
HIP	7.87	0.58	5.68	7.81	10.25

Prior to inferential analysis, the data are tested for conformity to the assumptions of parametric tests. An Anderson-Darling test for normality is conducted on each sample. Both samples significantly deviate from a normal distribution (p < 0.005), violating a key assumption for parametric testing. The results are shown in *Figure 4.9*.

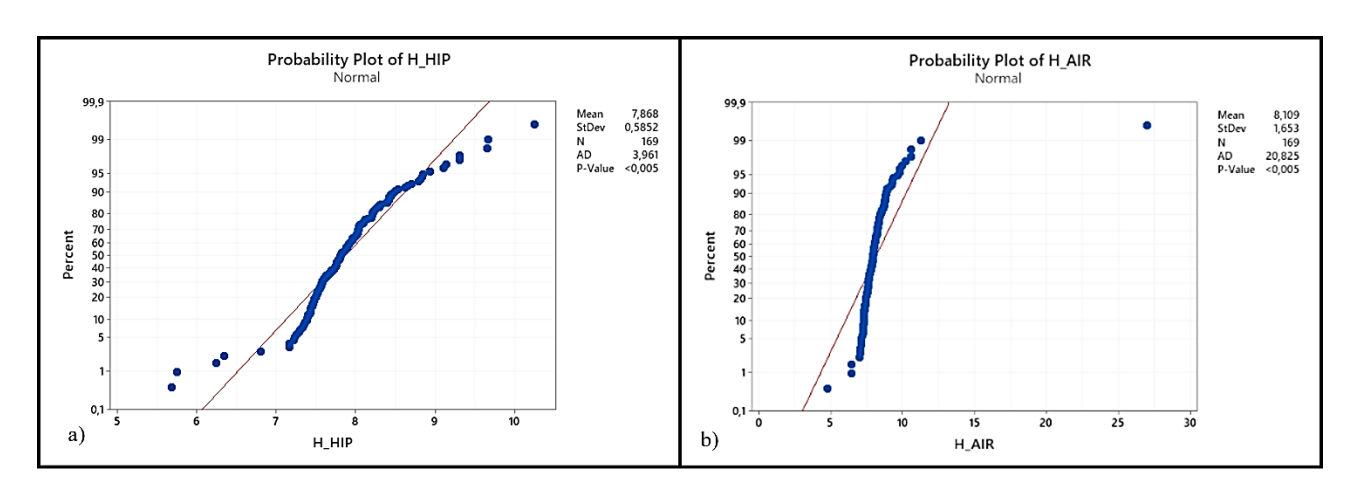


Figure 4.9. Hardness normal probability of a) HIPped sample and b) air treated sample.

Due to the non-normal distribution of the data, a non-parametric Mann-Whitney U test is selected to compare the medians of the two groups. This test is distribution-free and robust against violations of normality. The test is conducted at a 95% confidence level ($\alpha = 0.05$). The hypotheses defined are reported in *Table 4.2* and the parameters involved are shown in *Table 4.3*.

Table 4.2. Hypotheses of Mann-Whitney U test.

Null hypothesis	H ₀ : $\eta_1 - \eta_2 = 0$
Alternative	H ₁ : $\eta_1 - \eta_2 \neq 0$
hypothesis	

Table 4.3. Statistics.

η ₁ : median of Sample_AIR
η ₂ : median of Sample_HIP
Difference: η ₁ - η ₂

The data summary reveals similar central values with a slight difference in variability (*Table 4.4*).

Table 4.4. Descriptive statistics.

Sample	N	Median
AIR	169	7,90
HIP	169	7,81

The Mann-Whitney U test yielded a p-value of 0.203. As this value exceeds the significance level of $\alpha=0.05$, the null hypothesis (H₀) cannot be rejected. The test estimated the difference in median hardness between the AIR and HIP samples to be 0.07 GPa. However, the 95% confidence interval for this difference ranged from -0.04 GPa to 0.19 GPa. Since this interval includes zero, it indicates that the observed difference is not statistically significant at the $\alpha=0.05$ level. Based on the statistical evidence, it is possible to conclude that there is no statistically significant difference in the median nanoindentation hardness between the material processed in air and the material processed via Hot Isostatic Pressing. The extremely high p-value (p = 0.203) indicates that the minute observed difference in median values is highly likely to be due to random chance rather than a systematic effect of the processing method. Therefore, for the property of hardness measured via nanoindentation, the two processing techniques can be considered equivalent. A comparative boxplot (*Figure 4.10*) visually reinforces the statistical findings. The boxes, representing the interquartile ranges, show considerable overlap. The medians of both groups are contained within the other group's quartile range, providing clear visual confirmation of the lack of a significant difference.

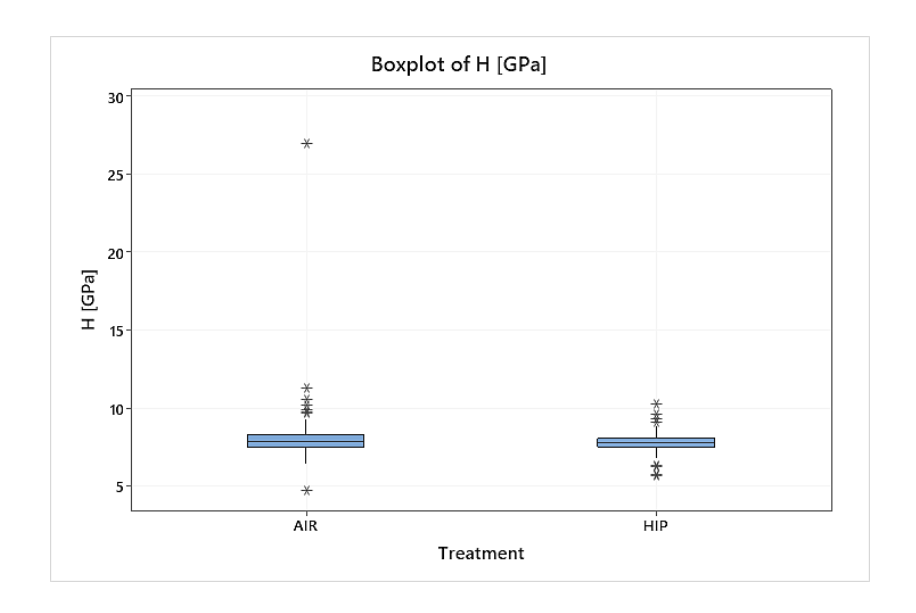


Figure 4.10 Box plot of nanoindentation hardness.

A histogram with overlaid normal distribution curves was generated to provide a detailed visual assessment of the hardness data distribution for both sample groups (Figure 4.11). This analysis offers further insight beyond the boxplot, illustrating the frequency and shape of the data distributions. While the Mann-Whitney test correctly concluded that the difference in the median hardness is not statistically significant, this histogram elucidates a fundamental difference in the nature of the two distributions. The HIP process produces a more predictable and uniform material property, as evidenced by its low variability. Conversely, the AIR process results in a broader range of hardness values, including a number of high outliers, suggesting potential inconsistencies or localized variations in the material's response to treatment.

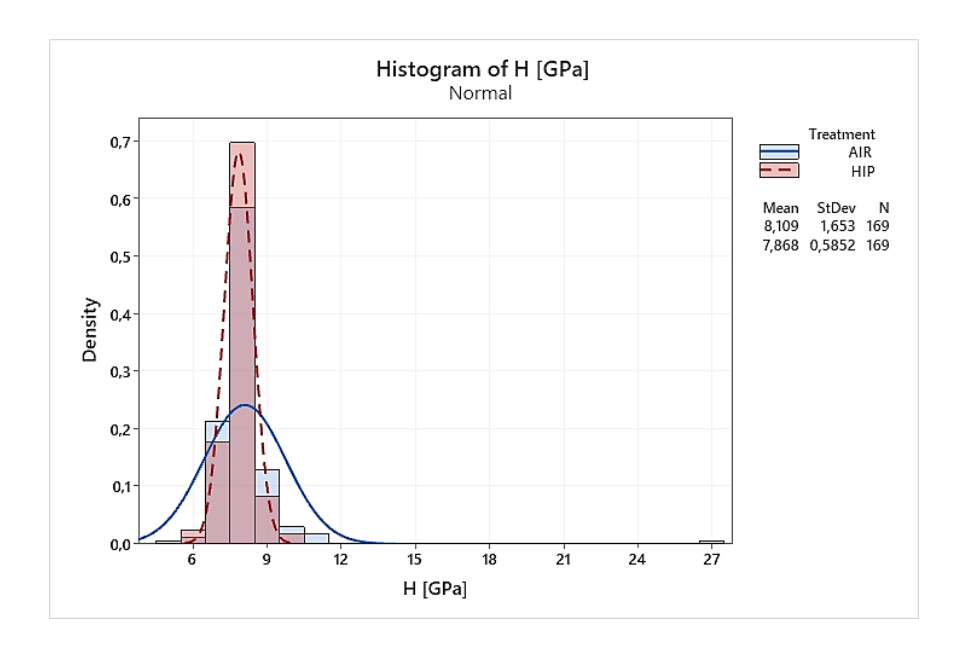


Figure 4.11. Histogram of hardness values for AIR and HIP samples, showing their differing distributions.

Further analysis was conducted to correlate the hardness values with specific microstructural features. A hardness contour plot was generated to visualize the spatial distribution of values across the sample surface and to identify any localized areas of high hardness. The plots are reported in *Figure 4.12* and *Figure 4.13*.

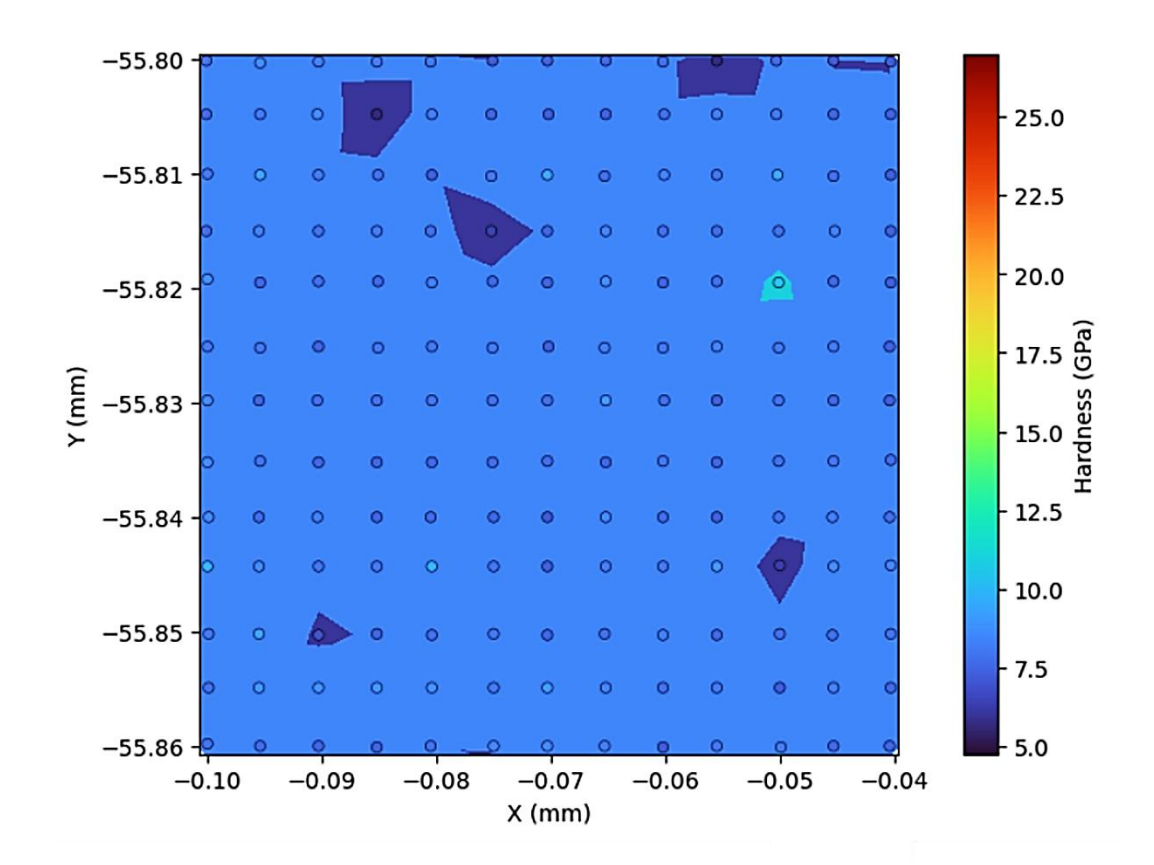


Figure 4.12. Contour plot of sample HIPped.

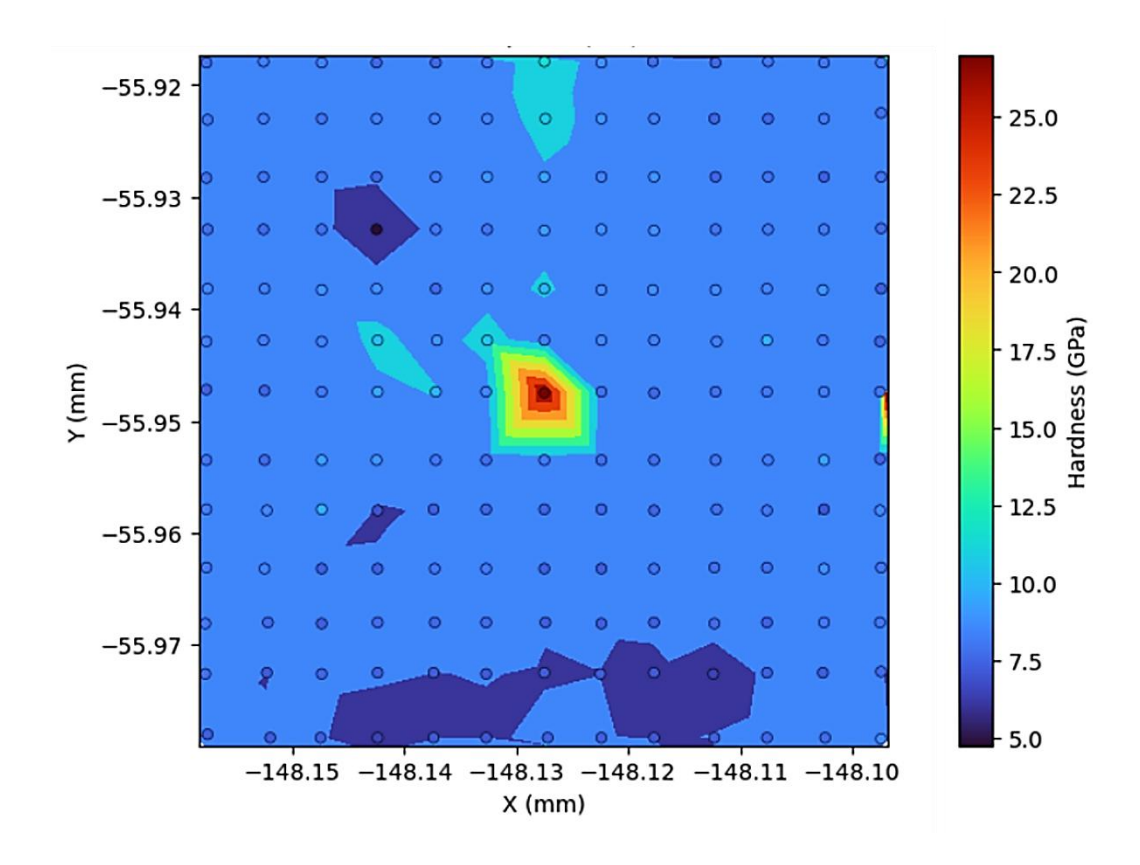


Figure 4.13. Contour plot of sample heat-treated in air.

The hardness map of the air-treated sample (Sample AIR) reveals a generally homogeneous distribution of values within the range of 6-8 GPa. However, a pronounced localized anomaly is observed, where hardness exceeds 25 GPa, reaching a maximum of 27 GPa. This hotspot manifests in the contour map (Figure 4.13) as a sharply bounded region of bright yellow, surrounded by a rhomboidal pattern arising from the interpolation between the extreme high point and neighboring lower values. The geometric appearance of this feature is not itself physical, but rather an artifact of the plotting method that emphasizes the contrast between one markedly different point and its surroundings. Overlapping the grid of nano indentations with the SEM image it appears that the maximum value of hardness falls exactly on a large single carbide, presumably TiC. In addition, the analysis reveals that the secondary phases, partucularly those associated with the eutectic phase and the n phase, do not exhibit hardness values significantly divergent from the average. Instead, their measured hardness values fell within the central distribution of the overall dataset. In contrast, the HIP-treated sample (Sample HIP) in Figure 4.12 displays a far more uniform contour map, with hardness values consistently distributed between 6 and 9 GPa and no evidence of extreme anomalies. The absence of isolated hotspots and the reduced variability may be indicative of microstructural homogenization and porosity elimination commonly associated with HIP processing.

Combining the EBSD analysis and the nano indentation it is possible to declare that the HIP-treated sample shows a tighter hardness distribution, with values clustered in a narrower range and smooth spatial variation across the 13×13 indent grid. This uniformity mirrors the EBSD evidence of consistent grain size and clean grain boundaries. In contrast, the air-treated sample exhibits a wider hardness scatter, with localized regions of both high and low values. The presence of small grains in certain regions contributes to local hardening, while coarser grains and boundary films enriched with eutectic and carbide phases act as mechanically softer or more heterogeneous zones.

The combined EBSD and nanoindentation analyses clearly demonstrate the different effects of air furnace and HIP treatments at 1300 °C on the microstructural and mechanical response of LPBFprocessed IN939. EBSD revealed that the HIP condition produced a fully recrystallized, equiaxed, and homogeneous microstructure, with an average grain size of ~ 80-90 µm and a narrow distribution across all orientations (X, Y, and Z). In contrast, the air-treated condition underwent recrystallization in a heterogeneous manner, characterized by a bimodal grain size distribution, clusters of similarly oriented grains, and grain boundary pinning by η-phase and carbides. The presence of resolidified films at grain boundaries further confirmed that incipient melting occurred under air treatment, limiting uniform grain growth. These microstructural differences were directly reflected in the nanoindentation maps. The HIP-treated sample exhibited a narrow hardness range and smooth spatial variation, consistent with its homogeneous grain structure and clean grain boundaries. Conversely, the air-treated sample displayed a broader hardness distribution, including localized hard and soft regions that correlate with the coexistence of fine and coarse grains, as well as with secondary-phase decorated boundaries. Overall, HIP at 1300 °C ensures a more reliable microstructure-property relationship, combining porosity elimination, uniform recrystallization, and consistent mechanical response, despite the drawback of grain coarsening. In contrast, air treatment at the same temperature leads to heterogeneous recrystallization and variable hardness. These findings highlight the advantages of HIP over conventional furnace treatment for stabilizing the microstructure of LPBF IN939, especially when mechanical uniformity and long-term high-temperature performance are critical.

CHAPTER 5

Conclusion

This work presented a comprehensive study of the microstructural and mechanical evolution of LPBF-processed IN939 in the as-built condition, after furnace heat treatments between 1250 and 1300 °C, and after HIP at 1260, 1280, and 1300 °C (125 MPa, 240 min). A multi-technique approach combining DSC, grain-size analysis, SEM/EDS, EBSD, and nanoindentation was employed to characterize the transformations occurring under different processing routes and to correlate thermal history with microstructural stability and mechanical performance.

The DSC analysis provided the thermal framework for interpreting the observed microstructures. In the as-built state, the alloy exhibited multiple sub-900 °C endothermic shoulders corresponding to the staged dissolution of γ' precipitates, confirming the high metastability of the LPBF microstructure. At higher temperatures, a pronounced endothermic signal near 1275-1310 °C indicated the onset of incipient melting, identifying a narrow critical window where grain boundary instability occurs. After a 1300 °C exposure, the DSC response changed significantly: the heating branch displayed exothermic peaks between ~700 and 900 °C, consistent with the precipitation and redistribution of carbides (M₆C and M₂₃C₆), followed by a broad endothermic step corresponding to the dissolution of the γ' populations formed during cooling from the super-solvus. A sharp endothermic trough again appeared near the solidus, confirming the persistence of liquation phenomena at grain boundaries. On cooling, the reciprocal exothermic effects marked resolidification and renewed γ' nucleation. These results confirmed that thermal treatments close to 1300 °C not only influence grain growth but also promote phase redistribution at grain boundaries, directly affecting microstructural stability. Grain growth was gradual between 1250°C and 1270 °C, peaked at 1280-1290 °C, and decreased slightly at 1300 °C. This non-monotonic behavior is explained by the DSC results: when the solidus is approached, liquation occurs, and resolidified films and carbides act as pinning sites, restricting uniform coarsening and producing heterogeneous grain distributions. HIP samples followed a similar trend but consistently exhibited larger grain sizes and narrower distributions. The applied pressure not only suppressed extensive grain-boundary liquation but also minimized the expansion of any liquid that did form, thereby reducing segregation and limiting the development of resolidified boundary films. At the same time, HIP eliminated porosity and promoted continuous recrystallization, leading to coarser yet more uniform microstructures than those observed in air.

Detailed microstructural analysis of the 1300 °C condition revealed the strongest divergence between air and HIP treatments. SEM and EDS showed that the air-treated sample contained resolidified films, η-phase lamellae, and carbides enriched in Ti, Ta, Nb, and W along grain boundaries, consistent with liquation and segregation during cooling. Microcracks and dendritic features further confirmed instability of the boundary network. In contrast, the HIP-treated sample exhibited clean equiaxed grains, reduced segregation, and a more homogeneous distribution of carbides, demonstrating the stabilizing effect of pressure against liquation.

EBSD analysis reinforced these observations. The HIP sample displayed a fully recrystallized, equiaxed microstructure with a narrow grain-size distribution and random orientations across X, Y, and Z directions, confirming homogeneous recrystallization. The air-treated condition, however,

was characterized by bimodal grain size distributions, orientation clustering, and evidence of boundary pinning by η -phase and carbides. High-magnification EBSD confirmed the presence of fine recrystallized grains adjacent to larger ones, highlighting the heterogeneous nature of recrystallization in air.

Nanoindentation directly connected these microstructural differences to mechanical response. The HIP-treated sample showed hardness values consistently between 6 and 9 GPa, with smooth spatial variation across the 13×13 grid, reflecting its homogeneous grain structure and clean grain boundaries. In the air-treated sample, hardness values averaged 6–8 GPa but exhibited a much broader scatter, including an extreme anomaly of 27 GPa traced to indentation on a large TiC carbide.

Overall, these results highlight the decisive influence of processing route on the stability of LPBF IN939 near the solidus. Furnace treatments in air promote recrystallization and grain growth but are accompanied by liquation, boundary segregation, and heterogeneous microstructures, leading to variable hardness and local anomalies. HIP, in contrast, achieves porosity elimination, suppresses liquation, and minimizes the expansion of any liquid phase, thereby limiting segregation and promoting uniform recrystallization. The strong convergence of evidence from DSC, grain-size analysis, SEM/EDS, EBSD, and nanoindentation demonstrates that HIP at 1300 °C provides a superior balance between microstructural homogeneity and mechanical reliability.

This study therefore establishes a clear framework for selecting thermal post-treatments of LPBF IN939. While furnace treatments in air can be effective at lower temperatures, they risk instability when approaching the solidus. HIP, by contrast, ensures structural consistency and mechanical uniformity, making it the preferred route for high-temperature applications where reliability is critical.

ACKNOWLEDGEMENTS

You are my foundation. Every win is built upon you.

Thanks to

my mother Patrizia,

my father Stefano,

my sister Francesca,

my grandfather Settimio.

Thanks also to my supervisor, Prof. Emilio Bassini, for his belief in me.

BIBLIOGRAPHY

- [1] Matthew J. Donachie, Stephen J. Donachie "Superalloys: A Technical Guide", 2nd Edition, The Materials Information Society.
- [2] J. Donachie Matthew and J. Donachie Stephen, "Understanding Superalloy Metallurgy," in Superalloys: A Technical Guide, ASM International,2002.doi: 10.31399/asm.tb.stg2.t61280025.
- [3] Geddes B., Leon H., and Huang X., "*Phases and microstructure of superalloys*," in Superalloys: Alloying and performance, 2010, pp.25–57.doi: https://doi.org/10.31399/asm.tb.sap.9781627083133.
- [4] Minet Kevin, Ankit Saharan, Anja Loesser, and Niko Raitanen. "Superalloys, Powders, Process Monitoring in Additive Manufacturing." In Additive Manufacturing for the Aerospace Industry, 163–85. Elsevier, 2019. https://doi.org/10.1016/B978-0-12-814062-8.00009-1.
- [5] Lee, J. A. (2012). Hydrogen embrittlement of nickel, cobalt and iron-based superalloys. In R. P. Gangloff & B. P. Somerday (Eds.), Gaseous hydrogen embrittlement of materials in energy technologies: The problem, its characterisation and effects on particular alloy classes (Vol. 2, pp. 624-667). Woodhead Publishing. https://doi.org/10.1533/9780857093899.3.624
- [6] Reed, R.C., 2006, "The Superalloys-Fundamentals and Applications," Cambridge University Press, Cambridge, ISBN-13 978-0-511-24546-6
- [7] Wang, D., Ornano, F., Li, Y. S., Wells, R., Hjalmarsson, C., Hedlund, L., & Povey, T. (2016, June 13-17). *FLOvane: a new approach for HP vane design*. ASME Turbo Expo 2016: Turbomachinery Technical Conference and Exposition, Seoul, South Korea. GT2016-57285.
- [8] Committee on the United States Air Force's Aerospace Propulsion Needs, National Research Council. (2006). *A Review of United States Air Force and Department of Defense Aerospace Propulsion Needs*. The National Academies Press. https://doi.org/10.17226/11780
- [9] As a Martinsson. Ageing influence on nickel-based superalloys at intermediate temperatures (400-600°C). 2006.
- [10] H. K. D. H. Bhadeshia. *Nickel Based Superalloys*. University of Cambridge. https://www.phase-trans.msm.cam.ac.uk/2003/Superalloys/superalloys.html
- [11] Sims, C.T., Stoloff, N.S., Hagel, W.C., (1987). Superalloys II. New York: Wiley-Interscience.
- [12] Chapman, L.A., (2004). Application of high temperature DSC technique to nickel based superalloys. J. Mat. Sci., 39, (24) 7229—7236.
- [13] Davis, J.R., (1997). Heat Resistant Materials. Materials Park: ASM International?

- [14] G. Liu, X. Xiao, M. Véron, and S. Birosca, "The nucleation and growth of η phase in nickel-based superalloy during long-term thermal exposure," Acta Mater, vol. 185, pp. 493–506, Feb. 2020, doi: 10.1016/j.actamat.2019.12.038.
- [15] Hou, K., Ou, M., Xing, W., Ma, G., Hao, X., Wang, M., & Ma, Y. (2024). *The formation of n-Ni₃Ti phase microstructure in a cast nickel-based superalloy with high Ti/Al ratio*. Journal of Materials Research and Technology, 29, 764–778.
- [16] Azadian, S.; Wei, L.Y.; Warren, R. *Delta phase precipitation in Inconel 718*. Mater. Charact. 2004, 53, 7–16.
- [17] https://www.lffgroup.com/posts/introduction-to-alloy-625-part-3
- [18] Jiang, L., Zhang, W.-Z., Xu, Z.-F., Huang, H.-F., Ye, X.-X., Leng, B., Yan, L., Li, Z.-J., & Zhou, X.-T. (2016). *M2C and M6C carbide precipitation in Ni-Mo-Cr based superalloys containing silicon*. Materials & Design, 112, 300–308. https://doi.org/10.1016/j.matdes.2016.09.075
- [19] Formenti, A., Eliasson, A., Mitchell, A., & Fredriksson, H. (2005). Solidification Sequence and Carbide Precipitation in Ni-Base Superalloys IN718, IN625 AND IN939. Casting of Metals. KTH - Royal Institute of Technology, Stockholm, Sweden; University of British Columbia, Vancouver, Canada
- [20] S.W.K. Shaw: Response of IN939 to process variations, Superalloys, 1980; pp 275-284.
- [21] https://aviation.stackexchange.com/questions/25645/what-material-is used-to-make-the-hot-sections-of-jet-engines
- [22] Geddes B., Leon H., and Huang X., "Strengthening Mechanisms," in *Superalloys: Alloying and Performance*, 2010, https://doi.org/10.31399/asm.tb.sap.9781627083133.
- [23] M. Abedini M.R. Jahangiri. Effect of long time service exposure on micro structure and mechanical properties of gas turbine vanes made of in 939 alloy. Materials and Design, 2014.
- [24] Marco Gonzalez Albarrán, D. Martínez, A Pérez, and H. Guajardo. *Microstructural rejuvenation through non-conventional heat treatments of an Inconel 939 superalloy.* 08 2012.
- [25] Visibile, A., Gunduz, K. O., Sattari, M., Fedorova, I., Halvarsson, M., & Froitzheim, J. (2024). *High temperature oxidation of inconel 939 produced by additive manufacturing*. Corrosion Science, 233, 112067. https://doi.org/10.1016/j.corsci.2024.112067
- [26] Hardy, M. C., Detrois, M., McDevitt, E. T., Argyrakis, C., Saraf, V., Jablonski, P. D., Hawk, J. A., Buckingham, R. C., Kitaguchi, H. S., & Tin, S. (2020). Solving recent challenges for wrought Ni-base superalloys. Metallurgical and Materials Transactions 50th Anniversary Collection, 2626–2650. https://doi.org/10.1007/s11661-020-05773-6

- [27] F.C. Campbell, Superalloys, in: *Manufacturing Technology for Aerospace Structural Materials*, Elsevier, 2006.
- [28] Mukherji, D., Rösler, J., Strunz, P., Gilles, R., Schumacher, G., & Piegert, S. (Year). *Beyond Ni-based superalloys: Development of CoRe-based alloys for gas turbine applications at very high temperatures*. International Journal of Materials Research.102. (2011).
- [29] Šulák, I., Babinský, T., Chlupová, A., Milovanovič, A., & Náhlík, L. *Effect of building direction and heat treatment on mechanical properties of Inconel 939 prepared by additive manufacturing*. Journal of Mechanical Science and Technology, 37 (3) 2023. https://doi.org/10.1007/s12206-022-2101-7
- [30] Duda, Thomas, and L. Venkat Raghavan. "3D Metal Printing Technology." IFAC-PapersOnLine, vol. 49, no. 29, 2016,. ScienceDirect, doi:10.1016/j.ifacol.2016.11.111.
- [31] https://engineeringproductdesign.com/knowledge-base/powder-bed-fusion/
- [32] T. Aboulkhair, F. Bosio, N. Gilani, C. Phutela, R. J. M. Hague, and C. J. Tuck, "*Additive manufacturing processes for metals*," in Quality Analysis of Additively Manufactured Metals, Elsevier, 2023. doi: 10.1016/B978-0-323-88664 2.00016-6.
- [33] https://www.malvernpanalytical.com/en/industries/advanced-manufacturing/powder-metallurgy/powder-bed-fusion
- [34] *Integrated Manufacturing Systems* course, Prof. Abdollah Saboori. Polytechnic University of Turin.
- [35] Raza, Syed Abbas, Olcay Ersel Canyurt, and Hüseyin Kürşad Sezer. "A Systematic Review of Inconel 939 Alloy Parts Development via Additive Manufacturing Process." Heliyon, vol. 10, 2024, p. e25506. ScienceDirect, doi:10.1016/j.heliyon.2024.e25506.
- [36] https://www.laserline.com/en-int/news-detail/laser-cladding-additive-manufacturing-technology/
- [37] Vilaro, T., Colin, C., Bartout, J. D., Naze, L., & Sennour, M. (2012). *Microstructural and mechanical approaches of the selective laser melting process applied to a nickel-base superalloy.* Materials Science and Engineering: A,534,(2012)446–451. https://doi.org/10.1016/j.msea.2011.11.092
- [38] H.V. Atkinson, S. Davies, "Fundamental aspects of hot isostatic pressing: An overview", Metall. Mater. Trans. A 31, 2000.
- [39] Sushant Negi, Suresh Dhiman, and Rajesh Kumar Sharma. *Basics, applications and future of additive manufacturing technologies: A review.* Journal of Manufacturing Technology Research, volume 5(number1/2), 2013.

- [40] Loh, N. L., and K. Y. Sia. "An Overview of Hot Isostatic Pressing." Journal of Materials Processing Technology, vol. 30, 1992, pp. 45–65.
- [41] Mostafa, Ahmad, Ignacio Picazo Rubio, Vladimir Brailovski, Mohammad Jahazi, and Mamoun Medraj. "Structure, Texture and Phases in 3D Printed IN718 Alloy Subjected to Homogenization and HIP Treatments." Metals (2017). https://doi.org/10.3390/met7060196.
- [42] Rezaie, Amir, and Seyed Ebrahim Vahdat. "Study of Effects of Temperature and Pressure in HIP Process on Mechanical Properties of Nickel-based Superalloys." Materials Today: Proceedings, vol. 4, 2017, pp. 152–56. ScienceDirect, www.sciencedirect.com.
- [43] Li, Xing, et al. "Effect of Heat Treatment on Microstructure Evolution of Inconel 718 Alloy Fabricated by Selective Laser Melting." Journal of Alloys and Compounds, vol. 764, 2018, pp. 639–49. ScienceDirect.
- [44] Sponseller, D. L. *Differential Thermal Analysis of Nickel-Base Superalloys*. ERIM Transportation & Energy Materials Laboratory, 4683 Freedom Drive, Ann Arbor, Michigan, 48108.
- [45] Jahangiri, M. R., Boutorabi, S. M. A., & Arabi, H. (Year). Study on incipient melting in cast Ni base IN939 superalloy during solution annealing and its effect on hot workability. Materials Science and Technology 2012, vol. 28, no. 12.
- [46] Vander Voort, G. F. (1984). Metallography: Principles and Practice. ASM International.
- [47] https://www.zeiss.com/microscopy/en/products/sem-fib-sem/sem/evo.html
- [48] Goldstein, J. et al. (2017). *Scanning Electron Microscopy and X-ray Microanalysis*. Springer. [DOI: 10.1007/978-1-4939-6676-9]
- [49] Li, X., Cui, L., Li, J., Chen, Y., Han, W., Shonkwiler, S., & McMains, S. (2022). *Automation of intercept method for grain size measurement: A topological skeleton approach*. Materials & Design, 224, 111358. https://doi.org/10.1016/j.matdes.2022.111358
- [50] https://terraanaliz.com/labsys-evo-sta
- [51] Alessandro Ruggeri," The influence of Hot Isostatic Pressing performed above solidus temperature of LPBFed Inconel 939 for microstructural improvement". 2023/2024
- [52] https://www.metal-am.com/quintus-supply-hot-isostatic-press-sintavias-metal-additive-manufacturing-facility-florida/
- [53] Rodríguez-Barber, I., & Pérez-Prado, M. T. (2025). Melt pool overlap as a key tool for microstructure design in PBF-LB/M of a Ni-based superalloy: Empirical and analytical approaches. Additive Manufacturing, 109,(20025). https://doi.org/10.1016/j.addma.2025.104901

- [54] Atkinson, H. V., & Davies, S. (2000). Fundamental aspects of hot isostatic pressing: An overview. Metallurgical and Materials Transactions A, 31(12), 2981–3000. https://doi.org/10.1007/s11661-000-0076-4
- [55]https://www.researchgate.net/figure/Schematic-diagram-of-a-nanoindenter-instrument fig82 334284198